Beyond the Standard Model with Composite Particles: A Lattice Study Based on SU(4)

by

William I. Jay

BA, Ball State University, 2012

MASt, University of Cambridge, 2013

A thesis submitted to the

Faculty of the Graduate School of the

University of Colorado in partial fulfillment

of the requirements for the degree of

Doctor of Philosophy

Department of Physics

2018

This thesis entitled:
Beyond the Standard Model with Composite Particles:
A Lattice Study Based on SU(4)
written by William I. Jay
has been approved for the Department of Physics

_____

Prof. Ethan Neil

_____

Prof. Thomas DeGrand

Date _____

The final copy of this thesis has been examined by the signatories, and we find that both the content and the form meet acceptable presentation standards of scholarly work in the above mentioned discipline.

Jay, William I. (Ph.D., Physics)

Beyond the Standard Model with Composite Particles:

A Lattice Study Based on SU(4)

Thesis directed by Prof. Ethan Neil

This thesis is about numerical simulations of a strongly coupled quantum field theory. The quantum field theory is a gauge theory based on the group SU(4) and contains fermionic matter charged under two different representations of the gauge group. The motivation for studying this theory is twofold. First, this theory is closely related to a theory of physics beyond the Standard Model which was recently proposed in the literature. In this model, the Higgs boson is a composite particle, and the top quark is a partially composite particle. Second, theories of this sort represent a new direction in the study of gauge dynamics and thus provide many opportunities to test our qualitative understanding of strongly coupled physics. The main result of this thesis is direct, non-perturbative (albeit numerical) calculation of the particle spectrum of the theory, including both mesons and baryons. Briefly stated, the particle spectrum turns out to be quite similar to that of QCD.

The first three chapters of the thesis serve as a theoretical background. Aside from incidental remarks, the material in these sections appears in standard references. The final four chapters deal with the numerical simulations and contain the new scientific contributions of this thesis. The main results of the thesis are: the low-energy constants associated with the pseudoscalar mesons (found in Table 5.1); estimates of the width-to-mass ratios of the vector mesons (found in Figure 5.14); and the full meson and baryon spectrum in physical units (found in Figure 6.10). For the reader already familiar with lattice techniques, Sections 5.4 and 6.9 provide compact summaries of the techniques and results for the meson and baryon spectrum.

Dedication

To my wife, Anastasia.

To my parents, Ian and Anita.

To the memory of my grandfather, Charles.

Acknowledgements

I am happy to acknowledge those who have helped me achieve the milestone of writing a doctoral thesis. My first thanks belongs to my chief advisors over the past five years, Ethan Neil and Tom DeGrand. They have both shared generously from their wealth of knowledge of quantum field theory and from their personal experience as scientists. It has been a pleasure to work with and learn from them.

My fellow graduate students have provided wonderful scientific and personal support. Dan Hackett has been a faithful checker of minus signs and factors of two; moreover, whatever modicum of computer skills I now possess must certainly be due in large part to him. I am thankful to Abhinav Prem for his many interests outside physics. As we sat discussing literature or film or the arts (or even condensed matter physics), our weekly lunches help provide a welcome balance to my life and thought. I am also grateful to Oscar Henriksson, Brant Rumberger, Andrea Carosso, and Will Cairncross for many lively and instructive conversations.

This thesis would not have been possible without the support of my collaborators: Venkitesh Ayyar, Maarten Golterman, Yigal Shamir, and Ben Svetitsky. I have been lucky to work alongside such knowledgable and careful colleagues.

The morning walk to coffee—commencing promptly at 10:30 each morning—is an institution for Boulder theorists. During the many cumulative hours we spent over coffee, Anna Hasenfratz, Paul Romatschke, Shanta DeAlwis, Oliver DeWolfe, Oliver Witzel, and Yuzhi Liu have broadened my scientific horizons.

Contents

Chapter

1 Introduction **1**

1.1 The Standard Model as an Effective Field Theory 1

1.2 The Archetypal Composite Theory: QCD 3

1.2.1 QCD and Its Broken Chiral Symmetry 4

1.2.2 The Effective Theory of QCD at Low Energy 5

1.2.3 The Quark model 10

1.2.4 Large-N_c QCD 11

1.3 Composite Models of Physics Beyond the Standard Model 13

1.3.1 Ferretti's Model 16

1.3.2 The Minimal Composite Higgs Model 18

1.3.3 The Nature of Experimental Predictions 20

2 Lattice Gauge Theory: An Overview **22**

2.1 Motivation 22

2.2 Technical Formulation 23

2.3 Markov Chain Monte Carlo 28

3 Lattice spectroscopy **32**

3.1 Fermion propagators 34

3.2 Hadron Correlation Functions 36

3.3 Extracting Physical Results 38

4 Simulation Details **42**

4.1 The Lattice Action and Parameters 43

4.2 Global Symmetries 44

4.3 Setting the Scale 45

4.4 Computing the Spectrum 45

4.5 Ensembles 46

5 The Meson Spectrum **50**

5.1 Chiral Perturbation Theory 50

5.1.1 Chiral Perturbation Theory and Setting the Scale 50

5.1.2 Wilson Chiral Perturbation Theory 53

5.1.3 Summary of Formulae from Chiral Perturbation Theory 55

5.2 Pseudoscalar mesons 57

5.2.1 Masses and Decay Constants 57

5.2.2 Stability of the NLO Fit 62

5.2.3 The Flavor-Singlet Goldstone Boson 64

5.3 Vector Mesons 66

5.3.1 Masses and Decay Constants 66

5.3.2 Vector Meson Dominance and the KSRF Relations 70

5.4 Summary of Meson Results 72

6 The Baryon Spectrum **75**

6.1 Overview 75

6.2 Baryons in SU(4) with Two Representations 76

6.3 Continuum Large-N_c Expectations 77

6.4 Baryon Masses on the Lattice 79

6.5 Spectrum Results . . . 81
6.6 Fitting Mass and Lattice-Spacing Dependence . . . 85
6.7 Physical Limits . . . 87
6.8 Scalar Matrix Elements . . . 89
6.9 Summary of Baryon Results . . . 90

7 Conclusions and Outlook **94**

Bibliography **96**

Appendix

A Technical Material **105**

A.1 Lie groups . . . 105
A.2 Symmetry Properties of Common Lattice Operators . . . 109
A.3 Goldstone's Theorem . . . 113
A.4 The General CCWZ Construction . . . 114
A.5 CCWZ for SO(5)/SO(4) . . . 118
A.6 Anomalous Symmetries in QFT . . . 122

B The Method of Conjugate Gradients **124**

B.1 Overview . . . 124
B.2 The Method of Conjugate Directions . . . 125
B.3 The Method of Conjugate Gradients . . . 127

C Construction of Lattice Correlation Functions **132**

C.1 Chimera Baryons . . . 132

D Data Tables **134**

Tables

Table

3.1 Summary of contraction patterns appearing in baryon correlation functions. 38

5.1 Parameter values from a joint fit to the full NLO χPT formulae. 59

6.1 Summary of basic physical properties of the ensembles used in this study. 76

6.2 The baryon spectrum in the double chiral limit ($\hat{m}_4, \hat{m}_6 \to 0$) in units of the flow scale $\sqrt{t_0}$ and of the sextet pseudoscalar decay constant F_6. For comparison, the masses of the fundamental and sextet vector mesons in this limit are also included. Mesonic quantities were determined in [10]. 89

A.1 The J^P classification of meson and diquark operators. 110

D.1 List of ensembles with $V = 16^3 \times 18$ generated for this study. Configurations are separated by 4 Monte Carlo trajectories. 134

D.2 List of ensembles with $V = 16^3 \times 32$. Configurations are separated by 10 Monte Carlo trajectories. 135

D.3 List of ensembles with $V = 24^3 \times 48$. Configurations are separated by 10 Monte Carlo trajectories. 135

D.4 Measured gradient flow scale t_0 and fermion masses $\hat{m}_r = m_r\sqrt{t_0}$ in the ensembles with volume $V = 16^3 \times 18$. 136

D.5 Same as Table D.4, but in the ensembles with volume $V = 16^3 \times 32$. 137

D.6 Same as Table D.4, but in the ensembles with volume $V = 24^3 \times 48$. 137

D.7 Measured pseudoscalar masses $\hat{M}_{Pr} = M_{Pr}\sqrt{t_0}$ and decay constants $\hat{F}_{Pr} = F_{Pr}\sqrt{t_0}$ in the ensembles with volume $V = 16^3 \times 18$. 138

D.8 Same as Table D.7, but in the ensembles with volume $V = 16^3 \times 32$. 139

D.9 Same as Table D.7, but in the ensembles with volume $V = 24^3 \times 48$. 139

D.10 Measured vector masses $\hat{M}_{Vr} = M_{Vr}\sqrt{t_0}$ and decay constants $\hat{F}_{Vr} = F_{Vr}\sqrt{t_0}$ in the ensembles with volume $V = 16^3 \times 18$. Some ensembles did not yield reliable measurements of F_{Vr} because of insufficient statistics. The figures and tables omit data from such ensembles. 140

D.11 Same as Table D.10, but in the ensembles with volume $V = 16^3 \times 32$. 141

D.12 Same as Table D.10, but in the ensembles with volume $V = 24^3 \times 48$. 141

D.13 The ensembles list used in the baryon analysis. All ensembles have volume $V = N_s^3 \times N_t = 16^3 \times 32$. 142

D.14 Fermion masses and flow scales for the ensembles used in the baryon analysis. . . . 142

D.15 Masses $\hat{M}_{Qqq}$ for the chimera baryons in units of the flow scale t_0/a^2. 143

D.16 Masses $\hat{M}_{q^4}$ for the fundamental baryons in units of the flow scale t_0/a^2. 143

D.17 Masses $\hat{M}_{Q^6}$ for the sextet baryons in units of the flow scale t_0/a^2. 144

Figures

Figure

1.1 Some one-loop vacuum polarization diagrams in QCD. 12

2.1 A diagrammatic representation of a plaquette $U_{\mu\nu}(n)$, the lattice analogue of a Wilson loop. The dots represent the nodes of the lattice. Each arrowhead represents a gauge link U. The free lines at site n indicate the un-contracted group indices in Eq. (2.9). 25

2.2 A diagrammatic representation of the object $Q_{\mu\nu}$ which appears in the clover term, in a fixed $\mu\nu$-plane. The dots represent the nodes of the lattice. Each arrowhead represents a gauge link U. Gauge links moving in opposite directions between the same nodes are related by hermitian conjugation. 27

3.1 A graphical representation of the propagator tensor of Eq. (3.15) from spacetime site m to site n. Color indices are associated to solid external lines. Spin (Lorentz) indices are associated to dotted external lines. 35

3.2 A graphical representation of the tensor contractions appearing in meson two-point correlation functions. The lines with arrows and ψ, $\bar{\psi}$ on the ends are the propagators. The dotted lines indicate spin contractions against the Dirac structure Γ. The white hollow boxes indicate color contractions against the Kronecker delta of SU(N_c). The connected diagram on the top is present for all mesons. The disconnected diagram on the bottom is present, e.g., for flavor singlet mesons. 37

3.3 A graphical representation of the tensor contractions appearing in baryon two-point correlation functions. The lines with arrows and labels u, d, or s on the ends are the propagators. The dotted lines indicate spin contractions against the Dirac structure Γ. The free dotted lines reflect the fact that the source and sink operators are fermionic. The solid black boxes indicate color contractions against the Levi-Civita tensor of SU(3). The top two diagrams have a closed "spin loop" and correspond to "spin topology A." The bottom three diagrams correspond to "spin topology B." . 39

4.1 Map of our ensembles in the plane of pseudoscalar masses M_{Pr}. These are coarse lattices, with $0.94 < \sqrt{t_0}/a < 1.41$. We define arbitrarily $\sqrt{t_0} = (1.4\text{ GeV})^{-1}$ for comparison with QCD. For most of these ensembles $1/a \simeq 1.45$ GeV by this measure. 48

4.2 Same as Fig. 4.1, but here we plot ensembles on fine lattices, $\sqrt{t_0}/a > 1.41$. If we fix $\sqrt{t_0} = (1.4\text{ GeV})^{-1}$ then this means $1/a > 2$ GeV. The blue squares are all at $1/a \simeq 2.1$ GeV. 49

5.1 Squared mass of the two pseudoscalar species, each plotted against the AWI mass of the corresponding fermion species, all in units of the flow scale t_0. 57

5.2 Decay constant of each pseudoscalar species plotted against the mass of the corresponding fermion species, in units of the flow scale t_0. 58

5.3 Breakdown of the contribution of lattice artifacts in the joint fit to χPT for the fundamental masses and decay constants. 60

5.4 Breakdown of the contribution of lattice artifacts in the joint fit to χPT for the sextet masses and decay constants. 61

5.5 Exploring the stability of leading-order LECs in chiral fits. We take the NLO result to define our central values, which appear at the bottom of each column. The variations are described in the text. 63

5.6 Mass squared $\hat{M}_\zeta^2$ of the non-anomalous Goldstone boson in the combined continuum ($\hat{a} \to 0$) and chiral-sextet ($\hat{m}_6 \to 0$) limits, as extracted using Eq. (5.18) and the central fit's parameters, plotted against $\hat{m}_4$. The pseudoscalar mass $\hat{M}_4^2$ in the fundamental sector in the same limit is shown for comparison. 65

5.7 Vector masses vs fermion masses in units of the flow scale t_0. 66

5.8 Vector decay constants vs fermion masses in units of the flow scale t_0. 67

5.9 The mass ratio M_{Pr}/M_{Vr} in a fixed representation. 67

5.10 Breakdown of the contribution of lattice artifacts in the empirical models for the vector masses and decay constants in the fundamental representation. 68

5.11 Breakdown of the contribution of lattice artifacts in the empirical models for the vector masses and decay constants in the sextet representation. 69

5.12 The ratio of the vector and pseudoscalar decay constants in each representation. The KSRF prediction is a constant value of $\sqrt{2}$. 70

5.13 The ratio of the vector mass and pseudoscalar decay constant in a fixed representation. KSRF identify this quantity with the coupling g_{VPP}. In QCD, this ratio is roughly 5.9. 71

5.14 Tree-level estimates for the width-to-mass ratio of the vector mesons according to KSRF. The KSRF estimate for this ratio is roughly 0.23 in QCD. 72

6.1 Lattice data for the baryon mass spectrum $\hat{M}_B$. The horizontal positions contain small offsets to reduce overlap and aid readability. 81

6.2 Mass splittings between baryons in the fundamental (left) and sextet (right) representations. The lines indicate the expected $J(J+1)$ behavior. 82

6.3 Estimates for the total constituent mass of the chimera baryons from the chimeras themselves (vertical axis) again the estimates from single-representation baryons (horizontal axis). The line indicates the expectation that the two independent estimates agree. 83

6.4 Estimates of the splitting coefficients B_{44}, B_{66}, and B_{46} on each ensemble as functions of $\hat{m}_4$ (left) and $\hat{m}_6$ (right). The horizontal positions contain small offsets to reduce overlap and aid readability. 84

6.5 Data (solid marker) and linear fits (open marker) to each state in the fundamental and sextet multiplets using the simple linear model (6.5), including a linear term proportional to $\hat{a}$. The error bars of the open markers are those of the fit. The horizontal positions contain small offsets to reduce overlap and aid readability. . . . 85

6.6 Results from the joint correlated fit of all baryon data to Eqs. (6.8), (6.9), and (6.10). The data (solid marker) correspond well to the fit (open marker) at each point. The errors bars of the open markers are those of the fit. The horizontal positions contain small offsets to reduce overlap and aid readability. 86

6.7 Results from the joint correlated fit of all baryon data to Eqs. (6.8)–(6.10). The left pane shows continuum masses obtained by subtracting the lattice artifact from the data. The right pane shows the corresponding fit, with the lattice artifact term removed. The horizontal positions contain small offsets to reduce overlap and aid readability. 87

6.8 The baryon spectrum in the $\hat{m}_6 \to 0$ limit. 88

6.9 Baryon matrix elements of the scalar density, defined via Eq. (6.20). Only the lightest state in each representation is shown; the heavier states are similar. The mesonic quantities were determined in [10]. 90

6.10 Baryon and meson masses in the $m_6 \to 0$ limit. The chimera $(J, I) = (1/2, 0)$ state corresponds to the top partner of Ferretti's model. The small rise of the sextet quantities in this limit is due to the mild variation of $\hat{F}_6$ with the fundamental fermion mass. Mesonic quantities were determined in [10]. 93

A.1 Some useful birdtrack diagrams for reducing contractions of SU(N) and SO(N) generators. 109

A.2 A graphical demonstration of the inductive proof of the preceding lemma. The square represents the generator $T^{\hat{a}}$, the circles represent $\pi_{\hat{a}}$, and the rounded rectangle represents $\partial\pi_{\hat{a}}$. The first line establishes the base case, and the induction proceeds by contracting powers of the quantity in parentheses. 120

Chapter 1

Introduction

1.1 The Standard Model as an Effective Field Theory

The Standard Model (SM) is a quantum field theory (QFT) based on the gauge group SU(3) × SU(2) × U(1).[1] In addition to the gauge boson fields, the SM also contains three generations of fermionic matter fields (quarks and leptons) and a fundamental scalar (the Higgs field). Although the principle of gauge invariance elegantly prescribes the form of SM interactions, some basic theoretical questions lie outside its purview. Why is the Higgs mass 125 GeV? Why is the top quark more than 10,000 times heavier than the light quarks? Models of physics beyond the Standard Model (BSM) are necessary to answer such questions. Physics beyond the Standard Model is also necessary to explain the observed effects of dark matter and dark energy.

In the modern perspective, any QFT is viewed as an effective field theory (EFT), i.e., an effective description valid up to some high-energy cutoff Λ. The Standard Model is no exception, and the EFT perspective provides valuable insight into the possible structure of new physics. In particular, the hierarchy problem and the more general notion of naturalness find their clearest expression when couched in the language of EFT. My own understanding of the Standard Model as an EFT has been shaped to a large extent by a series of lectures given by Rattazzi at the 2015 TASI summer school [124].

In an EFT, the physical Lagrangian contains *all* operators consistent with the field content

[1] Many excellent books discuss the Standard Model. The introductory text by Schwartz [129] and the more specialized treatment by Donoghue, Golowich, and Holstein [72] receive my warm recommendation.

and symmetries of the theory. Typically an infinite number of operators are possible. However, only a finite number of relevant or marginal operators (i.e., those with engineering dimension $\Delta \leq 4$) appear in most cases of interest. Therefore, the low-energy dynamics of the theory becomes insensitive to the high energy structure of the irrelevant operators (i.e., operators with engineering dimension $\Delta > 4$). An important physical consequence of this fact is the appearance of accidental symmetries at low energies. For instance, parity is a global symmetry of low-energy electrodynamics, while the full electroweak theory couples to left-handed fermions only and thereby breaks parity maximally. Most of the global symmetries in the Standard Model—like lepton or baryon number—are accidental symmetries.

A EFT is said to be *natural* if any exponentially small dimensionless quantities are associated with an approximate symmetry. This notion also extends to quantities like masses after accounting for dimensionality with power counting. Of course, no *a priori* physical principle says that the Standard Model or any other QFT must be natural. However, naturalness is a fruitful guiding principle, since approximate symmetries often arise as accidental symmetries of a more fundamental description.

Viewed through the lens of naturalness, the Standard Model contains a fundamental tension known as the hierarchy problem. The essential difficulty is that some quantities suggest a large separation of scales between the electroweak scale and the cutoff, while others imply that the cutoff should be near the electroweak scale. This general discussion is aided by concrete examples.

Consider first the case of neutrino masses, which are generated (at lowest order) by the dimension-five Weinberg operator [140]:

$$\mathcal{O}_5 = \frac{1}{\Lambda}\left(\overline{\ell}^c_{iaL}\ell_{jbL}\right) H_k H_l \left[f_{ab}\epsilon^{ik}\epsilon^{jl} + f'_{ab}\epsilon^{ij}\epsilon^{kl}\right], \tag{1.1}$$

where ℓ_L is a left-handed lepton doublet, $\overline{\ell}^c_L$ is the charge conjugate, and H is the Higgs doublet. Spinor indices (suppressed) are contracted into a Lorentz scalar inside the parentheses, while the $\mathrm{SU}(2)_L$ gauge indices i, j, k, l are contracted into singlets using the Levi-Civita tensor of $\mathrm{SU}(2)_L$. The dimensionless coupling constants f and f' connect generations of leptons (a, b) and are pre-

sumed, by naturalness, to be of order unity. After the Higgs field develops a vacuum expectation value v, this operator generates a mass for the neutrinos of order $m_\nu \sim v^2/\Lambda$. Given that neutrino masses are known experimentally to be roughly 0.1 eV, this relationship furnishes an estimate of the physical cutoff of the Standard Model:

$$\Lambda \sim \frac{v^2}{m_\nu} \sim \frac{(246\,\mathrm{GeV})^2}{0.1\,\mathrm{eV}} \sim 10^{14} - 10^{15}\,\mathrm{GeV}. \tag{1.2}$$

As a second example, consider the mass of the Higgs, mediated by the relevant operator

$$\mathcal{O}_2 = m_H^2 \left|H\right|^2 \equiv c\Lambda^2 \left|H\right|^2. \tag{1.3}$$

By naturalness, the dimensionless coupling c should generically be of order unity, or at least only algebraically small. But since the Higgs mass is known to be 125 GeV, this implies that the cutoff is also at the electroweak scale $\Lambda \sim 0.1 - 1\,\mathrm{TeV}$. If one instead takes the previous estimate $\Lambda \sim 10^{14}\,\mathrm{GeV}$ at face value, the dimensionless coupling must then be exponentially small $c \sim 10^{-24}$. In a natural theory, exponentially small numbers are only permissible when protected by some symmetry. The Standard Model does not possess any known symmetry principle which protects the Higgs mass; this fundamental conflict is the hierarchy problem.

In addition to the obvious requirement of continuing to agree with existing experimental data, a theoretically satisfying BSM model should render the Higgs mass natural without reintroducing relevant operators and creating a new hierarchy problem. The literature on BSM phenomenology is vast, and reviewing it exceeds the scope of this thesis. We simply note that many appealing theoretical ideas exist—ranging from supersymmetry to compact extra dimensions—beyond those studied here. The particular focus of this thesis is the notion of compositeness. We introduce compositeness first through the example of quantum chromodynamics in Sec. 1.2 to motivate the composite BSM models of Sec. 1.3.

1.2 The Archetypal Composite Theory: QCD

Quantum chromodynamics (QCD) is the SU(3) gauge theory within the Standard Model which describes hadronic interactions. Both experimentally and theoretically, QCD is probably the

best-known and most-studied strongly interacting QFT. At high energies, the fundamental quark and gluon fields of QCD interact weakly, and perturbation theory adequately describes their physics. Due to asymptotic freedom, the interactions become strong at lower energies. Below energies of about 1 GeV, the interactions becomes strong enough that the chiral condensate $\langle\bar{\psi}\psi\rangle$ develops a vacuum expectation value and spontaneously breaks chiral symmetry. At least schematically, the phenomenon is similar to spontaneous magnetization in solids. At the same time, the phenomenon of confinement hides away the quarks and gluons inside composite states, the familiar hadronic menagerie of mesons and baryons. Because QCD possess such a rich and extensively studied spectrum, it forms the basis of much of our understanding and speculation about other possible composite sectors. In this sense, QCD is the archetypal composite theory.

1.2.1 QCD and Its Broken Chiral Symmetry

In addition to its eight gluons, QCD contains six flavors of Dirac fermions. The fermions are charged under the fundamental representation of SU(3). Two of these flavors (or three, depending on the physical process of interest) are light, in the sense of having masses much below the QCD scale ($m \ll \Lambda_{\text{QCD}} \sim 1$ GeV). Recall that four-component Dirac fermions may be decomposed into a pair of two-component Weyl fermions using charge conjugation. Following Peskin [122], consider QCD as SU(N_c) gauge theory coupled to $2N_f$ Weyl fermions, with N_f fermions $\psi_\alpha^{(\mathbf{r})ai}$ in a complex representation $\mathbf{r}$ and N_f fermions $\psi_{\alpha ai}^{(\bar{\mathbf{r}})}$ in the conjugate representation $\bar{\mathbf{r}}$. Here α, β are Lorentz indices, a is a gauge index, and $i = 1, 2, \ldots, N_f$ is a flavor index. After accounting for the Adler-Bethe-Jackiw anomaly (see Appendix A.6 for more information about anomalies), the global symmetry structure of the theory is $\text{SU}(N_f)_L \times \text{SU}(N_f)_R \times \text{U}(1)_B$, which independently rotates the left- and right-handed components of the fermions. The formation of a chiral condensate

$$\epsilon^{\alpha\beta}\psi_\alpha^{(\mathbf{r})ai}\psi_{\beta ai}^{(\bar{\mathbf{r}})} \tag{1.4}$$

breaks this symmetry down to the diagonal (or "vector") subgroup $\text{SU}(N_f)_V \times \text{U}(1)_B$, those transformations which preserve the complex "dot product" $\delta^i{}_j$.

The physical consequences of this broken symmetry are immediately evident in the particle spectrum of QCD. First, the light pions are the telltale (pseudo) Goldstone bosons accompanying any spontaneously broken global symmetry. Second, the spectrum does *not* exhibit parity doubling. For instance, the mass of the proton is roughly 940 MeV, while its opposite-parity partner is nearly 1500 MeV. If chiral symmetry were unbroken, these states would have the same mass.

In a more general setting, a spontaneously broken flavor symmetry will still be characterized by a Lorentz-scalar operator developing a vacuum expectation value. However, depending on the representation of the matter fields (presumed to be fermions), the pattern of chiral symmetry breaking can be different. To see how this works in another case of interest for this thesis, consider $\mathrm{SU}(N_c)$ gauge theory coupled to $2N_f$ flavors of two-component fermions in a real representation, corresponding to a global $\mathrm{SU}(2N_f)$ flavor symmetry group. By definition of a real representation, their exists a symmetric invariant tensor d_{ab} acting on the gauge indices, which allows the formation of a "chiral condensate"

$$\epsilon^{\alpha\beta}\psi_{\alpha}^{(\mathbf{r})ai}\psi_{\beta}^{(\mathbf{r})bi}d_{ab}, \tag{1.5}$$

with indices as above and the flavor index now in $i = 1, 2, \ldots, 2N_f$. The unbroken symmetry comprises those transformations which preserve this real "dot product" in flavor space. In other words, the pattern of symmetry breaking is $\mathrm{SU}(2N_f) \to \mathrm{SO}(2N_f)$. In general, one typically assumes that dynamical mass generation—as characterized by the formation of a "chiral" condensate—preserves the largest possible flavor symmetry [122].

1.2.2 The Effective Theory of QCD at Low Energy

In the previous section, we argued that the formation of a chiral condensate in low-energy QCD breaks the global flavor symmetry $\mathcal{G}_{\mathrm{F}}$ down to a subgroup $\mathcal{H}_{\mathrm{F}}$. The ground state of the system, which includes the condensate, acquires non-trivial transformation properties under $\mathcal{G}_{\mathrm{F}}$. The fact that the vacuum now transforms implies that it consists of a manifold of states: those that can be reached by transformations in $\mathcal{G}_{\mathrm{F}}$, modulo those in the unbroken subgroup $\mathcal{H}_{\mathrm{F}}$. In

other words, the vacuum is the coset $\mathcal{G}_{\rm F}/\mathcal{H}_{\rm F}$. This general observation has important consequences for the spectrum and low-energy dynamics of the theory.

First, as hinted above, Goldstone's theorem says that theory contains massless particles which couple to broken generators, i.e., those in $\mathcal{G}_{\rm F}/\mathcal{H}_{\rm F}$. A proof of this statement appears in Appendix A.3. Second, even when broken spontaneously, symmetry completely determines the low-energy dynamics of the massless particles. The resulting effective theory is known in QCD as chiral perturbation theory.

A particularly attractive method for constructing a Lagrangian consistent with broken symmetry is due to Callan, Coleman, Wess, and Zumino (CCWZ). The chief virtue of their technique is that it provides a method for writing down the correct Lagrangian for *arbitrary* broken symmetries. Appendix A.4 reviews the technical aspects of the CCWZ construction. In brief, their method amounts to cataloguing objects with homogeneous transformation properties under the full symmetry group, $\mathcal{G}_{\rm F}$. The EFT Lagrangian is then simply the most general $\mathcal{G}_{\rm F}$-invariant function of these objects. As an instructive example, we shall review quickly how the EFT of two-flavor QCD arises in their general framework. The setup is slightly different from the usual presentation of the chiral Lagrangian.

The Goldstone bosons π transform under an induced nonlinear representation of the full symmetry group $\mathcal{G}_{\rm F}$. We shall denote this representation by r_π. Although nonlinear under $\mathcal{G}_{\rm F}$, the induced representation is linear when restricted to $\mathcal{H}_{\rm F} \subset \mathcal{G}_{\rm F}$. The simplest building block in the CCWZ scheme is the tensor $\mathbf{d}_\mu \simeq \partial_\mu \pi + \cdots$, which acts as a "$\mathcal{G}_{\rm F}$-covariant derivative" of the Goldstone modes; its precise definition appears is given in Appendix A.4 in Eq. (A.53). Neglecting temporarily terms involving the fermion mass, the leading-order CCWZ Lagrangian is simply the square of this covariant derivative:

$$\mathcal{L} = \frac{F^2}{4} \operatorname{Tr} \mathbf{d}_\mu \mathbf{d}^\mu, \tag{1.6}$$

where the leading coefficient ensures canonical normalization of the kinetic term. Further progress requires a particular coset of broken generators. In the case of two-flavor QCD (with $\mathcal{G}_{\rm F}/\mathcal{H}_{\rm F} =$

$\mathrm{SU}(2)_L \times \mathrm{SU}(2)_R \to \mathrm{SU}(2)_V$), it can be shown that the tensor $\mathbf{d}_\mu$ assumes the following form:

$$\mathbf{d}_\mu = \frac{\sqrt{2}}{F}\partial_\mu \pi_{\hat{a}} T^{\hat{a}} + \frac{\sqrt{2}}{F^3}\frac{}{3}((\partial_\mu \pi \times \pi) \times \pi)_{\hat{a}} T^{\hat{a}} + \cdots . \tag{1.7}$$

Squaring this quantity and tracing, one recovers the Goldstone kinetic term and leading-order interactions.

$$\mathcal{L} = \mathcal{L}_0 + \mathcal{L}_{\text{int}} \tag{1.8}$$

$$\mathcal{L}_0 = \frac{1}{2}\partial_\mu \pi_{\hat{a}} \partial^\mu \pi^{\hat{a}} \tag{1.9}$$

$$\mathcal{L}_{\text{int}} \sim \left[(\pi^{\hat{a}}\partial_\mu \pi_{\hat{a}})(\pi^{\hat{b}}\partial^\mu \pi_{\hat{b}}) - (\partial_\mu \pi_{\hat{a}})(\partial^\mu \pi^{\hat{a}})(\pi_{\hat{b}}\pi^{\hat{b}})\right] + \cdots . \tag{1.10}$$

Although somewhat complicated, interactions of this form are familiar from the study of non-linear sigma models. We observe that the leading interactions are quartic in the pions and are derivatively coupled. This derivative coupling respects a shift symmetry (see Eq. (A.52) in Appendix A.4 for additional context) and protects the vanishing Goldstone mass from radiative corrections.

Standard discussions of chiral perturbation theory do not mention the tensor $\mathbf{d}_\mu$, instead focusing on a Lagrangian of the form

$$\mathcal{L}^{\chi\text{PT}} = \frac{F^2}{4}\,\mathrm{Tr}\left(\partial_\mu U \partial^\mu U^\dagger\right), \tag{1.11}$$

where $U = e^{i2\pi_{\hat{a}} T^{\hat{a}}/F_\pi}$ is the Goldstone boson matrix. To compare with the interactions of Eq. (1.10), we expand $\mathcal{L}^{\chi\text{PT}}$. The quadratic portion and leading-order interactions are

$$\mathcal{L}_0 = \frac{1}{2}(\partial_\mu \vec{\pi}) \cdot (\partial^\mu \vec{\pi}) \tag{1.12}$$

$$\mathcal{L}_{\text{int}} \sim \left[(\vec{\pi} \cdot \partial_\mu \vec{\pi})^2 - \vec{\pi}^2(\partial_\mu \vec{\pi} \cdot \partial^\mu \vec{\pi})\right], \tag{1.13}$$

so the two methods agree. Many equivalent formulations, differing by nonlinear field redefinitions, exist for formulating low-energy EFTs. Of course, physical predictions (like on-shell scattering amplitudes) are independent of the field redefinition. Recent lectures by Csáki and Tanedo and a thesis from Budìnek provide an even more explicit translation guide for moving between the abstract CCWZ construction and chiral Lagrangians with the form of Eq. (1.11) [46, 34]. The key

point is that a Lagrangian of the form Eq. (1.11) depends on the $\mathcal{G}_{\rm F}/\mathcal{H}_{\rm F}$ coset being a symmetric space, i.e., possessing a particular notion of parity. In QCD, the necessary symmetry arises from switching "left" and "right" in the definition of the axial rotations.

Lattice discretization of fermions often breaks chiral symmetry. Therefore, from the perspective of lattice simulations, EFT provides a framework for taking a theoretically controlled chiral limit. So far the discussion has neglected the effects of terms which explicitly break the global symmetries. In the UV theory, such terms include an explicit mass for the fermions

$$m\bar{\psi}\psi = m(\bar{\psi}_L\psi_R + m\bar{\psi}_R\psi_L). \tag{1.14}$$

At low energies, so-called spurions mediate this explicit symmetry breaking.

Let us introduce spurions by way of example. For instance, consider a mass matrix M, which might have the following form in two-flavor QCD

$$M = \begin{pmatrix} m_u & 0 \\ 0 & m_d \end{pmatrix} = M_0 \mathbb{1}_2 + M_z \sigma_z, \tag{1.15}$$

with $M_0 = (m_u + m_d)/2$ and $M_z = (m_u - m_d)/2$. Writing the matrix in this form makes it clear that, in the back of our minds, we have chosen some particular basis for the coset $\mathcal{G}_{\rm F}/\mathcal{H}_{\rm F}$ to describe the physical pions. Of course, the physics should be independent of this choice, which means that the M should have definite transformation properties under $\mathcal{G}_{\rm F}$. Let us suppose that the mass matrix transforms in the same nonlinear representation as the Goldstone matrix, i.e., $M \longmapsto gMh^{-1}(g;\pi)$ (cf. Eq. (A.46) in Appendix A.4). In this case, the following term may be added to the leading-order EFT:

$$\mathcal{L}_{\rm explicit} \sim {\rm Tr}[MU^{-1} + M^{-1}U] \tag{1.16}$$

$$= {\rm Tr}[M]\vec{\pi}\cdot\vec{\pi} + \cdots \tag{1.17}$$

$$= (m_u + m_d)\vec{\pi}\cdot\vec{\pi} + \cdots \tag{1.18}$$

$$\sim (m_\pi^2)\vec{\pi}\cdot\vec{\pi} + \cdots, \tag{1.19}$$

where we've taken M to be a real, symmetric matrix. The leading contribution occurs sensibly at quadratic order in the pions. Applications typically work with the rescaled quantity $\chi = 2BM$, where B is a new low-energy constant. In this case, the leading-order term with explicit symmetry breaking is

$$\mathcal{L}_{\text{explicit}} = \frac{F^2}{4} \operatorname{Tr}[\chi U^{-1} + \chi^{-1} U]. \tag{1.20}$$

This short discussion also reveals a qualitatively important point: at leading order, the square of the Goldstone mass is linear in the fermion mass. Coupling to the mass matrix also induces quartic interactions among the Goldstone bosons which, lacking any derivatives, break the aforementioned shift symmetry.

Including quantum fluctuations in the EFT proceeds according to the following steps. First, the leading order Lagrangian defines the interaction vertices for calculating tree-level processes and their one-loop corrections. Second, the next-to-leading order Lagrangian (which we have not discussed) furnishes additional interaction vertices, which appear at tree level. Adding together results from the first two steps yields a superficially divergent result, which must be regulated, e.g., in the $\overline{\text{MS}}$ scheme. Because the chiral Lagrangian contains many complicated interactions, calculations such as these are rather involved and exceed the scope of this thesis. Books, notes, and reviews treat this subject in detail [72, 80, 86]. As an example of the sort of results one can obtain, it can be shown that the one-loop renormalized (pseudo) Goldstone mass is:

$$m_\pi^2 = (2Bm_q)\left[1 + L(2Bm_q) + \frac{(2Bm_q)}{16\pi^2 F^2} \log \frac{(2m_q B)}{\mu^2}\right], \tag{1.21}$$

where μ^2 is an arbitrary reference scale and L is a calculable linear combination of low-energy constants appearing in the chiral Lagrangian. To a lattice gauge theorist, Eq. (1.21) provides the means to extract low-energy constants (B, F, and L) from lattice data at finite fermion mass: simply determine M_π and m_q for a variety of fermion masses and conduct a fit.

1.2.3 The Quark model

The quark model refers to a broad set of theoretical ideas used to understand the observed spectrum of hadronic physics [72, 120]. The general philosophy of the quark model is to focus on the valence-quark content of hadrons. At its simplest level, the quark model provides an organizing principle for studying the hadron spectrum through the classification of gauge-invariant local operators. With the addition of some dynamical model assumptions, non-relativistic quark models provide a simple and semi-quantitative description of hadron masses in terms of constituent quarks.

The primary building blocks for constructing gauge-invariant local operators are meson ($\bar{\psi}\Gamma\psi$) and diquark ($\psi^{\mathrm{T}}C\Gamma\psi$) operators, where Γ is some product of gamma matrices. The choice of appropriate Γ allows for the formation of operators with definite spin, parity, and charge-conjugation properties. Appendix A.2 classifies common choices for Γ along with their quantum numbers. The quark model says that simple operators like ($\bar{\psi}\gamma_5\psi$) and ($\bar{\psi}\gamma_i\psi$) should describe the pseudoscalar and vector mesons, while operators like $\psi(\psi^{\mathrm{T}}C\gamma_5\psi)$ correspond to baryons.

So far the discussion of the quark model has neglected flavor. In the case of three light quarks (up, down and strange), QCD possess an approximate SU(3) flavor symmetry. Mesons and baryons are therefore classified by products of representations of SU(3):

$$\mathbf{3}\otimes\bar{\mathbf{3}} = \mathbf{8}\oplus\mathbf{1} \tag{1.22}$$

$$\mathbf{3}\otimes\mathbf{3}\otimes\mathbf{3} = (\mathbf{6}\oplus\bar{\mathbf{3}})\otimes\mathbf{3} = \mathbf{10}\oplus\mathbf{8}\oplus\mathbf{8}\oplus\mathbf{1}. \tag{1.23}$$

Eq. (1.22) says that mesons should appear in a flavor octet alongside a flavor singlet. The octet corresponds to the observed pions, kaons, and the eta:

$$(\pi^0, \pi^{\pm}, K^0, \bar{K}^0, K^{\pm}, \eta), \tag{1.24}$$

while the flavor singlet is the η'. Eq. (1.23) says that baryon spectrum should include a spin-3/2 decuplet

$$(\Delta^0, \Delta^{\pm}, \Delta^{++}, \Sigma^{*0}, \Sigma^{*\pm}, \Xi^{*0}, \Xi^{*0}, \Omega^{-}) \tag{1.25}$$

and a spin-1/2 octet

$$(n, p, \Sigma^0, \Sigma^{\pm}, \Lambda, \Xi^0, \Xi^-), \tag{1.26}$$

in agreement with observation. These group theoretical observations form the foundation of lattice spectroscopy techniques, described in more detail in Chapter 3.

The valence-fermion picture of hadrons also admits semi-quantitative predictions of masses. The idea is to image that each valence quark is surrounded by a cloud of virtual quarks, antiquarks, and gluons, which is presumed to form a collective degree of freedom called a constituent quark. By solving the non-relativistic Schrödinger equation in terms of these constituent quarks (and their constituent masses) in an external potential, one can determine energy levels and quark wavefunctions.

No rigorous derivation of the correct external potential exists from QCD. Nevertheless, in the spirit of phenomenology, a variety of reasonable model assumptions are often made. For instance, the potential often includes a spin-independent, long-range confining term. Motivated by single-gluon exchange and in analogy with the hyperfine interaction of atomic physics, the potential often includes a short-range, spin-dependent term. After accounting for the appropriate group theoretical differences, modes like these play an important role in understanding the spectrum of other strongly coupled QFTs. In particular, Chapter 6 uses an quark model to interpret the baryon spectrum in the lattice simulations of this thesis.

1.2.4 Large-N_c QCD

The essential feature of gauge theories is a paucity of free parameters. In the absence of fermion masses, a single measurement (of, say, a hadron mass) determines all other physical quantities in the theory. In this sense, gauge theories are maximally predictive theories of nature. The drawback is that these theories become very hard to solve with pen-and-paper techniques in regimes where the interactions are intrinsically strong. Without free parameters, it becomes impossible to construct controlled approximations, e.g., in the coupling strength between the particles and fields,

Figure 1.1: Some one-loop vacuum polarization diagrams in QCD.

which is absorbed into defining the scale of masses via the renormalization group.

Long ago 't Hooft realized that gauge theories do, in fact, possess a disguised expansion parameter [138]. His insight was that QCD—with three colors and gauge group SU(3)—should be considered alongside a series of sister gauge theories with N_c colors and the gauge group SU(N_c). The idea was and remains that the theory with large N_c may be easier to solve, while retaining a close quantitative and qualitative resemblance to QCD with $N_c = 3$. Although large-N_c QCD has so far defied exact analytic solution, much of our qualitative understanding of QCD finds its best theoretical justification in large-N_c arguments. One of the nicest expositions of large-N_c is due to Witten [145].

Why do gauge theories simplify at large-N_c? In the simplest physical terms, a counting argument is responsible: the $\mathcal{O}(N_c^2)$ gluonic degrees of freedom completely dominate the $\mathcal{O}(N_c)$ fermion degrees of freedom, which can be neglected to leading order.

Let us now consider the large-N_c limit more precisely. A well-defined perturbative expansion should contain, e.g., a smooth limit for the one-loop gluon vacuum polarization, shown on the left of Fig. 1.1. But this quantity scales as

$$g^2 f_{acd} f_{bcd} = \delta_{ab} g^2 C_A = \delta_{ab} g^2 N_c, \tag{1.27}$$

where the f are the structure constants of SU(N_c), g^2 is the gauge coupling, and $C_A = N_c$ is the adjoint Casimir. A finite limit exists for this quantity if the 't Hooft coupling $\lambda \equiv g^2 N_c$ is held fixed. The situation is different for the one-loop fermion contribution to the gluon propagator,

shown on the right of Fig. 1.1. This quantity scales as

$$g^2 \,\mathrm{Tr}[T_a T_b] = \delta_{ab} g^2 T(R) = \delta_{ab} \frac{\lambda}{2N_c} \tag{1.28}$$

and therefore vanishes in the large-N_c limit. This example illustrates a general feature: fermionic fluctuations are suppressed as $1/N_c$ in the large-N_c limit. For the purpose of this thesis, we shall only need some highlights from large-N_c:

(1) meson masses have a smooth (i.e., finite) large-N_c limit,

(2) meson decay constants grow as $\sqrt{N_c}$ in the large-N_c limit, and

(3) baryon masses grow as N_c in the large-N limit.

More careful treatment of theses points exist in the literature; see 't Hooft or Witten and the references therein [138, 145]. The literature has focused largely on the case of fermions in the fundamental representation. A suggestive generalization to fermions charged under higher representations replaces factors of N_c by $\dim_f$, the dimension of the representation. Our lattice results support this generalization.

1.3 Composite Models of Physics Beyond the Standard Model

Compositeness is the idea that some particles in the Standard Model are not point-like but rather bound states of some new strongly interacting sector. The essential physical analogy is QCD, where the hadrons appear point-like at long distances ($L \gg 1/\Lambda_{\mathrm{QCD}}$) despite being composite objects. At least in principle, the hypothesis of compositeness can solve many problems [74, 102, 83].

First, a composite Higgs boson is naturally light, since its mass is generically that of the compositeness scale or, in the case of pseudo Goldstone bosons, can be tuned to be parametrically light. Second, gauge-fermion systems like QCD contain no strongly relevant operators (with engineering dimension $\Delta \leq 4$), so no new hierarchy problem arises. A useful modern reference to these ideas is the monograph by Panico and Wulzer [121].

The fate of fermions in composite models requires a somewhat longer explanation. Consider first the Standard Model, where fermions receive masses through Yukawa couplings to the Higgs field,

$$\mathcal{L}_{\text{mass}} = -Y^d_{ij}\left(\overline{Q}^i H d^j_R\right) - Y^u_{ij}\left(\overline{Q}^i \tilde{H} u^j_R\right) + h.c., \tag{1.29}$$

where $Q = (u_L, d_L)^{\text{T}}$ is an SU(2) doublet of quarks in generation i. A similar expression exists for the leptons. The Yukawa couplings of the two 3×3 matrices Y^d and Y^u are (up to some well-understood redundancy) free parameters of the Standard Model.

The story for fermion masses is different in composite models, since the Higgs is no longer a fundamental field. The microscopic explanation of fermion masses therefore involves composite operators, rather than the Higgs field itself. Different scenarios are possible, depending on whether the Standard Model fermions couple quadratically or linearly to the composite operators. Linear coupling introduces mass mixing and therefore goes by the name of partial compositeness; larger mixing means that a given fermion is more composite.

Dimensional analysis shows some of the difficulties associated with compositeness and why partial compositeness may be a useful mechanism. To see how the argument works, consider a mixed operator which is the product of Standard Model fields $\mathcal{O}_{\text{SM}}$ and elementary fields in the new composite sector $\mathcal{O}_{\text{BSM}}$:

$$\mathcal{O} = \frac{\lambda[\Lambda_{\text{UV}}]}{\Lambda_{\text{UV}}^{\Delta_{\text{BSM}}+\Delta_{\text{SM}}-4}}\mathcal{O}_{\text{BSM}}\mathcal{O}_{\text{SM}}. \tag{1.30}$$

In this expression, Λ_{UV} is the cutoff of the composite theory itself and the scale at which the product operator is generated. The framework of EFT requires that we consider all such operators consistent with the symmetries and matter content of the BSM theory.

As with all operators, Eq. (1.30) changes with scale according to dimensional analysis. Neglecting quantum fluctuations (i.e., in the absence of anomalous dimensions), operator evolution is simply the result of changing normalization. The separation of scales therefore suppresses irrelevant

couplings according to

$$\lambda[\Lambda_{\rm IR}] \simeq \lambda[\Lambda_{\rm UV}] \left(\frac{\Lambda_{\rm IR}}{\Lambda_{\rm UV}}\right)^{\Delta_{\rm BSM}+\Delta_{\rm SM}-4}, \tag{1.31}$$

where $\Lambda_{\rm IR}$ is some low energy scale, e.g., the composite scale itself. Eq. (1.31) reveals the basic difficulty that exists in composite models. Generic operators must be small, since they induce flavor-changing neutral currents (which experiments constrain tightly). At the same time, operators involving to the top quark must remain large in order generate a large mass.

Suppressing generic operators requires a large separation of scales ($\Lambda_{\rm IR}/\Lambda_{\rm UV} \ll 1$). To combat this suppression, operators which couple to the top quark must have nearly vanishing exponents ($\Delta_{\rm BSM} + \Delta_{\rm SM} - 4 \simeq 0$) in Eq. (1.31). When the top quark couples quadratically to new operators ($[\psi\psi] = \Delta_{\rm SM} \sim 3$), the dimension of the high-energy operator must be nearly unity ($\Delta_{\rm BSM} \sim 1$). Unfortunately, this scheme reintroduces issues with naturalness, since rigorous results show that the free scalar is the only operator with dimension exactly unity [117]. Recent results from conformal field theory establish new bounds for scalar operators with dimension near unity [125], clarifying some of the challenges with this setup.

In partial compositeness—where the top quark couples linearly to new physics ($[\psi] = \Delta_{\rm SM} \sim 3/2$)—the high-energy operator must have dimension five-halves ($\Delta_{\rm BSM} \sim 5/2$). If the new operator contains three fermions, the engineering dimension is nine-halves ($[\psi\psi\psi] = \Delta_{\rm BSM} \sim 9/2$). Reconciling this difference requires large anomalous dimensions, which may be difficult to produce in explicit models. However, in contrast to the case of quadratic couplings, no *a priori* obstruction exists to an operator with such dimensions. Such dimensions seem possible in holographic theories [45], but it remains unknown if they are also possible in strictly four-dimensional theories.

From the perspective of lattice gauge theory, many avenues exist for studying composite models. The first approach, adopted in this thesis, is simply to determine the particle spectrum. Directly computing the anomalous dimensions of composite operators would be an interesting second step. Some perturbative work has been done in this direction [64]. However, non-perturbative determination of the anomalous dimension is a technically challenging problem on the lattice which

we shall not pursue further in this thesis.

1.3.1 Ferretti's Model

This thesis explores the possibility that the Higgs arises from the strong dynamics of some hypercolor theory based on the gauge group $\mathcal{G}_{\rm HC}$ as a (pseudo) Goldstone boson associated with a spontaneously broken global symmetry $\mathcal{G}_{\rm F} \to \mathcal{H}_{\rm F}$. Consistency with low-energy physics requires that the unbroken global symmetry $\mathcal{H}_{\rm F}$ contain the custodial symmetry group, $\mathcal{G}_{\rm cus}$, and the familiar symmetry group of the Standard Model, $\mathcal{G}_{\rm SM}$:

$$\mathcal{H}_{\rm F} \supset \mathcal{G}_{\rm cus} \equiv {\rm SU}(3)_c \times {\rm SU}(2)_L \times {\rm SU}(2)_R \times {\rm U}(1)_X \tag{1.32}$$

$$\supset \mathcal{G}_{\rm SM} \equiv {\rm SU}(3)_c \times {\rm SU}(2)_L \times {\rm U}(1)_Y. \tag{1.33}$$

In order to single out concrete realizations of this idea, additional physical assumptions are required. Ferretti and Karateev recently classified four-dimensional, asymptotically free UV completions of the Standard Model using five assumptions [77]:

(1) The absence of gauge anomalies in the hypercolor sector $\mathcal{G}_{\rm HC}$, signaling a consistent theory.

(2) The possibility of symmetry breaking according to $\mathcal{G}_{\rm F} \to \mathcal{H}_{\rm F} \supset \mathcal{G}_{\rm cus}$, allowing the Standard Model to be embedded as an unbroken global symmetry.

(3) The absence of 't Hooft anomalies for $\mathcal{G}_{\rm cus}$, allowing consistent inclusion of the dynamics of the Standard Model via gauging.

(4) The existence of a Higgs field in the coset $\mathcal{G}_{\rm F}/\mathcal{H}_{\rm F}$ with charges $(\mathbf{1}, \mathbf{2}, \mathbf{2})_0$ under $\mathcal{G}_{\rm cus}$.

(5) The presence of fermionic hypercolor-singlet operators with the same Standard Model quantum numbers as the third generation of quarks, $(\bar{\mathbf{3}}, \mathbf{2})_{-1/6}$ and $(\mathbf{3}, \mathbf{1})_{2/3}$ under $\mathcal{G}_{\rm SM}$, allowing for a partially composite top quark.

One particularly promising model in their classification is a hypercolor theory with gauge group $\mathcal{G}_{\rm HC} = {\rm SU}(4)$, which was the subject of a more detailed paper by Ferretti [75]. An interesting feature

of this model is the presence of fermions in two different representations of the gauge group: the fundamental **4** and the two-index antisymmetric **6**, a real representation. More precisely, Ferretti's model contains six left-handed Weyl fermions in the **4** and five left-handed Weyl fermions in the **6**. The global symmetry then breaks according to

$$\frac{\mathcal{G}_{\mathrm{F}}}{\mathcal{H}_{\mathrm{F}}} = \left(\frac{\mathrm{SU}(3) \times \mathrm{SU}(3)'}{\mathrm{SU}(3)_c}\right) \times \left(\frac{\mathrm{SU}(5)}{\mathrm{SO}(5)}\right) \times \left(\frac{\mathrm{U}(1)_X \times \mathrm{U}(1)'}{\mathrm{U}(1)_X}\right). \tag{1.34}$$

The custodial symmetry of the Standard Model remains unbroken because SO(5) contains SO(4), which is locally isomorphic to $\mathrm{SU}(2)_L \times \mathrm{SU}(2)_R$. Lattice simulations of this SU(4) gauge theory form the heart of this thesis, albeit with slightly modified matter content.

So far we have only discussed the dynamics of the hypercolor theory and the unbroken global symmetry structure. In addition the strong dynamics of $\mathcal{G}_{\mathrm{HC}}$, Ferretti's model also includes the gauge dynamics of the Standard Model. From a theoretical perspective, one imagines first solving the dynamics of $\mathcal{G}_{\mathrm{HC}}$ (e.g., with a lattice simulation, as in this thesis) and then "switching on" the $\mathcal{G}_{\mathrm{SM}}$ dynamics as a small perturbation. Perturbative interactions with the fields of the Standard Model generate an effective potential for the Higgs (which is an element of Goldstone multiplet SU(5)/SO(5)). If this potential has the correct properties, the top quark misaligns the vacuum and triggers the formation of a vacuum expectation value for the Higgs and breaks electroweak symmetry $\mathrm{SU}(2)_L \times \mathrm{U}(1)_Y \to \mathrm{U}(1)_{\mathrm{EM}}$.

Ferretti computed the effective potential for the Higgs to lowest order and found that it has the form

$$V(h) \propto \alpha \cos(2h/f) - \beta \sin^2(2h/f), \tag{1.35}$$

where α and β are low-energy constants encoding the contributions of the electroweak gauge bosons and top quark, respectively [75]. The precise values of these low-energy constants depend on the dynamics of the hypercolor theory. The minimum of this potential occurs for $\cos(2h/f) = -\alpha/2\beta$, i.e., for $\sin^2(2h/f) = 1 - (\alpha/2\beta)^2$. As we shall discuss more below, the figure of merit in composite

Higgs models is the dimensionless ratio

$$\xi = (v/f)^2 = \sin^2\left(\langle h \rangle / f\right), \tag{1.36}$$

which measures the departure of Higgs physics from the Standard Model. With this definition, we learn that

$$\xi \simeq \frac{1}{4}\left(1 - \frac{\alpha}{2\beta}\right)^2. \tag{1.37}$$

This expression shows the fine-tuning parameter ξ depends not only the scale of new dynamics but also on consistency conditions of the hypercolor theory itself. Lattice simulations can investigate self-consistency relations like this by computing low-energy constants.

1.3.2 The Minimal Composite Higgs Model

Low-energy effective theory is the natural starting point for phenomenology of composite Higgs models. EFT discussions begin with the choice of the coset $\mathcal{G}_{\mathrm{F}}/\mathcal{H}_{\mathrm{F}}$ from which the Higgs boson emerges as a pseudo Goldstone boson. In direct analogy to chiral perturbation theory and QCD, this approach contains many free parameters (in the form of undetermined low-energy constants) and remains largely agnostic about the underlying high-energy dynamics of the hypercolor theory. However, the perspective of EFT offers a close connection to collider searches for new physics and enjoys a degree of model independence.

The coset SO(5)/SO(4) sometimes goes by the name of the *minimal composite Higgs model*. Although not directly applicable to the lattice model of this thesis, the minimal composite Higgs model nevertheless contains some universal features which are expected in more complicated scenarios. It is therefore worthwhile to review the important features of this toy model, following the discussion of Panico and Wulzer [121].

Let us suppose that some strongly interacting hypercolor gauge theory confines and breaks the global symmetry $\mathcal{G}_{\mathrm{F}}/\mathcal{H}_{\mathrm{F}} = \mathrm{SO}(5)/\mathrm{SO}(4)$. Because SO(4) is locally isomorphic to $\mathrm{SU}(2)_L \times \mathrm{SU}(2)_R$, the unbroken symmetry includes the custodial symmetry of the Standard Model. The Goldstone bosons $\pi_{\hat{a}} T^{\hat{a}}$ are elements of the coset SO(5)/SO(4).

The general CCWZ construction again provides the correct EFT Lagrangian, with or without gauge interactions of the unbroken $\mathcal{H}_{\rm F} = {\rm SO}(4)$ generators (Appendix A.4 describes the general CCWZ construction). To include gauge interactions, one simply promotes the $\mathcal{G}_{\rm F}$-covariant derivative $\mathbf{d}_\mu[\pi]$ to a gauge- and $\mathcal{G}_{\rm F}$-covariant derivative $\mathbf{d}_\mu[\pi, A]$ using

$$\partial_\mu \longmapsto D_\mu = \partial_\mu - iA_\mu, \tag{1.38}$$

where A_μ denotes the gauge field(s) of the unbroken generators. As shown in Appendix A.5, the tensor $\mathbf{d}_\mu$ for the coset SO(5)/SO(4) takes the form:

$$\mathbf{d}_\mu = \left[\sqrt{2}\left(\frac{1}{\pi}\sin\left(\frac{\pi}{f}\right) - \frac{1}{f}\right)\frac{\pi\cdot\partial_\mu\pi}{\pi^2}\pi_{\hat{a}} - \frac{\sqrt{2}}{\pi}\sin\left(\frac{\pi}{f}\right)(\partial_\mu\pi_{\hat{a}})\right]T^{\hat{a}}, \tag{1.39}$$

where $\pi = \sqrt{\pi_{\hat{a}}\pi^{\hat{a}}}$. Squaring this quantity and tracing then yields the most general two-derivative Lagrangian:

$$\mathcal{L} = \frac{f^2}{4}\,{\rm Tr}\,\mathbf{d}_{\mu,\hat{a}}\mathbf{d}^{\mu,\hat{a}} \tag{1.40}$$

$$= \frac{f^2}{2}\left[\left(\left(\frac{\pi}{2}\right)^2 - \sin^2\left(\frac{\pi}{f}\right)\right)\left(\frac{\pi\cdot\partial_\mu\pi}{\pi^2}\right)^2 + \sin^2\left(\frac{\pi}{f}\right)\frac{\partial_\mu\pi\cdot\partial^\mu\pi}{\pi^2}\right]. \tag{1.41}$$

Although this expression is indeed rather complicated, the remarkable fact that it can be written exactly reveals generic features expected in any composite model. A slight change of notation aids the discussion. Consider therefore the Higgs field, defined as a doublet of $SU(2)_L \subset SO(4)$:

$$H = \begin{pmatrix} h_u \\ h_d \end{pmatrix} = \frac{1}{\sqrt{2}}\begin{pmatrix} \pi_2 + i\pi_1 \\ \pi_4 + i\pi_3 \end{pmatrix}, \tag{1.42}$$

which evidently satisfies $\pi = \sqrt{2}\,|H|$ where $|H| = \sqrt{H^\dagger H}$. Coupling to the gauge fields and using the fact that $\pi\cdot D_\mu\pi = \pi\cdot\partial_\mu\pi$ (since the generators of SO(4) are antisymmetric and π is bosonic), the Lagrangian becomes:

$$\mathcal{L} = \frac{f^2}{2}\left[\sin^2\left(\frac{\sqrt{2}\,|H|}{f}\right)\frac{D_\mu H^\dagger D^\mu H}{|H|^2} + \left(\frac{2\,|H|^2}{f^2} - \sin^2\frac{\sqrt{2}\,|H|}{f}\right)\left(\frac{\partial_\mu\,|H|^2}{2\,|H|^2}\right)^2\right] \tag{1.43}$$

First, we see that the Higgs field often appears in combination with the decay constant f of the hypercolor sector: $|H|/f$. After electroweak symmetry breaking, the figure of merit becomes

$\xi = (v/f)^2$, where $v = 246$ GeV is the Higgs vacuum expectation value. The ratio ξ is inversely related to the generic energy scale of compositeness, as measured by f. Second, in the limit of a very heavy composite sector ($\xi \to 0$), one recovers the usual Higgs-gauge interactions of the Standard Model:

$$\mathcal{L} \to |D_\mu H|^2 \,. \tag{1.44}$$

Third, we see a pathway to experimental investigation of composite Higgs models. Even if resonances from the hypercolor sector are too heavy to produce directly in collier experiments, composite Higgs models generically predict small corrections to Standard Model couplings. These corrections are are proportional to powers of ξ. In this way, high-precision experiments can constrain the space of possible composite Higgs models. All three of these lessons are expected to apply in a generic composite Higgs model $\mathcal{G}_{\rm F}/\mathcal{H}_{\rm F}$.

1.3.3 The Nature of Experimental Predictions

The experimental search for physics beyond the Standard Model is a vast subject, ranging from tabletop atomic experiments in Boulder [37] to enormous collider experiments at the Large Hadron Collider [1]. The research of this thesis necessarily fits into a large scientific story involving not only lattice gauge theorists., but also experimentalists and phenomenologists. Combining theoretical arguments with state-of-the-art experimental constraints is the fascinating and technical subject. Some recent work, relevant to the simulations of this thesis, exists in this direction [70, 76]. Unfortunately, it exceeds the scope of this thesis to discuss this story at length. This section attempts to compensate for this deficiency by explaining, in the simplest possible terms, the nature of the experimental predictions emerging from these simulations.

As we saw in Sec. 1.3.2, a generic composite Higgs model modifies coupling(s) of the Higgs to the other fields in the Standard Model. The dimensionless parameter $\xi = (v/f)^2$ controls this shift, where $v = 246$ GeV is the known Higgs vacuum expectation value and f is the new compositeness scale. By measuring the Higgs coupling(s)—for instance, through decay rates and

branching ratios—experiments provide upper bounds on possible values of ξ.

Theoretical predictions from a lattice simulation are always dimensionless ratio of physical quantities. For example, a lattice prediction of the mass spectrum can be phrased in units of the compositeness scale as (M/f). Then, given an upper bound for ξ, the lattice result gives a lower bound on the masses of new particles:

$$M \text{ (GeV)} \gtrsim \left(\frac{M}{f}\right)_{\text{thy.}} \times \left(\frac{v}{\sqrt{\xi}}\right)_{\text{exp.}}. \tag{1.45}$$

Statements like these are the easy to understand. Given a preferred experimental value for ξ, the theory predicts new particles for discovery in direct detection experiments at high energies.

In Ferretti's model (but not all composite Higgs models), the top quark is partially composite. The fact that the top quark has substructure will induce small changes in its decay width and decay properties, which experiment also constrains. Because the precise nature of such predictions is the subject of current research, we shall not discuss it further here.

Other predictions are possible with lattice simulations, although they are usually more abstract and more difficult to compute. For instance, in Ferretti's model, we learned in Eq. (1.37) that the parameter self-consistency conditions also determine the value of ξ in terms of low-energy constants of the composite Higgs model. Computing these constants in a lattice simulation would indicate a preferred value for ξ, which could be compared directly to experimental bounds.

Chapter 2

Lattice Gauge Theory: An Overview

2.1 Motivation

Much of the conceptual and technical difficulty of quantum field theory arises from regulators to ensure that physical predictions of the theory are finite. In fact, the need for such regulators is easily understood with a little bit of hindsight. First, consider the fact that many field theories of interest (like QCD with massless fermions) are classically conformal, possessing no intrinsic length scale. Nevertheless, general QFTs exhibit both scale dependence (i.e., running couplings) and massive bound states (i.e., dimensional transmutation). In order to compute either of these effects starting from a classically scale-invariant Lagrangian, one should expect to introduce some reference scale or regulator. Second, the quantum mechanical partition function receives contributions from violent fluctuations across all distance scales. Rendering this quantity finite requires limits on the lowest-energy and highest-energy fluctuations allowed, that is, the introduction of regulators.

Lattice-regulated QFT, originally due to Wilson [143], approximates spacetime as a finite four-dimensional lattice, with physical fields taking values on the links and nodes. By virtue its finite size V and lattice-spacing a, this procedure introduces hard cutoffs in both the IR and UV. As usual, physical results follow the removal of the regulators in the continuum ($a \to 0$) and infinite-volume ($V \to \infty$) limits. Most importantly, the lattice preserves gauge invariance even at finite lattice spacing and finite volume.

Presently, only the lattice gives complete, non-perturbative definition to strongly coupled QFTs like QCD, and only the lattice yields controlled and systematically improvable computations

at strong coupling. From both a practical and theoretical perspective, lattice gauge theory simulations are therefore the most reliable way to answer quantitative questions about the spectrum of strongly coupled QFTs. However, tools like the quark model, chiral perturbation theory, and large-N_c provide additional context and intuition for lattice results. This thesis shall freely use techniques from all three.

Lattice gauge theory is by now a mature field with many textbooks. Learning the subject for the first time, I found the following books particularly useful: DeGrand and DeTar [59]; Gattringer and Lang [82]; Knechtli, Günter, and Peardon [105]; and Montvay and Münster [119]. Even when not explicitly referenced below, their presentations have heavily influenced much of the discussion in the rest of this chapter.

2.2 Technical Formulation

The usual continuum action of QCD is the sum of a gauge action S_G and a fermion action S_F, given by

$$S_G = \frac{1}{2g^2} \int d^4x \, \mathrm{Tr} \left[F_{\mu\nu}(x) F^{\mu\nu}(x) \right], \tag{2.1}$$

$$S_F = \int d^4x \bar{\psi} \not{D} \psi, \tag{2.2}$$

where $\not{D} = \gamma^\mu(\partial_\mu + igA_\mu)$ is the familiar gauge-covariant derivative. On the lattice we find it convenient to work with slightly more complicated actions, which reduce to the previous expression in the continuum limit. The best motivation for lattice actions comes from effective field theory. In this spirit, Eqs. (2.1) an (2.2) are simply the most general gauge-invariant actions containing only marginal and relevant operators.[1] Additional irrelevant operators (i.e., those with engineering

[1] In fact another marginal term is also possible, the CP-violating "theta term,"

$$\mathcal{S}_{\mathrm{CP}} = \theta \int d^4x \ \mathrm{Tr}[\epsilon^{\mu\nu\rho\sigma} F_{\mu\nu} F_{\rho\sigma}]. \tag{2.3}$$

Experiments, e.g., measuring the electron dipole moment of the neutron constrain this term to satisfy $\theta \lesssim 10^{-10}$. The unexplained smallness of this number goes by the name of the Strong CP Problem.

dimension $\Delta > 4$) are also possible. The sole dimension-five operator,

$$S^{(5)} \sim \frac{1}{\Lambda} \int d^4x \bar{\psi} \not{D} \not{D} \not{D} \psi \tag{2.4}$$

$$= \frac{1}{\Lambda} \int d^4x \bar{\psi} \left(D^2 + \frac{1}{2} \sigma_{\mu\nu} F^{\mu\nu} \right) \psi, \tag{2.5}$$

will play a key role in the construction of a lattice action below.

In continuum field theory, the spurious transformation properties of $\bar{\psi} \not{\partial} \psi$ under local symmetries motivative the introduction of the gauge-covariant derivative. The associated gauge field is defined in the *algebra* of the gauge group, which encodes the infinitesimal structure of the symmetry. Because the derivative compares infinitesimally close points in spacetime, the presence of the algebra is sensible in this context. The situation differs on the lattice, where adjacent spacetime points are separated by a finite distance, and matter fields are defined at each point on the lattice. In this case, a more economical description therefore arises from group elements corresponding to finite transformations. The continuum provides the necessary motivation, where the Wilson-line operator

$$G_{\mathcal{C}} = \mathcal{P} \exp \left(i \int_{\mathcal{C}} dx \cdot A \right) \tag{2.6}$$

is a group-valued functional of the path $\mathcal{C}$ connecting two points in spacetime ($\mathcal{P}$ denotes the path-ordered exponential). The lattice Wilson line operator is defined at site n extending in the direction μ as

$$U_\mu(n) = \exp(iaA_\mu(n)). \tag{2.7}$$

Because this quantity is naturally associated with the link between sites n and $n + \mu$, it is referred to as a gauge link. Gauge links can be used to define plaquettes, the lattice analogues of Wilson loops,

$$U_{\mu\nu}(n) = U_\mu(n) U_\nu(n + \hat{\mu}) U_{-\mu}(n + \hat{\mu} + \hat{\nu}) U_{-\nu}(n + \hat{\nu}) \tag{2.8}$$

$$= U_\mu(n) U_\nu(n + \hat{\mu}) U_\mu(n + \hat{\nu})^\dagger U_\nu(n)^\dagger. \tag{2.9}$$

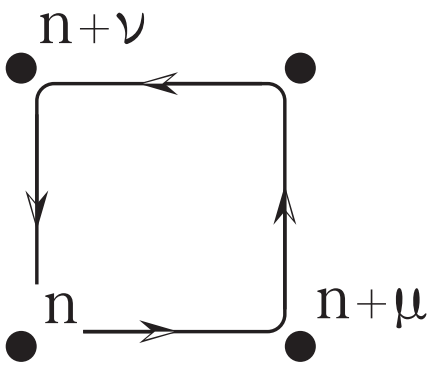

Figure 2.1: A diagrammatic representation of a plaquette $U_{\mu\nu}(n)$, the lattice analogue of a Wilson loop. The dots represent the nodes of the lattice. Each arrowhead represents a gauge link U. The free lines at site n indicate the un-contracted group indices in Eq. (2.9).

Figure 2.1 shows a diagrammatic representation of a plaquette. The famous Wilson gauge action is simply a sum over plaquettes:

$$S_G[U] = \frac{2}{g^2} \sum_n \sum_{\mu<\nu} \Re \operatorname{Tr} \left[\mathbb{1} - U_{\mu\nu}(n)\right]. \tag{2.10}$$

By direct computation with the help of the Baker–Campbell–Hausdorff formula (see Eq. (A.15)), one discovers that

$$S_G[U] = \frac{a^4}{2g^2} \sum_n \sum_{\mu,\nu} \operatorname{Tr} \left[F_{\mu\nu}(n) F^{\mu\nu}(n)\right] + \mathcal{O}(a^2). \tag{2.11}$$

In other words, the Wilson gauge action agrees with the familiar continuum version up to lattice artifacts of $\mathcal{O}(a^2)$, which vanish in the continuum ($a \to 0$) limit.

In the fermion sector, the naive fermion action approximates the gauge-covariant derivative with a gauge-covariant symmetric finite difference:

$$S_F = a^4 \sum_n \sum_\mu \gamma^\mu \bar{\psi}(n) \left(\frac{U_\mu(n)\psi(n+\hat{\mu}) - U_{-\mu}(n)\psi(n-\hat{\mu})}{2a} \right) + m\bar{\psi}(n)\psi(n). \tag{2.12}$$

This discretization suffers from two issues. First, this action possesses an accidental surfeit of low-energy modes known as fermion doublers. Second and more benignly, the naive fermion action only approaches the continuum limit up to $\mathcal{O}(a)$ lattice artifacts. Because physical predictions emerge

only in the continuum limit, it is desirable to approach this limit as efficiently as possible and at least as quickly as the Wilson gauge action. Including additional irrelevant operators in the action solves both issues.

As we saw above, a single dimension-five operator $\propto \not{D}^2$ exists. The lattice action containing this term goes by the name of the Wilson fermion action with clover improvement; its explicit form is:

$$\begin{aligned} S_{\mathrm{W}} = \sum_n \bar{\psi}_n \psi_n - \kappa \sum_{n,\mu} \left[\bar{\psi}_n (r - \gamma_\mu) U_\mu(n) \psi_{n+\hat{\mu}} + \bar{\psi}_n (r + \gamma_\mu) U_\mu^\dagger (n - \hat{\mu}) \psi_{n-\hat{\mu}} \right] \\ - r\kappa c_{\mathrm{SW}} \frac{1}{2} \sum_{n,\mu,\nu} \bar{\psi}_n \sigma_{\mu\nu} C_{\mu\nu} \psi_n. \end{aligned} \tag{2.13}$$

The object $C_{\mu\nu}$ is a combination of gauge links defined to reduce to the field strength in the continuum limit $C_{\mu\nu} = a^2 F_{\mu\nu} + \mathcal{O}(a^4)$, a definition containing freedom in the structure of the higher-order terms. Because of this freedom, the lattice community has in practice used many different forms for $C_{\mu\nu}$, with possible forms appearing in the standard texts, e.g., [59, 82]. As one particular concrete example, consider

$$C_{\mu\nu} = -\frac{i}{8a^2} \left(Q_{\mu\nu}(n) - Q_{\nu\mu}(n) \right) \tag{2.14}$$

$$Q_{\mu\nu} = U_{\mu,\nu}(n) + U_{\nu,-\mu}(n) + U_{-\mu,-\nu}(n) + U_{-\nu,\mu}(n). \tag{2.15}$$

This combination of plaquettes resembles a four-leaf clover, whence the name "clover term." Figure 2.2 shows a diagram of the clover term in a fixed $\mu\nu$-plane. In Eq. (2.13), r is the so-called Wilson parameter, and c_{SW} is the clover coefficient (after Sheikholeslami and Wohlert [135]). Throughout this thesis we shall set the clover coefficient and the Wilson parameter to unity, a choice motivated by tree-level matching to the continuum [141, 142].

The final parameter in Eq. (2.13) is the "hopping parameter" κ, which serves as a proxy for the bare mass. To see this connection more clearly, let us consider the Wilson action in the limit

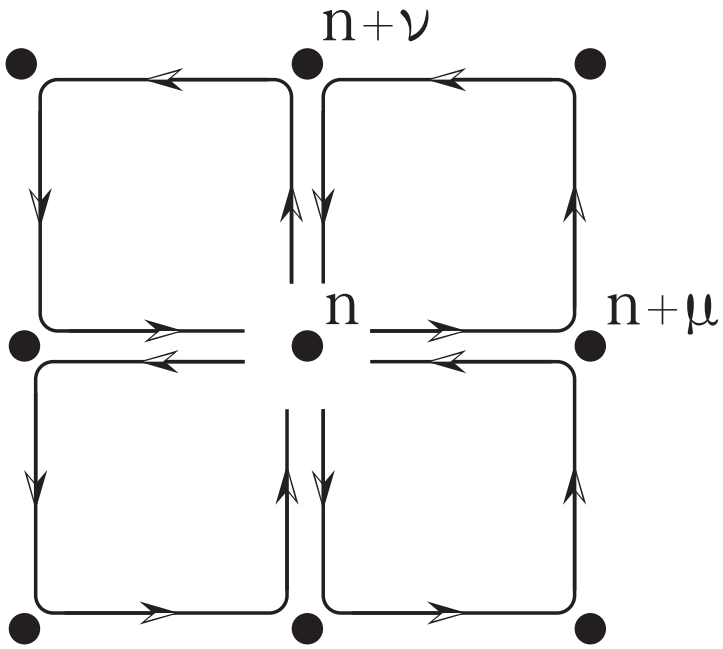

Figure 2.2: A diagrammatic representation of the object $Q_{\mu\nu}$ which appears in the clover term, in a fixed $\mu\nu$-plane. The dots represent the nodes of the lattice. Each arrowhead represents a gauge link U. Gauge links moving in opposite directions between the same nodes are related by hermitian conjugation.

of free fermions, i.e., neglecting interactions with the gauge links:

$$S_{\mathrm{W}}^{(\mathrm{free})} = \sum_n \bar{\psi}_n \psi_n - \kappa \sum_{n,\mu} \left[\bar{\psi}_n (1-\gamma_\mu) \psi_{n+\hat{\mu}} + \bar{\psi}_n (1+\gamma_\mu) \psi_{n-\hat{\mu}} \right] \tag{2.16}$$

$$= \sum_n \bar{\psi}_n \psi_n - \kappa \sum_{n,\mu} \left[2\bar{\psi}_n \psi_n - 2\bar{\psi}_n \gamma_\mu \partial_\mu \psi_n + \cdots \right] \tag{2.17}$$

$$= 2\kappa \sum_n \left[\bar{\psi}_n \partial\!\!\!/ \psi_n + \frac{1}{2} \left(\frac{1}{\kappa} - 8 \right) \bar{\psi}_n \psi_n + \cdots \right] \tag{2.18}$$

$$\equiv 2\kappa \sum_n \left[\bar{\psi}_n \partial\!\!\!/ \psi_n + m \bar{\psi}_n \psi_n + \cdots \right]. \tag{2.19}$$

Therefore, up to an immaterial field normalization factor, we see that the fermion mass is related to the hopping parameter by

$$am = \frac{1}{2} \left(\frac{1}{\kappa} - 8 \right) \iff \kappa^{-1} = 2(am + 4). \tag{2.20}$$

A lattice simulation with Wilson fermions begins by specifying the bare inverse gauge coupling (i.e., the prefactor of the Wilson action) and the bare hopping parameter κ. For the free fermions we have

considered, the massless limit corresponds to a critical value of the hopping parameter $\kappa_c = 1/8$. The value of the critical point shifts in the presence of interactions. In the strong-coupling limit, $\kappa_c = 1/4$ [144, 93]. In general, the fermion mass and the hopping parameter are inversely related, with vanishing κ corresponding to arbitrarily heavy, static fermions.

Because simulations occur on finite four-dimensional lattices, boundary conditions deserve at least a passing remark. In brief, the precise boundary conditions are expected to be irrelevant in the thermodynamic ($V \to \infty$) limit. Practical simulations often employ periodic boundary conditions in the spatial directions. According to the thermal partition function, finite temporal extent corresponds to a finite temperature. Because of the trace in the thermal partition function,

$$Z_T = \mathrm{Tr}\, e^{-T\hat{H}}, \tag{2.21}$$

bosons should be periodic in time, while fermions should be anti-periodic in time.

2.3 Markov Chain Monte Carlo

A quantum field theory is defined according to the path integral

$$Z[J] = \int [d\phi] \exp\left(-S_E[\phi, J]\right), \tag{2.22}$$

where S_E denotes a Euclidean action in terms of arbitrary fields ϕ and sources J. Computing this integral constitutes a complete solution of the QFT. Because lattice simulations include quantum fluctuations to all orders, the usual perturbative diagrammatic expansion is not the most useful way to think about $Z[J]$. Instead, one interprets the partition function as a weighted average over field space. Two basic ideas are necessary to compute the full path integral in practice: importance sampling and molecular dynamics.

Importance sampling is common to all Monte Carlo approaches to integration. Because the path integral is a high-dimensional integral, brute-force evaluation of all possible field configurations is not feasible. As a simple example, consider the Ising model, with spins on each lattice site taking the values ± 1. For a d-dimensional lattice with N^d total sites, the dimension of the field space $\{\phi\}$

is exponentially large:

$$\dim\{\phi\} = 2^{N^d} = \exp\left(N^d \log 2\right). \tag{2.23}$$

Moreover, the Boltzmann factor $\exp\left(-S_E[\phi, J]\right)$ exponentially suppresses most field configurations. To bypass this problem, instead of sampling configurations randomly and weighting them with a Boltzmann factor, importance sampling draws configurations from a Boltzmann distribution and weights them evenly. How can we draw configurations from such a distribution?

Molecular dynamics generates configurations according to the Boltzmann distribution and is based on the trivial introduction of an additional gaussian field p:

$$\int [d\phi] \exp\left(-S_E[\phi]\right) = \int [d\phi][dp] \exp\left(-\frac{p^2}{2} - S_E[\phi]\right) \tag{2.24}$$

$$\equiv \int [d\phi][dp] \exp\left(-H(p,\phi)\right). \tag{2.25}$$

The quantum path integral is thus equivalent to a statistical partition function in one additional (fictitious) dimension. But Boltzmann's key insight in statistical mechanics allows us to compute this quantity: ensemble averages equal time averages. Therefore it suffices to solve the classical Hamiltonian equations

$$\dot{p} = -\frac{\partial H}{\partial \phi} \tag{2.26}$$

$$\dot{\phi} = \frac{\partial H}{\partial p} \tag{2.27}$$

of the "molecular dynamics" of the system. Evidently the complicated dynamical behavior of the system in the fictitious fifth dimension encodes the full structure of the 4-dimensional quantum fluctuations. This program requires many technical considerations in order to be a practical simulation method for realistic field theories. Briefly, numerical integration of the Hamilton's equations should be symplectic (in the sense of preserving the natural notion of area on the classical phase space) and time-reversal symmetric. Dynamical fermions present their own technical challenges, which are beyond the scope of this thesis to describe.

The abstract framework of Markov Chain Monte Carlo unites importance sampling and molecular dynamics. Consider a Markov process, i.e., a random sequence of configurations $U_0 \to$

$U_1 \to \cdots U_n$ with the transition probability

$$P(U_n = U' | U_{n-1} = U) = T(U'|U) \tag{2.28}$$

satisfying positivity and normalization requirements

$$0 \leq T(U'|U) \leq 1 \tag{2.29}$$

$$\sum_{U'} T(U'|U) = 1. \tag{2.30}$$

Suppose that, in addition to the transition probability T, this sequence also has a limit distribution $P(U)$. After "thermalizing" ($n \to \infty$), the sequence must be reversible in the following sense: the probability to obtain a configuration U' (from any initial configuration U) equals the probability to leave the configuration U' (and go to any final configuration U). Mathematically, this reversibility condition corresponds to the balance equation,

$$\sum_{U} T(U'|U)P(U) = \sum_{U} T(U|U')P(U'). \tag{2.31}$$

A sufficient condition for satisfying the balance equation is "detailed balance," i.e., term-by-term equality:

$$T(U'|U)P(U) = T(U|U')P(U'). \tag{2.32}$$

These ideas form the basis of Markov Chain Monte Carlo.

The abstract language of Markov chains provides a practically useful algorithm which unites importance sampling and molecular dynamics. Importance sampling requires an ensemble of configurations sampled from the statistical distribution $P(U) \sim \exp(-S_E[\phi])$. In principle, this ensemble can be realized as a the limit of a Markov process. To define a Markov process which limits to $P(U)$, it suffices to specify a transition probability T satisfying the detailed balance condition of Eq. (2.32). It can be shown that symplectic, time-symmetric integration of Hamilton's equations satisfies

$$T(p, \phi | p', \phi') = T(p', \phi' | p, \phi). \tag{2.33}$$

However, detailed balance also involves the statistical distribution $P(U)$, while molecular dynamics only converges to $P(U)$ in the limit of vanishing integration step size. Fortunately, an auxiliary "Metropolis" acceptance probability restores detailed balance even at finite integration step size [73]:

$$T_{\text{Metroplis}}(U'|U) = \min\left[1, \frac{T(U|U')\,P(U')}{T(U'|U)\,P(U)}\right] \tag{2.34}$$

$$= \min\left[1, \frac{\exp(-S_E[\phi'])}{\exp(-S_E[\phi])}\right] \tag{2.35}$$

$$= \min\left[1, \exp(-\Delta S_E)\right]. \tag{2.36}$$

Therefore, $T_{\text{Metropolis}}$ defines a Markov process which limits to the desired Boltzmann distribution. In the lattice literature, the algorithm based on these ideas is called Hybrid Monte Carlo.

Chapter 3

Lattice spectroscopy

Lattice studies extract physical quantities, like masses and decay constants, from the asymptotic behavior of n-point correlations functions. Two-point functions—propagators—are particularly important, both because of their central role in perturbation theory and because their poles reveal the particle content of the theory. As a reminder of the general argument, consider the spectral representation of the two-point function:

$$\langle 0|\phi(\mathbf{x},0)\phi(\mathbf{0},0)|0\rangle = \int_{m_0^2}^{\infty} dm^2\, \rho(m^2) D^{-1}(\mathbf{x},0;m^2), \tag{3.1}$$

where D^{-1} is the propagator and $\rho(m^2)$ is the positive spectral weight function. Stable one-particle states (of mass m') contribute to the spectral weight with a delta function:

$$\rho(m^2) \propto \delta(m^2 - m'^2). \tag{3.2}$$

Integrating this quantity over the spatial volume projects onto states of zero spatial momentum,

$$C(t) \equiv \int d^3\mathbf{x} \langle 0|\phi(x)\phi(0)|0\rangle = \int_{m_0}^{\infty} dm\, \rho(m^2) e^{-mt} \propto e^{-m_0 t}. \tag{3.3}$$

For large time separations, the lightest state (of mass m_0) dominates. This fact guides lattice computations, where the goal is to measure the asymptotic behavior of $C(t)$ by fitting to sums of exponentials.

The necessary formulae change slightly at finite temperature, i.e., in the presence of a finite temporal direction T. Recall that the thermal partition function is $Z_T = \operatorname{Tr} e^{-T\hat{H}} = \sum_n e^{-TE_n}$. Following Gattringer and Lang [82], let us consider the behavior of a two-point function $C(t) =$

$\langle \mathcal{O}_2(t)\mathcal{O}_1(0)\rangle$ of bosonic operators after summing over spatial slices. Inserting a complete set of states, we find that this functions takes the form

$$C(t) = \langle \mathcal{O}_2(t)\mathcal{O}_1(0)\rangle = \frac{\sum_{m,n}\langle n|\mathcal{O}_2|m\rangle\langle m|\mathcal{O}_1|n\rangle e^{-t\Delta E_m}e^{-(T-t)\Delta E_n}}{1+e^{-T\Delta E_1}+e^{-T\Delta E_2}+\ldots} \tag{3.4}$$

where $\Delta E_n \equiv E_n - E_0$ is written in terms of the ordered energy spectrum $E_{n+1} > E_n$. Note that ΔE_0 vanishes by definition. The normalization by Z_T in the denominator depends only on the total temporal length T of the lattice, not on the difference $(T-t)$. On long lattices where $T \gg 1$, the denominator approximately unity, and so

$$\langle \mathcal{O}_2(t)\mathcal{O}_1(0)\rangle \simeq \sum_{m,n}\langle n|\mathcal{O}_2|m\rangle\langle m|\mathcal{O}_1|n\rangle e^{-t\Delta E_m}e^{-(T-t)\Delta E_n}. \tag{3.5}$$

This expression is useful with the following two observations. First, in the region $t \approx 0$, the quantity $e^{-t\Delta E_m}$ is large, while the quantity $e^{-(T-t)\Delta E_n}$ is vanishingly small except when $m = 0$, in which case it is unity. Second, in the region $t \approx T$, the quantity $e^{-(T-t)\Delta E_n}$ is large, while $e^{-t\Delta E_m}$ is vanishingly small, except when $n = 0$, in which case it is unity. Therefore, we may approximate the two-point function as

$$\langle \mathcal{O}_1(t)\mathcal{O}_2(0)\rangle \simeq \sum_{n}\langle 0|\mathcal{O}_1|n\rangle\langle n|\mathcal{O}_2|0\rangle e^{-t\Delta E_n} + \langle n|\mathcal{O}_1|0\rangle\langle 0|\mathcal{O}_2|n\rangle e^{-(T-t)\Delta E_n}. \tag{3.6}$$

If the two operators are in fact the same ($\mathcal{O}_1 = \mathcal{O}_2$) and Hermitian, the result simplifies even further, and $C(t)$ reveals itself to be a hyperbolic cosine:

$$\langle \mathcal{O}(t)\mathcal{O}(0)\rangle = \sum_n |\langle 0|\mathcal{O}|n\rangle|^2 \left[e^{-t\Delta E_n} + e^{-(T-t)\Delta E_n}\right] \tag{3.7}$$

$$= \sum_n |\langle 0|\mathcal{O}|n\rangle|^2 e^{T/2} \left[e^{(T/2-t)\Delta E_n} + e^{-(T/2-t)\Delta E_n}\right] \tag{3.8}$$

$$= \sum_n |\langle 0|\mathcal{O}|n\rangle|^2 e^{T/2} 2\cosh\left[(T/2-t)\Delta E_n\right]. \tag{3.9}$$

If the operator is not hermitian, a relative minus sign is possible between the two terms, yielding a hyperbolic sine.

So far the discussion has assumed that the operators are bosonic. Important examples include mesonic operators of the form $(\bar{\psi}\Gamma\psi)$. However, lattice studies also employ fermionic operators to

study baryons. Following Montvay and Münster [119], suppose that B and $\bar{B}$ are baryon operators and consider the correlation function $\left\langle B(t)\bar{B}(0)\right\rangle$. For in the limit of infinite temporal extent ($T \to \infty$), the asymptotic behavior is

$$\left\langle B(t)\bar{B}(0)\right\rangle = c_{B^+}\left(1+\gamma_4\right)e^{-tm_{B^+}} + c_{B^-}\left(1-\gamma_4\right)e^{-tm_{B^-}}. \tag{3.10}$$

The parity projection operators $(1\pm\gamma_4)$ arise from the spin sum at zero spatial momentum, which is implicit in the sum over states. The fact that the spin sum occurs at zero spatial momentum follows from summing over spatial slices, as previously. For finite temporal extent T, states propagate in both directions, giving

$$\begin{aligned}\left\langle B(t)\bar{B}(0)\right\rangle = &\left(1+\gamma_4\right)\left[c_{B^+}e^{-tm_{B^+}} - c_{B^-}e^{-(T-t)m_{B^-}}\right] \\ &+ \left(1-\gamma_4\right)\left[c_{B^-}e^{-tm_{B^-}} - c_{B^+}e^{-(T-t)m_{B^+}}\right].\end{aligned} \tag{3.11}$$

Notice the presence of both states, B^+ and B^-, in each term. This feature has a reasonable physical interpretation: a fermion state propagating backward in time reverses its parity. The important observation is that baryon correlation functions at finite T in general contain states of both parities, even after acting with a parity projection operator. Thus, baryon correlation functions are typically asymmetric in the time t. As a physical example from QCD, the nucleon interpolating field

$$N_\alpha = \epsilon_{abc}u^a_\alpha\left(u^{b\mathrm{T}}C\gamma_5 d^c\right) \tag{3.12}$$

couples both to the proton ($E \sim 940$ MeV) and its negative-parity partner ($E \sim 1500$ MeV).

3.1 Fermion propagators

Wick's theorem provides a convenient dictionary for evaluating fermionic path integrals:

$$\left\langle \psi_{i_1}\bar{\psi}_{j_1}\ldots\psi_{i_n}\bar{\psi}_{j_n}\right\rangle_F = \frac{1}{Z}\int[d\psi][d\bar{\psi}]\psi_{i_1}\bar{\psi}_{j_1}\ldots\psi_{i_n}\bar{\psi}_{j_n}e^{-S_E[\bar{\psi},\psi]} \tag{3.13}$$

$$= (-1)^n \sum_{\sigma(1,2,\ldots,n)} D^{-1}_{i_1,j_{\sigma(1)}} D^{-1}_{i_2,j_{\sigma(2)}}\ldots D^{-1}_{i_n,j_{\sigma(n)}}, \tag{3.14}$$

where the sum runs over all possible permutations σ and the subscripts i and j are shorthand for the quantum numbers of the fermion fields. (This result appears in all field theory texts; the present

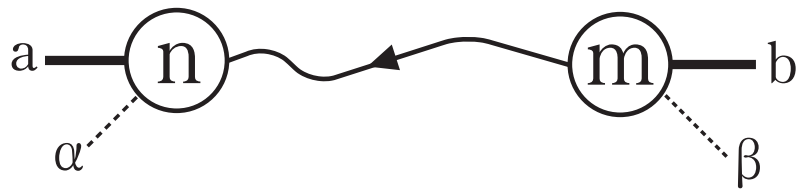

Figure 3.1: A graphical representation of the propagator tensor of Eq. (3.15) from spacetime site m to site n. Color indices are associated to solid external lines. Spin (Lorentz) indices are associated to dotted external lines.

form is from [82]). As usual, D^{-1} denotes the fermion propagator, i.e., the inverse of the quadratic portion of the action. This expression reveals that fermion propagators form the computational backbone of lattice spectroscopy calculations. For a given set of sources, Wick's theorem says that fermions propagate to all possible sinks, with minus signs from permuting fermions.

On the lattice, we view D^{-1} as a matrix connecting two lattice sites n and m:

$$D^{-1} \equiv D^{-1}(n|m)^{a,b}_{\alpha,\beta}\,, \tag{3.15}$$

where a and b are color indices associated with the sites n and m, respectively. Similarly, α and β are the associated Lorentz indices. *A priori*, one must compute this matrix for all sites m and n. Fortunately, for most quantities of interest, one can exploit translational invariance and compute the propagator from a single, fixed source site $m = \bar{m}$ to all other sink sites n. Let $S(m)^{(\bar{m},\bar{\alpha},\bar{a})}_{\alpha,a}$ denote a source vector which selects the site $\bar{m}$ with fixed Lorentz and color structure $\bar{\alpha}$ and $\bar{a}$, respectively. Explicitly for a point source,

$$S(m)^{(\bar{m},\bar{\alpha},\bar{a})}_{\alpha,a} = \delta_{m,\bar{m}}\delta_{\alpha,\alpha_0}\delta_{a,a_0}. \tag{3.16}$$

The propagator from the fixed source (at $\bar{m}$) to the sink (at any other lattice site n) is therefore the product:

$$G(n|\bar{m}) = D^{-1}(n|m)S(m)^{(\bar{m})}. \tag{3.17}$$

Suppose the fermions are charged in a $\dim_f$-dimensional representation of the gauge group in four spacetime dimensions on a lattice with $N_s^3 \times N_t$ sites. For fixed source location $\bar{m}$, G is an array

of $N_s^3 \times N_t \times \dim_f^2 \times 4^2$ complex numbers. For the familiar case of QCD with fermions in the fundamental representation on a modest $16^3 \times 32$ lattice, the computational task requires more than three million complex numbers. The numerical methods for this expensive computational task are well-established and are mostly outside the scope the thesis. However, for the sake of completeness and since these techniques are so important for lattice spectroscopy, Appendix B reviews the essential ideas in some detail.

3.2 Hadron Correlation Functions

In this thesis, we shall be interested in meson and baryon states. The quark model classifies the valence fermion structure of these objects and motivates operators of the form $(\bar{\psi}\Gamma\psi)$ and $\psi(\psi^T C\Gamma\psi)$. Appendix A.2 classifies the symmetry properties of common operators of this form. Wick's theorem, Eq. (3.13), provides the dictionary for constructing correlation functions from propagators. This section examines the concrete forms of correlation functions which arise after the fermion contractions of Wick's theorem.

Consider first a meson correlation function between two operators of the form $\mathcal{O} \sim (\bar{\psi}\Gamma\psi)$. In the case where the fermion ψ and antifermion $\bar{\psi}$ have different flavor quantum numbers, fermion contraction delivers

$$\left\langle (\bar{\psi}(t)\Gamma\psi(t))(\bar{\psi}(0)\Gamma\psi(0)) \right\rangle = -\operatorname{Tr}\left[\Gamma D^{-1}(t|0)\Gamma D^{-1}(0|t)\right]. \tag{3.18}$$

An additional contraction exists in the case of flavor-singlet operators: $\operatorname{Tr}\left[\Gamma D^{-1}(0|0)\right]\operatorname{Tr}\left[\Gamma D^{-1}(t|t)\right]$. Diagrammatic versions of both contractions appear in Figure 3.2. Fermion-line disconnected contractions involve the creation and subsequent annihilation of a fermion at the same site. Such contributions are expensive to compute numerically and are the subject of active research in the lattice QCD community. Because this thesis does not consider flavor-singlet correlation functions, we will not pursue the subject further. Another potential computational concern arises for mesons, since Eq. (3.18) requires both $D^{-1}(t|0)$ and $D^{-1}(0|t)$. Fortunately, all "reasonable" lattice Dirac

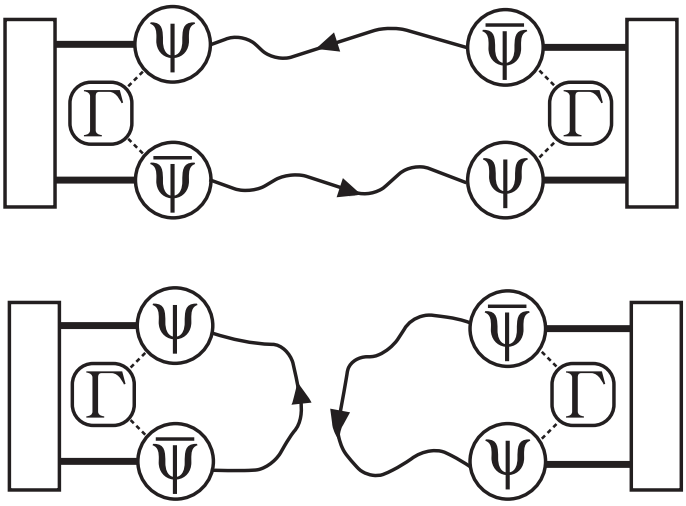

Figure 3.2: A graphical representation of the tensor contractions appearing in meson two-point correlation functions. The lines with arrows and ψ, $\bar{\psi}$ on the ends are the propagators. The dotted lines indicate spin contractions against the Dirac structure Γ. The white hollow boxes indicate color contractions against the Kronecker delta of $\mathrm{SU}(N_c)$. The connected diagram on the top is present for all mesons. The disconnected diagram on the bottom is present, e.g., for flavor singlet mesons.

operators (and the clover Dirac operator, in particular) satisfy a property known as γ_5-hermiticity:

$$D^\dagger = \gamma_5 D \gamma_5 \iff (D^{-1})^\dagger = \gamma_5 D^{-1} \gamma_5. \tag{3.19}$$

Therefore, a single computation of the propagator suffices for a meson two-point correlation function.

The structure of baryon correlation functions is typically more complicated. Consider the case of three distinct fermion flavors: up, down, and strange. For simplicity, take the up and down fermions to be be mass degenerate. Five different contractions patterns are then possible, depending on the location of the strange fermion in the source and sink operators. These five different patterns contain two distinct "topologies" of spin contractions. In the first topology, Wick's theorem connects both fermions in the diquark at the source and sink, forming a closed loop of spinor indices among the propagators. In the second topology, Wick's theorem connects a fermion in the source diquark with the open fermion at the sink. Enumeration of the contractions

Example	s spin	$\bar{s}$ spin	Spin topology
$\left\langle s(u^{\mathrm{T}}C\Gamma d)(\bar{u}C\Gamma\bar{d}^{\mathrm{T}})\bar{s}\right\rangle$	Open	Open	A
$\left\langle u(d^{\mathrm{T}}C\Gamma s)(\bar{d}C\Gamma\bar{s}^{\mathrm{T}})\bar{u}\right\rangle$	Diquark	Diquark	A
$\left\langle u(d^{\mathrm{T}}C\Gamma s)(\bar{u}C\Gamma\bar{d}^{\mathrm{T}})\bar{s}\right\rangle$	Open	Diquark	B
$\left\langle s(u^{\mathrm{T}}C\Gamma d)(\bar{d}C\Gamma\bar{s}^{\mathrm{T}})\bar{u}\right\rangle$	Diquark	Open	B
$\left\langle u(d^{\mathrm{T}}C\Gamma s)(\bar{u}C\Gamma\bar{s}^{\mathrm{T}})\bar{d}\right\rangle$	Diquark	Diquark	B

Table 3.1: Summary of contraction patterns appearing in baryon correlation functions.

is now straightforward and given in Table 3.1. Figure 3.3 shows a diagrammatic representation of the tensor contractions.

3.3 Extracting Physical Results

So far we have described how to compute fermion propagators $D^{-1}(n|m)^{a,b}_{\alpha,\beta}$, contract their color and Lorentz structures, and sum over the lattice sites on each time slice to obtains the scalar correlation function $C(t)$. However, we must still extract the physical content of the theory from this function.

The first step toward this goal is often the construction of so-called effective mass curves. When the correlation function is well-approximated by a single decaying exponential, $C(t) \propto e^{-mt}$, the logarithm of consecutive points furnishes an estimate of the mass:

$$m \simeq \log \frac{C(t)}{C(t+1)}. \tag{3.20}$$

As we saw above, lattice correlation functions often have the form

$$C(t) \simeq Ae^{-mt} \pm Be^{-m(T-t)}. \tag{3.21}$$

An alternative estimate of the mass, which correctly handles the sign from both terms in Eq. (3.21), is based on the observation that $C(t \pm 1) = e^{\pm m}C(t)$. With this observation, we define the effective mass $m_{\mathrm{eff}}(t)$ via

$$m_{\mathrm{eff}} = \operatorname{arccosh}\left(\frac{C(t+1)+C(t-1)}{C(t)}\right). \tag{3.22}$$

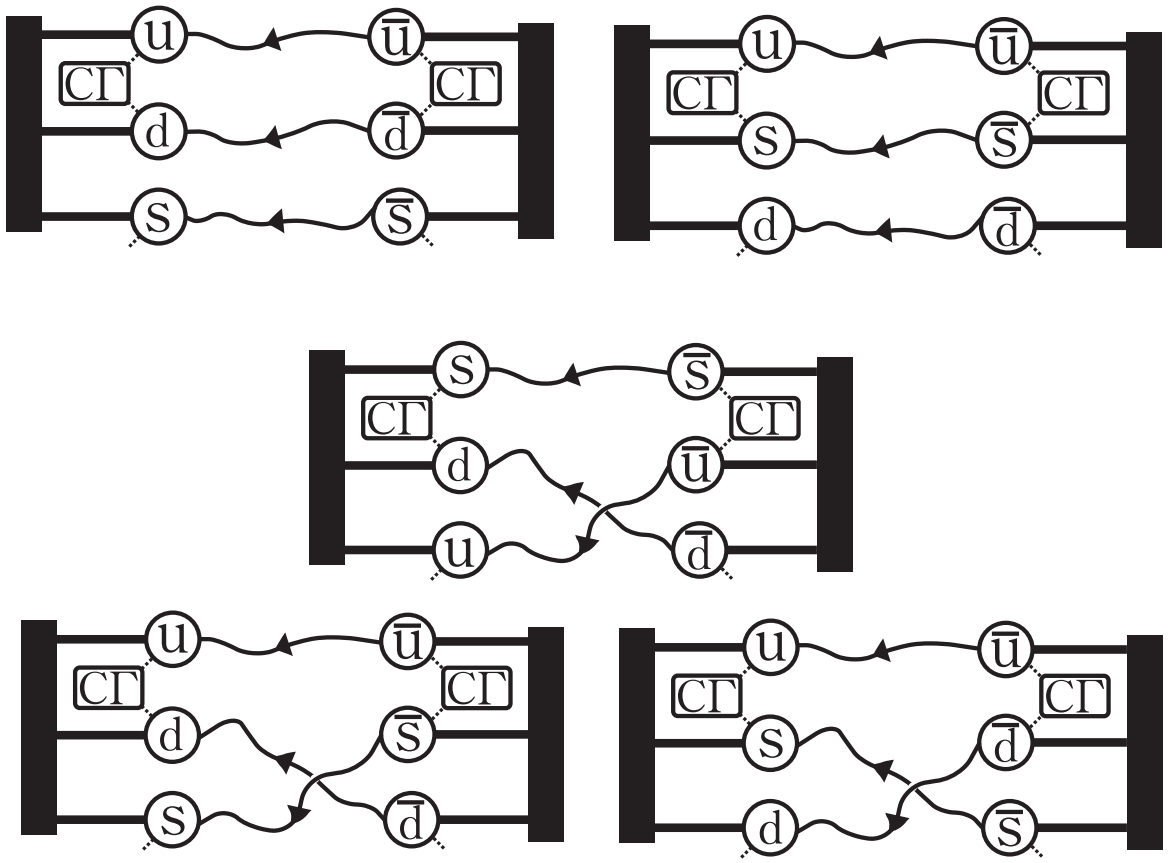

Figure 3.3: A graphical representation of the tensor contractions appearing in baryon two-point correlation functions. The lines with arrows and labels u, d, or s on the ends are the propagators. The dotted lines indicate spin contractions against the Dirac structure Γ. The free dotted lines reflect the fact that the source and sink operators are fermionic. The solid black boxes indicate color contractions against the Levi-Civita tensor of SU(3). The top two diagrams have a closed "spin loop" and correspond to "spin topology A." The bottom three diagrams correspond to "spin topology B."

When a single exponential saturates the correlation function $C(t)$, the effective mass will be a nearly constant curve. In this way, the effective mass can diagnose the presence of lingering contamination from excited states. It is tempting to imagine averaging over a flat "plateau" region in the effective mass to estimate the mass of the corresponding state. While this method is a valuable check on further results, it is inadequate because it fails to include correctly the contribution of correlations.

Instead, the correct solution is to determine the masses and amplitudes from a fit which

includes the correlations. Correlated curve fitting can be phrased as an optimization problem. Suppose that some "experimental" data to be fit are described by their means and a covariance matrix: $(\mathbf{y}, \Sigma)$. Let $\mathbf{y}_{\text{model}}(\mathbf{x}; \mathbf{a})$ be a function of the independent variables $\mathbf{x}$ and the parameter $\mathbf{a}$, which we shall use as a model for data $\mathbf{y}$. Define the χ^2 function as

$$\chi^2 = (\mathbf{y}_{\text{model}} - \mathbf{y})^{\mathrm{T}} \Sigma^{-1} (\mathbf{y}_{\text{model}} - \mathbf{y}). \tag{3.23}$$

The best fit parameters $\mathbf{a}^*$ are chosen to minimize the χ^2 function. A good fit has χ^2/N_{dof} of order unity, meaning that the distance between the model prediction and data is typically order unity, in units of the standard deviation at each point. Many possible methods exist for the actual minimization procedure to determine the best-fit parameters $\mathbf{a}^*$. The Levenberg–Marquardt algorithm is a common choice which works well in practice [110]

Unlike, say, polynomial models, model functions in lattice gauge theory are typically nonlinear functions of the fit parameters. Nonlinear optimization is a difficult, potentially unstable problem. For this reason, lattice studies often employ Bayesian priors to help stabilize large fits. These priors can take many forms. For instance, a lattice determination of the pion decay constant might use the experimental value as input. A study of excited-state spectroscopy might restrict masses to be positive. In computations involving effective field theory, power-counting arguments may provide priors imposing that poorly determined higher-order terms must remain order unity. Regardless of the precise motivation, fits that include priors augment the χ^2 function to

$$\chi^2_{\text{aug}} = \chi^2 + (\mathbf{y}_{\text{model}} - \tilde{\mathbf{y}})^{\mathrm{T}} \tilde{\Sigma}^{-1} (\mathbf{y}_{\text{model}} - \tilde{\mathbf{y}}), \tag{3.24}$$

and then the minimization proceeds as before. In this expression, $\tilde{\mathbf{y}}$ contains the means of the priors and $\tilde{\Sigma}$ the prior covariances.

Other practical considerations arise in the analysis of correlations functions $C(t)$. At early times, contamination from excited states may spoil the asymptotic form of the model function, which often includes one or just a few exponentials. At late times, particularly with baryons, the signal-to-noise ratio of the correlation function deteriorates dramatically. Therefore, one must often

cut on the data by specifying the initial and finial times $[t_{\min}, t_{\max}]$ to include in the fit. We shall refer to such fits as range fits, since they involve fitting over a (contiguous) range of values.

Effective mass curves often motivate reasonable choices of $[t_{\min}, t_{\max}]$ for range fits. However, selecting a particular range fit based solely on visual cues is essentially qualitative. In order to compare different range fits, we require a goodness-of-fit function which quantifies their differences. A useful choice will prefer small χ^2/dof, large fit ranges, and well-determined fit parameters. One such criterion is

$$Q \equiv \frac{p\text{-value} \times N_{\text{dof}}}{\sum_n (\sigma_n / a_n^*)^2}, \tag{3.25}$$

where p is the unconstrained p-value, N_{dof} is the number of degrees of freedom in the fit and (σ_i / a_i^*) is the relative error in the nth fit parameter. The form of Q is motivated by old techniques in the QCD literature [30]. Although this criterion is ultimately arbitrary, it coincides with intuition about which fits ought to be considered good and removes subjective bias. It is worthwhile to note that, although this function involves the p-value used in statistical hypothesis testing, we are not interested in its statistical properties, *per se*. Instead, Q should simply be seen as number which has been engineered to be large for "good" fits and small for "bad" fits.

For each fit, the final procedure is as follows. First, we vary the initial and final times $[t_{\min}, t_{\max}]$ used in the fits, amounting to a grid search over possible range fits. Next, we choose the best fit to be the one with maximum value of Q. We confirm that masses emerging from this procedure are consistent with expectations from effective mass plots. Finally, for an estimate of the systematic uncertainty associated with the fit-choice procedure, we compute the spread in the model parameters emerging from all nominally good fits, e.g., those with $Q \geq 0.1$ or $\chi^2/\text{dof} \sim 1$. We then combine statistical and systematic uncertainties conservatively using

$$\sigma_{\text{tot}} = \sigma_{\text{stat}} + \sigma_{\text{syst}}. \tag{3.26}$$

The systematic error assigned by this procedure can be comparable to the statistical error and is occasionally significantly larger.

Chapter 4

Simulation Details

After the extended motivation of the preceding chapters, we are now in a position to discuss the lattice simulations which are the heart of this thesis.

This thesis presents a lattice study of SU(4) gauge theory with two flavors of Dirac fermions ($N_f = 2$) in each of two distinct representations, the fundamental **4** and two-index antisymmetric **6** (a real representation). The motivation for this study is a composite Higgs model proposed by Ferretti and introduced in Sec. 1.3.1 above. We remind the reader that Ferretti's model contains five Majorana fermions in the sextet representation and three Dirac fermions in the fundamental. Simulating this fermion content requires the costly rational hybrid Monte Carlo algorithm. Instead, we study a deformed theory with four Majorana fermions (equivalent to two Dirac fermions) in the sextet and two Dirac fermions in the fundamental. As explained below, the model contains the essential qualitative physics of Ferretti's model while offering a laboratory for developing quantitative techniques.

The results in this and subsequent chapters are based on two papers from me and my colleagues [10, 13]. Although I led the analysis in these papers, the plural "we" reflects the collaborative nature of the work.

4.1 The Lattice Action and Parameters

Our lattice action contains gauge-field terms and two fermion actions, one for each representation:

$$S = S_{\text{gauge}} + S_F^{(\mathbf{4})} + S_F^{(\mathbf{6})}. \tag{4.1}$$

Each fermion action is a Wilson–clover action built of gauge links constructed by nHYP smearing [92, 91]. In $S_F^{(\mathbf{6})}$ the smeared links are promoted to the sextet representation [62]. There are two hopping parameters, κ_4 and κ_6. We set both clover coefficients equal to unity, $c_{\text{SW}} = 1$, a choice known to work well with nHYP smearing in QCD [25] and with fermions in higher representations [130].

The gauge-field action takes the form

$$S_{\text{gauge}} = \beta S_{\text{plaq}} + \gamma S_{\text{NDS}}. \tag{4.2}$$

The first term is the usual plaquette action, while the second is an nHYP dislocation-suppression (NDS) term [65], constructed from the nHYP-smeared links. The NDS term is designed to avoid singularities in the nHYP smearing. For the present study, we hold the ratio γ/β fixed at $1/125$ and use β as a free bare parameter.

Alongside the spectroscopic work described in this thesis, my colleagues and I are also studying the finite-temperature phase structure of the theory, also with the NDS action [12]. Comparing results of the sextet-only limit of this theory (in which the fundamental fermions are taken to be very heavy and decouple) to earlier published results [62] shows that the NDS action removes the previously-observed bulk transition from the interesting region of parameter space (see also Ref. [94]). In the multirep theory, we see no evidence for a bulk transition anywhere near the range of bare parameters at which we run, indicating that all of our ensembles correspond to the confined continuum phase with broken chiral symmetry.

4.2 Global Symmetries

In Ferretti's model, the massless sextet Majorana fermions $\psi^{(\mathbf{6})}$ condense and break their global flavor symmetry according to SU(5) $\to$ SO(5); the sextet Goldstone coset contains the Higgs multiplet of the Standard Model. In contrast, the symmetry breaking in the present simulations is SU(4) $\to$ SO(4). As discussed in Sec. 1.2.1, the pattern SU(N) $\to$ SO(N) arises because the sextet representation is real. A more detailed explanation is given in [62, 60]. The fundamental fermions $\psi^{(\mathbf{4})}$ in Ferretti's model condense in the chiral limit and break their chiral symmetry according to $\mathrm{SU}(3)_L \times \mathrm{SU}(3)_R \to \mathrm{SU}(3)_V$. In the present simulations, the corresponding symmetry-breaking scheme is $\mathrm{SU}(2)_L \times \mathrm{SU}(2)_R \to \mathrm{SU}(2)_V$, the familiar pattern from two-flavor QCD.

As usual, the Wilson term in the lattice action explicitly breaks the chiral symmetry of the theory. The lattice theory therefore possesses the same flavor symmetry as the (expected) broken phase of the continuum theory: $\mathrm{SU}(2)_V \times \mathrm{U}(1)_B$ for the fundamental representation and SO(4) for the sextet. In other words, using Wilson fermions assumes that global symmetries break according to the patterns of Sec. 1.2.1—those induced by fermion bilinear condensates.

Ferretti's model required fermions in multiple representations in order to build the composite baryon operators $B \sim \psi^{(\mathbf{4})}\psi^{(\mathbf{4})}\psi^{(\mathbf{6})}$. These fermionic operators couple to the "chimera" bound states which serve as partners for the top quark. Such chimera baryons still exist in the present theory and are discussed in Chapter 6.

A special feature of the two-representation theory is the existence of a conserved U(1) axial current. While the individual U(1) currents $J_{5\mu}^{(\mathbf{4})}$ and $J_{5\mu}^{(\mathbf{6})}$ are anomalous, one can form a linear combination $J_{5\mu}$ of these currents that decouples from $\epsilon^{\mu\nu\rho\sigma}F_{\mu\nu}F_{\rho\sigma}$. Condensation of either fermion species then spontaneously breaks the non-anomalous axial symmetry, giving rise to a flavor-singlet Goldstone boson that we denote ζ. The normalization of the U(1) current is reviewed in Ref. [10].

4.3 Setting the Scale

We set the scale in our simulations using the flow scale, t_0, introduced by Lüscher [115]. The flow scale is defined by the implicit equation

$$t^2\langle E(t)\rangle|_{t_0} = C, \tag{4.3}$$

where $E(t) = \frac{1}{4}G^a_{\mu\nu}G^a_{\mu\nu}(t)$ is constructed from the clover form of the field strength $G^a_{\mu\nu}$ at flow time t. Here C is a dimensionless number, conventionally [115] taken to be 0.3 in QCD. With this choice, $\sqrt{t_0}$ corresponds to a length scale of 0.14 fm (i.e., an energy scale of 1.4 GeV) in QCD simulations [20, 58].

For an arbitrary gauge theory, any value for C is *a priori* as good as any other. However, for comparison to existing studies with different gauge groups, it is useful to let C vary with N_c. Arguments from large-N_c QCD, supported by lattice data [40, 58], suggest that $t_0 \sim N_c$ at leading order. For the SU(4) simulations of this work we therefore use

$$t^2\langle E(t)\rangle|_{t_0} = 0.3 \times \frac{4}{3} = 0.4\,. \tag{4.4}$$

Lattice calculations give masses as dimensionless numbers Ma and the gradient-flow scale as t_0/a^2. Dimensionless products like $\hat{M} \equiv M\sqrt{t_0}$ eliminate the lattice spacing a, and our tables and figures will display such quantities. To aid intuition with respect to QCD, one can mentally convert $M\sqrt{t_0}$ to $M/(1.4\text{ GeV})$.

We return to the subject of scale-setting and its connection to chiral perturbation theory in Section 5.1 below.

4.4 Computing the Spectrum

We extract masses and decay constants in the usual way from two-point correlation functions as described in Sec. 3.3 For mesons, we denote pseudoscalar masses and decay constants as M_P and F_P, respectively. The corresponding quantities in the vector channel are denoted by M_V and

F_V. For baryons, a generic mass will be M_B. In all cases, additional subscripts indicate the representation: **4**, **6**, or mixed. For instance, M_{P4} is a fundamental pseudoscalar meson.

We define the fermion masses m_4 and m_6 by imposing the axial Ward identity (AWI),

$$\partial_\mu \langle 0|A^{(r)}_{\mu a}(x)\mathcal{O}_r(0)|0\rangle = 2m_r \langle 0|P^{(r)}_a(x)\mathcal{O}_r(0)|0\rangle \ , \tag{4.5}$$

where $x \neq 0$, and a is an isospin index. We use the local unimproved axial current $A^{(r)}_{\mu a}$ and pseudoscalar density $P^{(r)}_a$ in each representation r. For the determination of the AWI mass, we do not renormalize these currents because the mass itself is not a physical observable; based on the perturbative renormalization of these currents described in Ref. [10], the effect of including the renormalization would be small anyway, amounting to a few-percent shift of the masses. For $\mathcal{O}_r$ we take a pseudoscalar source. When the distinction between representations is irrelevant, we will refer to the fermion mass defined by Eq. (4.5) as $m_{\rm AWI}$.

The pseudoscalar decay constants are defined by

$$\left\langle 0\middle|A^{(r)}_{4a}\middle|P^{(r)}_b\right\rangle = \delta_{ab} M_{Pr} F_{Pr} \ , \tag{4.6}$$

at zero spatial momentum, which is the convention that gives $F_\pi \simeq 130$ MeV in QCD. We calculate F_{Pr} with the procedure described in Sec. 3.3. Renormalization is described in Ref. [10].

4.5 Ensembles

The ensembles used in this study are listed in Tables D.1–D.3 in Appendix D. They fall into three groups. The short runs with the smallest lattices, of size $V = N_s^3 \times N_t = 16^3 \times 18$, were used for general orientation in the three-dimensional coupling space $(\beta, \kappa_4, \kappa_6)$. The most important observables for this step were the gradient-flow scale $\sqrt{t0}$ (see Tables D.4–D.6), and the masses M_{Pr} of the pseudoscalars constructed respectively from fermions in the $r = \mathbf{4}$ and $\mathbf{6}$ representations (see Tables D.7–D.9).

The goal of this orientation was to find couplings that give $t_0/a^2 = O(1)$ along with pseudoscalar masses that are reasonably light, for subsequent comparison to χPT. It turned out that

these short runs yielded results that are in themselves usable in the chiral fits to be presented below, and hence we include them in our analysis.

As can be seen in the tables, some ensembles differ in small changes to their κ_r values. Our orientation runs found that t_0/a^2 and aM_P are often sensitive to these small changes.

We demanded that our ensembles satisfy the criterion $M_{Pr}L > 4$ for both representations, where $L = N_s a$ is the spatial size of the lattice. This is the familiar rule of thumb from QCD, based on the fact that leading-order finite-volume corrections are proportional to $e^{-M_\pi L}$; a more detailed study of finite-volume effects in our data is given in Ref. [10]. We considered cutting data above a maximum value of t_0/a^2 beyond which finite-volume effects severely contaminate determination of the flow scale; such a cut was found to be unnecessary following the cuts on $M_P L$. We did eliminate ensembles with $t_0/a^2 < 0.94$ because in these cases the flow did not enter a linear regime. These correspond to a large lattice spacing—in QCD language, $1/a < 1.3$ GeV.

Having found interesting regions for study, we continued with high-statistics runs on lattices with $V = 16^3 \times 32$. Finally, we have four extended runs on lattices with $V = 24^3 \times 48$. These runs were done at large t_0/a^2 and small $\hat{M}_P$, so that the constraint $M_P L > 4$ demanded an increase in L/a.

The pseudoscalar masses for all the ensembles are given in Tables D.7–D.9. To show our coverage of M_P values, we map them in the (M_{P4}, M_{P6}) plane in Figs. 4.1 and 4.2. The first shows the pseudoscalar masses obtained for $0.94 < \sqrt{t_0}/a < 1.41$, which translates to a cutoff of 1.3 GeV $< 1/a <$ 2 GeV in QCD language (most are in the neighborhood of $\sqrt{t_0}/a = 1.05$, or $1/a = 1.45$ GeV). The second plot represents ensembles in the range $1.41 < \sqrt{t_0}/a < 1.64$, or 2 GeV $< 1/a <$ 2.3 GeV.

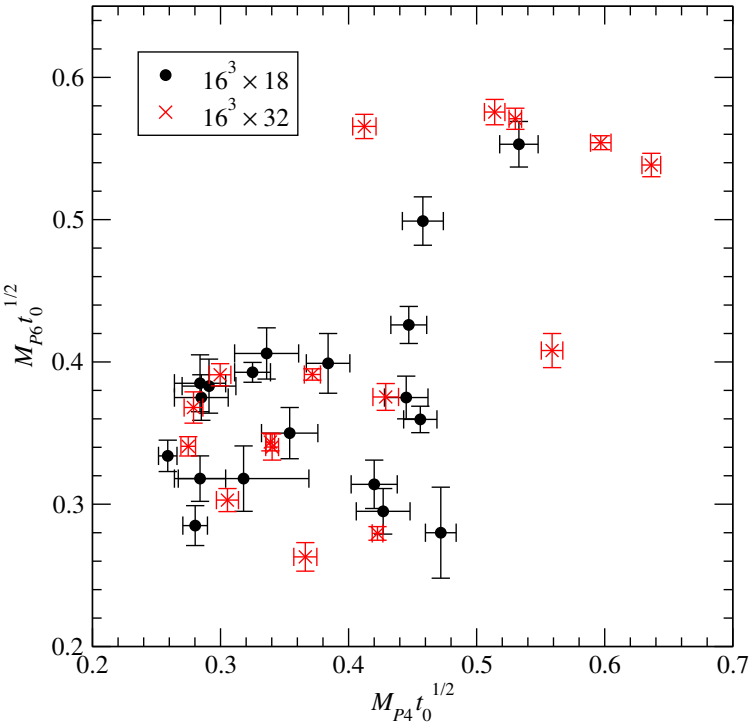

Figure 4.1: Map of our ensembles in the plane of pseudoscalar masses M_{Pr}. These are coarse lattices, with $0.94 < \sqrt{t_0}/a < 1.41$. We define arbitrarily $\sqrt{t_0} = (1.4 \text{ GeV})^{-1}$ for comparison with QCD. For most of these ensembles $1/a \simeq 1.45$ GeV by this measure.

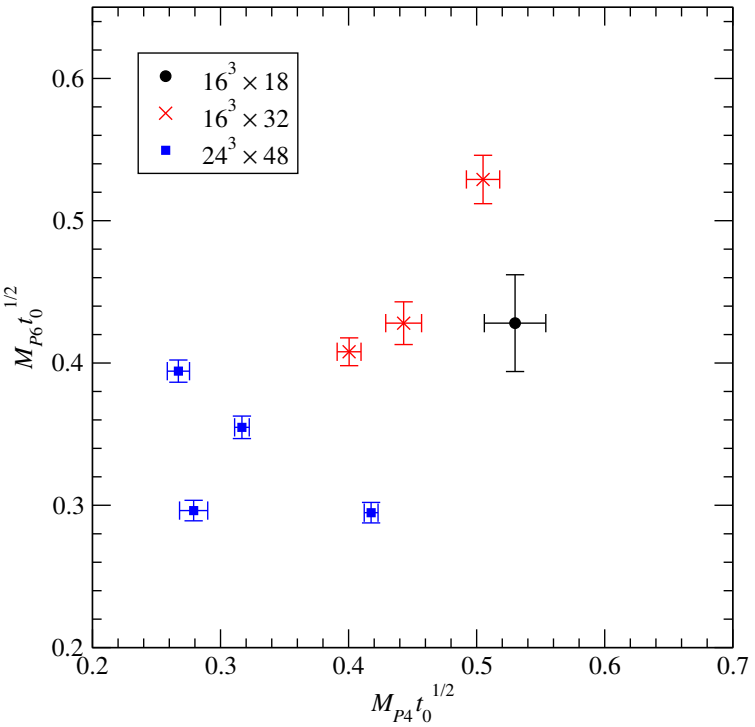

Figure 4.2: Same as Fig. 4.1, but here we plot ensembles on fine lattices, $\sqrt{t_0}/a > 1.41$. If we fix $\sqrt{t_0} = (1.4 \text{ GeV})^{-1}$ then this means $1/a > 2$ GeV. The blue squares are all at $1/a \simeq 2.1$ GeV.

Chapter 5

The Meson Spectrum

In this chapter we discuss the meson spectrum in our theory. Sec. 5.1 begins with a discussion of the low-energy EFT and its role in defining a mass-dependent scheme for setting the physical scale of the simulations. Next, Sec. 5.2 presents results for the pseudoscalar masses and decay constants and conducts a joint extrapolation to the chiral and continuum limits using the EFT. Finally, Sec. 5.3 presents results for the vector masses and decay constants, interpreting the findings in terms of a model using vector meson dominance.

5.1 Chiral Perturbation Theory

The standard framework for analyzing the light pseudoscalar sector is chiral perturbation theory (χPT). The generalization of χPT to a theory with fermions in two different representations was developed in Ref. [60], and the next-to-leading-order (NLO) results of this work provide the basis for our fits for the pseudoscalar masses and decay constants. We will also need Wilson chiral perturbation theory (WχPT), the extension of chiral perturbation theory to include the discretization errors of Wilson fermions [133, 17, 128, 5, 132, 86].

5.1.1 Chiral Perturbation Theory and Setting the Scale

In this work we use the gradient-flow scale $\sqrt{t_0}$ as the characteristic length scale of every ensemble. This choice allows us to measure dimensionful quantities as the fermion masses vary. To measure an observable in units of t_0 simply means to multiply it by the power of t_0 that renders

it dimensionless. Since t_0 itself admits a chiral expansion [16], the resulting dimensionless quantity admits a chiral expansion whenever the original dimensionful observable does.

To see how this idea works in practice, consider a gauge theory with mass-degenerate fermions of mass m in the same representation. In continuum χPT, the leading-order (LO) pseudoscalar mass is

$$(M^2)^{\mathrm{LO}} = 2Bm, \tag{5.1}$$

where B and F are the familiar parameters of the leading-order chiral Lagrangian. The the next-to-leading (NLO) expression for the decay constant is

$$F^{\mathrm{NLO}} = F\left(1 + c\,\frac{2Bm}{8\pi^2F^2}\log\left(2Bm/\mu^2\right) + L\,\frac{2Bm}{F^2}\right). \tag{5.2}$$

The remaining parameters in Eq. (5.2) are the renormalization scale (μ) and L, which is a dimensionless linear combination of the NLO low-energy constants (LECs). The value of L depends on the choice of the renormalization scale. The coefficient c of the logarithmic term is a calculable number that depends only on the fermion representation and on the number of flavors [29].

The NLO result for flow scale t_0 is

$$t_0^{\mathrm{NLO}} = t_{0,\mathrm{ch}}\left(1 + k_1\frac{2Bm}{F^2}\right)\ , \tag{5.3}$$

where $t_{0,\mathrm{ch}}$ is the value of t_0 in the chiral limit, and k_1 is a new LEC. Notice that this expression depends analytically on the fermion mass m. As was shown in Ref. [16], logarithmic corrections to t_0 occur for the first time at the next-to-next-to-leading order ($\mathrm{N^2LO}$).

Combining Eqs. (5.2) and (5.3) we obtain the NLO result for the dimensionless product $\hat{F} \equiv F\sqrt{t_0}$,

$$\hat{F}^{\mathrm{NLO}} = F\sqrt{t_{0,\mathrm{ch}}}\left(1 + c\,\frac{2Bm}{8\pi^2F^2}\log\left(2Bmt_0\right) + (L + k_1/2)\frac{2Bm}{F^2}\right)\ . \tag{5.4}$$

Here we have chosen the renormalization scale to be $\mu = t_{0,\mathrm{ch}}^{-1/2}$. The low-energy constants are independent of the fermion mass, and to preserve this feature we rescale them with $t_{0,\mathrm{ch}}$, for

example defining $\mathring{F} = F\sqrt{t_{0,\mathrm{ch}}}$. Equation (5.4) can then be written as

$$\hat{F}^{\mathrm{NLO}} = \mathring{F}\left(1 + c\,\frac{2\mathring{B}\mathring{m}}{8\pi^2\mathring{F}^2}\log\left(2\mathring{B}\mathring{m}\right) + (L + k_1/2)\frac{2\mathring{B}\mathring{m}}{\mathring{F}^2}\right) \ . \tag{5.5}$$

The expansion parameter is now $\mathring{m}$, which is the fermion mass m measured in units of $t_{0,\mathrm{ch}}$.

Equation (5.5) is inconvenient because $\mathring{m}$ is not known for a given ensemble until $t_{0,\mathrm{ch}}$ is known. Finding $t_{0,\mathrm{ch}}$ (in units of t_0 of the given ensemble) requires a complicated fitting procedure that we wish to avoid. Instead, we opt for rescaling all observables of a given ensemble, including the fermion mass, with t_0 of the same ensemble. Introducing $\hat{m} \equiv m\sqrt{t_0}$ we now use Eq. (5.3) to relate the rescaled masses,

$$\mathring{m} = \hat{m}\left(1 - k_1\frac{Bm}{F^2}\right) \ , \tag{5.6}$$

which allows us rewrite Eq. (5.5) as

$$\hat{F}^{\mathrm{NLO}} = \mathring{F}\left(1 + c\,\frac{2\mathring{B}\hat{m}}{8\pi^2\mathring{F}^2}\log\left(2\mathring{B}\hat{m}\right) + (L + k_1/2)\frac{2\mathring{B}\hat{m}}{\mathring{F}^2}\right) \ . \tag{5.7}$$

The transition from $\mathring{m}$ to $\hat{m}$ left no trace, because the difference is a higher-order correction. More generally, at NLO the transition from $\mathring{m}$ to $\hat{m}$ can always be absorbed into a redefinition of the low-energy constants. This redefinition is non-trivial, for instance, in the case of the NLO pseudoscalar mass.

An appealing feature of Eq. (5.7) is that it looks the same as Eq. (5.2). In particular, the coefficient of the logarithmic term is unchanged. The only minor change is that the coefficient of the NLO analytic term is now $L + k_1/2$ instead of L. It can be checked that this nice feature generalizes to an arbitrary fermion content. At N^{2}LO things would become technically more complicated, because N^{2}LO logarithmic corrections for t_0 would have to be incorporated as well. In the NLO fit formulae below, all the logarithmic terms will thus have the same coefficients as in the usual continuum NLO expressions [29, 60].

5.1.2 Wilson Chiral Perturbation Theory

The extension of continuum chiral perturbation theory to include the discretization errors of Wilson fermions goes under the name of Wilson chiral perturbation theory, or WχPT. In the light pseudoscalar sector, WχPT allows us to extrapolate both to the chiral ($m \to 0$) and continuum ($a \to 0$) limits. WχPT comes in two variants, depending on the choice of a power counting scheme. In this analysis we follow the "generic small mass" power counting, defined by

$$p^2 \sim m \sim a \ , \tag{5.8}$$

where p is an external momentum, m is the fermion mass, and a is the lattice spacing, all measured in terms of a typical hadronic scale. The alternative power counting scheme, known as the "large cutoff effects" power counting, is defined by

$$p^2 \sim m \sim a^2 \ . \tag{5.9}$$

The generic small mass scheme is appropriate when the fermion mass is not too small, and $O(a^2)$ effects may be considered as subleading corrections. Both schemes require that simulations remain within the chiral regime, where $\hat{m} = m\sqrt{t_0}$ is small.

The fermion mass appearing in the leading-order Lagrangian of WχPT is the so-called *shifted mass*, defined by

$$m_{\text{shifted}} = m_{\text{ctm}} + aW_0/B, \tag{5.10}$$

where m_{ctm} is the fermion mass of continuum χPT, and W_0 is a new low-energy constant from WχPT. The difference between the shifted and continuum masses vanishes in the continuum limit.

For the present analysis, we need to know how the shifted mass m_{shifted} compares to the fermion mass m_{AWI} measured in our simulations via the axial Ward identity Eq. (4.5). As was shown in Ref. [6], $m_{\text{shifted}} = m_{\text{AWI}}$, up to corrections that are higher order in either of the above power counting schemes. A derivation of of this result is summarized in Ref. [10]. For our chiral fits we thus define

$$\hat{m} = m_{\text{AWI}}\sqrt{t_0} \ . \tag{5.11}$$

The last ingredient we need for our fits is the lattice spacing. Since we are measuring all dimensionful quantities in units of t_0, it is natural to adopt a *mass-dependent* prescription, and to measure also the lattice spacing in units of t_0. We thus introduce

$$\hat{a} \equiv a/\sqrt{t_0} \ . \tag{5.12}$$

The Wilson discretization effects of any hatted (dimensionless) observable will be accounted for by an expansion in $\hat{a}$.

In QCD studies, it is common to choose a *mass-independent* scale-setting prescription in which the lattice spacing is a function of the bare coupling β but is independent of the bare fermion masses (see for example Refs. [19, 33]). In brief, for every constant-β plane, this procedure requires finding the point where certain dimensionless quantities (such as M_π/F_π and M_K/F_K) attain their real-world values. The value in lattice units of some dimensionful observable at the reference point is then used to determine the lattice spacing in physical units.

Here we have opted for mass-dependent scale setting because of several important differences. First, the BSM context does not provide us with any experimental results that could be used to define a reference point. This problem might be circumvented by invoking the chiral limit as a reference point on each constant-β plane. Using this limit, however, has the undesirable feature that the scale setting procedure would necessarily involve an extrapolation.

Second, in our model, as in many other models that have been studied in the BSM context, we observe a rapid change of t_0/a^2 with the fermion mass, especially when the latter becomes light. Moreover, this phenomenon is quite general and is seen for virtually any quantity that might be used to set the scale; its proper interpretation is that the lattice spacing itself is changing rapidly. The underlying reason for this phenomenon is that, in comparison with QCD, BSM theories tend to have a large number of fermionic degrees of freedom, which have a strong screening effect on the bare coupling. When we consider the dependence of a hatted quantity, such as $\hat{M}_P$, on the hatted mass parameter, $\hat{m}$, we expect to see some deviations from the continuum values, but such scaling violations should be small when the bare coupling is small enough. By contrast, as explained above,

the lattice spacing $\hat{a}$ itself can vary rapidly with the fermion mass(es). By using the mass-dependent scale-setting prescription of Eq. (5.12) we can incorporate this effect into our analysis. As we will see, the remaining scaling violations in the hatted quantities are small and amenable to WχPT.

5.1.3 Summary of Formulae from Chiral Perturbation Theory

Our central fits below will include terms through NLO in the generic small mass power counting. These formulae depend exclusively on the dimensionless quantities we have introduced in the previous subsections. The NLO expressions for the pseudoscalar masses of the two representations are

$$(\hat{M}_{P4}^2)^{\rm NLO} = 2\hat{m}_4\mathring{B}_4\left(1 + L_{44}^M\hat{m}_4 + L_{46}^M\hat{m}_6 + \frac{1}{2}\Delta_4 - \frac{4}{5}\Delta_\zeta\right) + \mathring{W}_{44}^M\hat{a}\hat{m}_4 + \mathring{W}_{46}^M\hat{a}\hat{m}_6 + \mathring{W}_4^M\hat{a}^2 \ , \tag{5.13}$$

$$(\hat{M}_{P6}^2)^{\rm NLO} = 2\hat{m}_6\mathring{B}_6\left(1 + L_{66}^M\hat{m}_6 + L_{64}^M\hat{m}_4 - \frac{1}{4}\Delta_6 - \frac{1}{5}\Delta_\zeta\right) + \mathring{W}_{66}^M\hat{a}\hat{m}_6 + \mathring{W}_{64}^M\hat{a}\hat{m}_4 + \mathring{W}_6^M\hat{a}^2 \ , \tag{5.14}$$

while the expressions for the decay constants are

$$(\mathring{F}_{P4})^{\rm NLO} = \mathring{F}_4\left(1 + L_{44}^F\hat{m}_4 + L_{46}^F\hat{m}_6 - \Delta_4\right) + \mathring{W}_4^F\hat{a} \ , \tag{5.15}$$

$$(\mathring{F}_{P6})^{\rm NLO} = \mathring{F}_6\left(1 + L_{66}^F\hat{m}_6 + L_{64}^F\hat{m}_4 - 2\Delta_6\right) + \mathring{W}_6^F\hat{a} \ . \tag{5.16}$$

The one-loop chiral logarithms enter as

$$\Delta_4 = \frac{2\hat{m}_4\mathring{B}_4}{8\pi^2\mathring{F}_4^2}\log\left(2\hat{m}_4\mathring{B}_4\right) \ , \tag{5.17}$$

$$\Delta_6 = \frac{2\hat{m}_6\mathring{B}_6}{8\pi^2\mathring{F}_6^2}\log\left(2\hat{m}_6\mathring{B}_6\right) \ ,$$

$$\Delta_\zeta = \frac{\hat{M}_\zeta^2}{8\pi^2\mathring{F}_\zeta^2}\log\left(\hat{M}_\zeta^2\right) \ ,$$

where the dimensionless mass-squared of the flavor singlet Goldstone boson is *defined* by

$$\hat{M}_\zeta^2 = \frac{8}{5}\left(\frac{2\mathring{F}_4^2\hat{m}_4\mathring{B}_4 + \mathring{F}_6^2\hat{m}_6\mathring{B}_6}{\mathring{F}_\zeta^2}\right) \ . \tag{5.18}$$

This corresponds to the LO result of Ref. [60], rescaled by t_0. Further technical details related to the ζ and conventions for the conserved axial current appear in Ref. [10].

The most important parameters in the expressions above are the LO low-energy constants of the continuum two-representation theory (rescaled by $\sqrt{t_{0,\mathrm{ch}}}$): $\mathring{B}_4$, $\mathring{B}_6$, $\mathring{F}_4$, $\mathring{F}_6$, and $\mathring{F}_\zeta$. The dimensionless parameters L_{rs}^M and L_{rs}^F, $r = 4, 6$, are linear combinations of the continuum NLO low-energy constants and of similar NLO low-energy constants originating from the chiral expansion of the flow scale [cf. Eq. (5.3)]. The general form of the analytic NLO continuum terms was discussed in [60]. Because we do not have enough independent quantities to distinguish the individual NLO low-energy constants, we instead consider L_{rs}^M and L_{rs}^F as the parameters for the fit. Finally, the various $\mathring{W}$ parameters account for the NLO analytic terms of WχPT in the generic small mass power-counting scheme. Overall, these formulae contain 21 undetermined parameters, which we will fit below using 172 correlated points of data: four data points for each of our 43 ensembles.

We have not presented NLO fit formulae for the mass and decay constant of the singlet Goldstone boson ζ. We do not make use of these formulae in this work because we have not calculated fermion-disconnected diagrams, which is technically challenging, and so we do not have direct access to the singlet sector. Nevertheless, through the quantity Δ_ζ, virtual ζ loops contribute to the masses and decay constants of the other Goldstone bosons at NLO. In the next section we will explore what can be learned about the singlet sector from this effect.

Another interesting quantity is the chiral condensate in each representation. At lowest order in χPT (equivalently, in the corresponding chiral limit, $\hat{m}_r \to 0$), the fermion condensate per flavor is given by

$$\hat{\Sigma}_r = -\mathring{B}_r \mathring{F}_r^2 \ . \tag{5.19}$$

Instead of measuring the condensates directly—a formidable task with Wilson fermions—we will make use of Eq. (5.19) to extract their values in the joint chiral limit from our analysis of the pseudoscalar masses and decay constants.

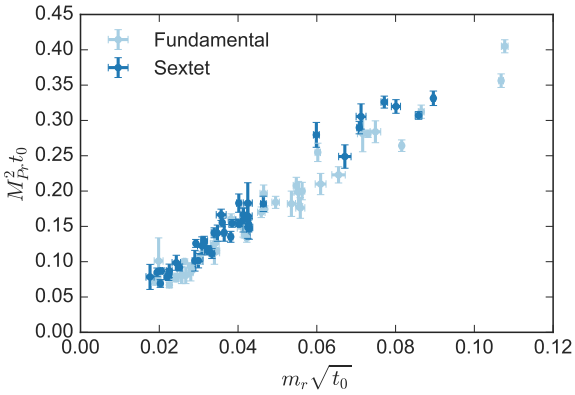

Figure 5.1: Squared mass of the two pseudoscalar species, each plotted against the AWI mass of the corresponding fermion species, all in units of the flow scale t_0.

5.2 Pseudoscalar mesons

5.2.1 Masses and Decay Constants

We begin with the pseudoscalar mesons, which become Goldstone bosons in the chiral limit. For a first look, we plot in Fig. 5.1 the squared masses $\hat{M}_{Pr}^2$. The sextet mass $\hat{M}_{P6}$ is plotted against sextet fermion mass $\hat{m}_6$, ignoring the dependence on the fundamental fermion mass $\hat{m}_4$. Likewise for the fundamentals, $\hat{M}_{P4}$ is plotted against $\hat{m}_4$. As expected from leading-order chiral perturbation theory, the overall behavior of each squared mass is approximately linear. One supposes that the scatter around the straight lines is due to the hidden dependence on the other fermion mass, as well as corrections from NLO and from lattice artifacts. We will examine this hypothesis shortly.

We plot the (rescaled) decay constants $\hat{F}_{Pr}$ in Fig. 5.2. The data show a steady rise with $\hat{m}_r$. The same qualitative behavior is seen in QCD, where the pion decay constant is an increasing function of the quark mass.

Sec. 5.1.3 presents the predictions of χPT in NLO for pseudoscalar observables. We conduct a joint fit of the four observables $\hat{M}_{Pr}^2$ and $\hat{F}_{Pr}$ to the NLO formulae of Eqs. (5.13)–(5.16). On each ensemble, we use single-elimination jackknife to construct the 6×6 correlation matrix among pseudoscalar masses, decay constants, and AWI masses of the fermions. These correlation matrices

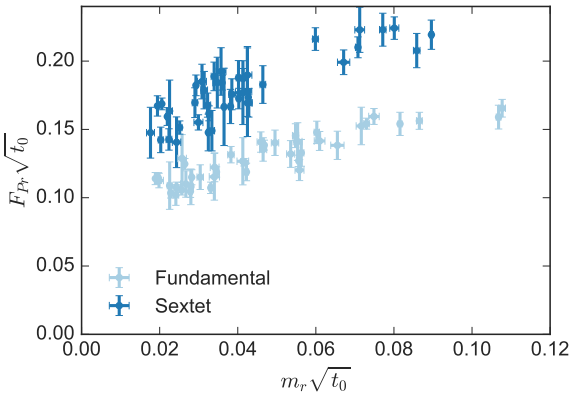

Figure 5.2: Decay constant of each pseudoscalar species plotted against the mass of the corresponding fermion species, in units of the flow scale t_0.

enter into the χ^2 function that is minimized for the fit. We do not include correlations with the flow scale t_0, which has negligible error compared to the other quantities we extract.

The full NLO fit to 21 parameters and $172 - 21 = 151$ degrees of freedom gives $\chi^2/\text{dof} = 0.48$. Table 5.1 contains the resulting values for the low-energy constants and demonstrates the presence of important lattice artifacts in our data. For the masses, the most significant terms are the $\mathcal{O}(\hat{m}_r\hat{a})$ artifacts, in the same representation. For the decay constants, the $\mathcal{O}(\hat{a})$ artifacts are also significant. From an empirical perspective, these four NLO Wilson terms form a necessary minimal set of artifact terms for modeling the data.

Figures 5.3 and 5.4 illustrate the sizes of the Wilson artifacts (red) emerging from this fit. In these figures, the "corrected" data (dark blue) result from subtracting the lattice artifacts from the data (light blue), allowing us to extrapolate to the continuum limit, $\hat{a} \to 0$. The corrected data follow fairly well the tree-level formula for the pseudoscalar masses and the continuum NLO result for the decay constants, respectively, both indicated by green bands. The bands represent one standard deviation (1σ) in the fit parameters.

In order to display a smooth curve for the continuum NLO result for the decay constants, we have included only the same-representation terms when drawing the green band (indicated by "continuum NLO SREP" in the figure). The remaining scatter and deviation in the subtracted

LO:	$\mathring{B}_4$	2.4(2)
	$\mathring{B}_6$	2.7(1)
	$\mathring{F}_4$	0.114(7)
	$\mathring{F}_6$	0.17(1)
	$\mathring{F}_\zeta$	0.16(2)
continuum NLO:	L_{44}^F	3.4(5)
	L_{46}^F	1.4(6)
	L_{64}^F	0.3(4)
	L_{66}^F	3.9(5)
	L_{44}^M	0.1(7)
	L_{46}^M	3.(1)
	L_{64}^M	0.4(7)
	L_{66}^M	0.5(7)
lattice NLO:	$\mathring{W}_4^F$	-0.055(6)
	$\mathring{W}_6^F$	-0.08(1)
	$\mathring{W}_4^M$	0.01(1)
	$\mathring{W}_{44}^M$	-1.9(3)
	$\mathring{W}_{46}^M$	-0.6(3)
	$\mathring{W}_6^M$	0.001(9)
	$\mathring{W}_{64}^M$	0.1(2)
	$\mathring{W}_{66}^M$	-2.5(4)

Table 5.1: Parameter values from a joint fit to the full NLO χPT formulae.

data (dark blue) is evidence of coupling between the representations.

Table 5.1 demonstrates that all five LO low-energy constants are well-determined by the NLO fit. We note that the singlet decay constant $\mathring{F}_\zeta$ is larger than $\mathring{F}_4$ and similar in size to $\mathring{F}_6$. Because measurement of chiral logarithms is known to be a difficult task in QCD studies, we return to the question of the stability of this result below.

Turning our attention to the NLO low-energy constants, we examine the communication between the representations. The ratios L_{46}^M/L_{44}^M and L_{46}^F/L_{44}^F quantify the relative influence of the sextet fermions on $\hat{M}_{P4}^2$ and $\hat{F}_{P4}$, respectively, in the continuum theory. Similarly, the ratio $\mathring{W}_{46}^M/\mathring{W}_{44}^M$ measures the relative influence of the sextet artifact term compared to the fundamental artifact term in $\hat{M}_{P4}^2$. Taking into account correlations, the following ratios are different from zero

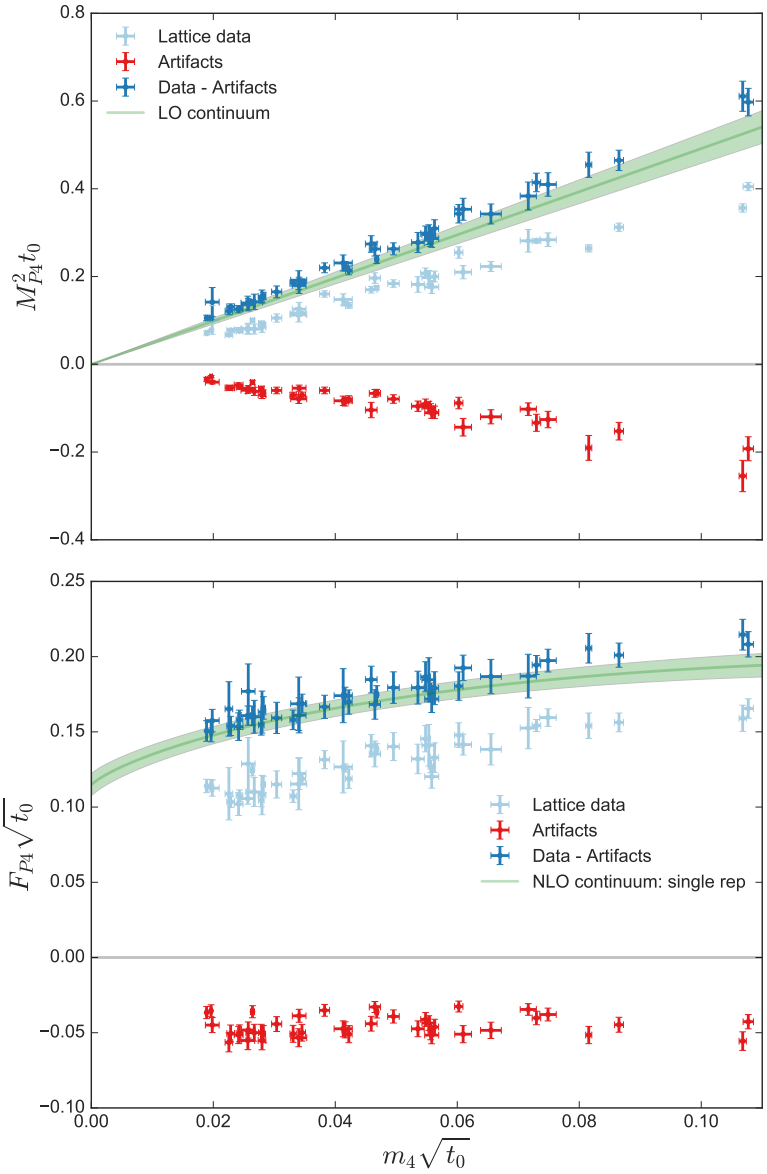

Figure 5.3: Breakdown of the contribution of lattice artifacts in the joint fit to χPT for the fundamental masses and decay constants.

at the 2σ level,

$$L_{46}^F / L_{44}^F = +0.4(2), \tag{5.20}$$

$$\mathring{W}_{46}^M / \mathring{W}_{44}^M = +0.30(15). \tag{5.21}$$

The converse influence of the fundamentals upon the sextets follows from exchanging $(4 \leftrightharpoons 6)$. The

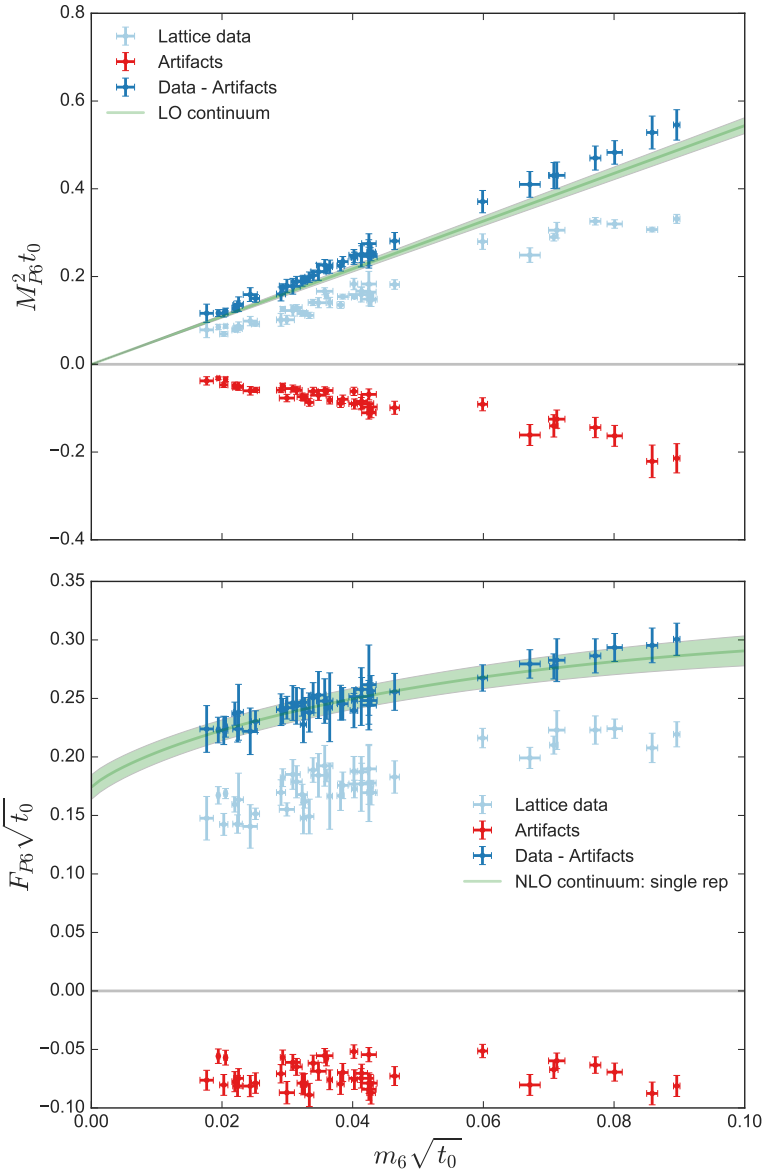

Figure 5.4: Breakdown of the contribution of lattice artifacts in the joint fit to χPT for the sextet masses and decay constants.

ratios L_{64}^M/L_{66}^M, L_{64}^F/L_{66}^F, and $\mathring{W}_{64}^M/\mathring{W}_{66}^M$ are all consistent with zero. Despite the large uncertainties, these ratios suggest that the sextets influence the fundamentals significantly, while the converse is not true. The same qualitative conclusion is also evident, for instance, in the NLO continuum behavior of the decay constants. Figure 5.4 shows that subtracted data (dark blue) are, to good approximation, a smooth function of $\hat{m}_6$ only. In contrast, the corresponding fundamental result

in Fig. 5.3 (also in dark blue) exhibits a conspicuous jaggedness, indicating important dependence on the sextet fermion mass.

5.2.2 Stability of the NLO Fit

In this subsection we explore the stability of the NLO fit. First, since our analysis uses empirical priors to aid convergence of the non-linear fitting procedure, it is important to verify that they did not bias our results. To this end, we have redone the fit using the results of the first fit as initial guess, while multiplying the width of all priors by 10. Figure 5.5 shows the results of both fits for the 5 LO low-energy constants in the two lines at the bottom. The results are indistinguishable, indicating that the LO low-energy constants were not influenced by the priors. The same is also true for the NLO low-energy constants.

The chiral fit provides *a posteriori* justification for the use of generic small mass power counting, where $\mathcal{O}(a^2)$ terms are not part of the LO Lagrangian. Both fermion masses in our ensembles lie roughly in the range

$$0.02 \lesssim \hat{m}_r \lesssim 0.10 \ . \tag{5.22}$$

The range of lattice spacings we explore is

$$0.4 \lesssim \hat{a}^2 \lesssim 1.1 \ . \tag{5.23}$$

(Recall that Eq. (5.12) defines $\hat{a}^2 = a^2/t_0$ in our scale-setting procedure.) The $\mathcal{O}(m_r)$ contribution to the pseudoscalar masses is $2\mathring{B}_r\hat{m}_r$, while the $\mathcal{O}(a^2)$ contribution is $\mathring{W}_r^M\hat{a}^2$. For our fermion masses and lattice spacings, these contributions lie approximately within the following ranges

$$2\mathring{B}_r\hat{m}_r : \ 5 \times [0.02, 0.1] \approx [0.1, 0.5] \ , \tag{5.24}$$

$$\mathring{W}_r^M\hat{a}^2 : \ 0.01 \times [0.4, 1.1] \approx [0.004, 0.01] \ . \tag{5.25}$$

We see that the $\mathcal{O}(m_r)$ terms are at least an order of magnitude larger than the $\mathcal{O}(a^2)$ terms, showing that the generic small mass power counting is appropriate (as long as this picture is not upset by large N^{2}LO corrections, see below).

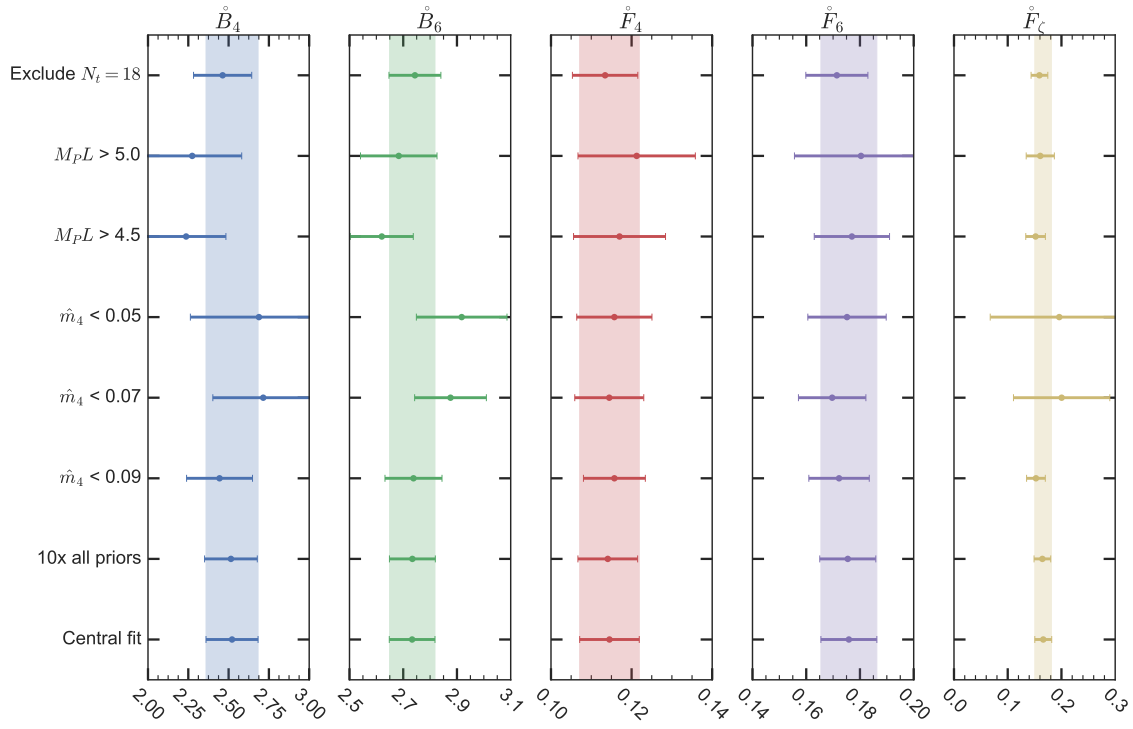

Figure 5.5: Exploring the stability of leading-order LECs in chiral fits. We take the NLO result to define our central values, which appear at the bottom of each column. The variations are described in the text.

Measurement of the LECs also provides information about the convergence of the chiral expansion. With our convention for the decay constant, the expansion parameters of continuum χPT are $\xi_r \equiv 2\mathring{B}_r \hat{m}_r / 8\pi^2 \mathring{F}_r^2$. With the central-fit values for the low-energy constants, these fermion masses correspond to the following ranges for the expansion parameters,

$$0.09 \lesssim \xi_4 \lesssim 0.50 \ , \tag{5.26}$$

$$0.04 \lesssim \xi_6 \lesssim 0.20 \ . \tag{5.27}$$

We see that the the maximum of the sextet expansion parameter ξ_6 is smaller by a factor of 2.5 than the fundamental expansion parameter ξ_4. The main reason is that $\mathring{F}_6$ is significantly larger than $\mathring{F}_4$, as might be expected based on the relative dimension of the two representations.

It is quite plausible that ξ_6 is sufficiently small that the expansion in m_6 converges well over

our entire ensemble set. The same may not be true for ξ_4, whose value can be as large as 0.5. In the next three lines of Fig. 5.5 we study the influence on the LO low-energy constants of dropping ensembles at the high end of the $\hat{m}_4$ range: $\hat{m}_4 > 0.09$, > 0.07, and finally > 0.05. We see that truncating our data set has only a modest effect on the $\mathring{F}_r$ and $\mathring{B}_r$ parameters. On the other hand, since we only obtain $\mathring{F}_\zeta$ through NLO logarithms, it is not surprising that the increase in the error of $\mathring{F}_\zeta$ is much more pronounced. Indeed, when we restrict to $\hat{m}_4 < 0.05$, $\mathring{F}_\zeta$ is only two standard deviations (2σ) away from zero.

The next two lines in Fig. 5.5 investigate the possible influence of finite-volume effects on our central analysis; a more thorough technical discussion appears in Ref. [10]. The minimum cutoff on $M_P L$ in data used in the central fit is varied from its initial value of 4.0 in our main analysis to 4.5 and 5.0, excluding more data than would be expected to have the largest finite-volume effect contamination. Finally, in the top line we repeat our fit with all $V = 16^3 \times 18$ ensembles excluded from the analysis, in order to test for systematic effects in our correlator analysis due to the smaller time extent. No significant change to our results appears in any case.

The main systematic uncertainty about this non-QCD system is the neglect of N^{2}LO corrections. We do not really know how high can we go in ξ_4 and ξ_6 if we want these corrections to remain below a certain level. While our stability tests give us some insight, we do not have enough data for a quantitative study of N^{2}LO. Nevertheless, we take the smallness of ξ_6 and our stability tests on $\hat{m}_4$ as evidence that the data are in the regime where NLO χPT applies, even if we do not have enough information to quantify the corresponding systematic error.

5.2.3 The Flavor-Singlet Goldstone Boson

As explained in Sec. 5.1.3, the chiral fit in the fundamental and sextet sectors allows us to probe the flavor-singlet ζ meson as well. We examine its mass in the chiral-sextet limit, $\hat{m}_6 \to 0$. Figure 5.6 shows $\hat{M}_\zeta^2$, constructed using Eq. (5.18) and the parameters of the central fit, in the continuum ($\hat{a} \to 0$) limit, as a function of the mass $\hat{m}_4$ of the fundamental fermions. The figure shows that the flavor-singlet boson is consistently lighter than the pseudoscalar of the fundamental

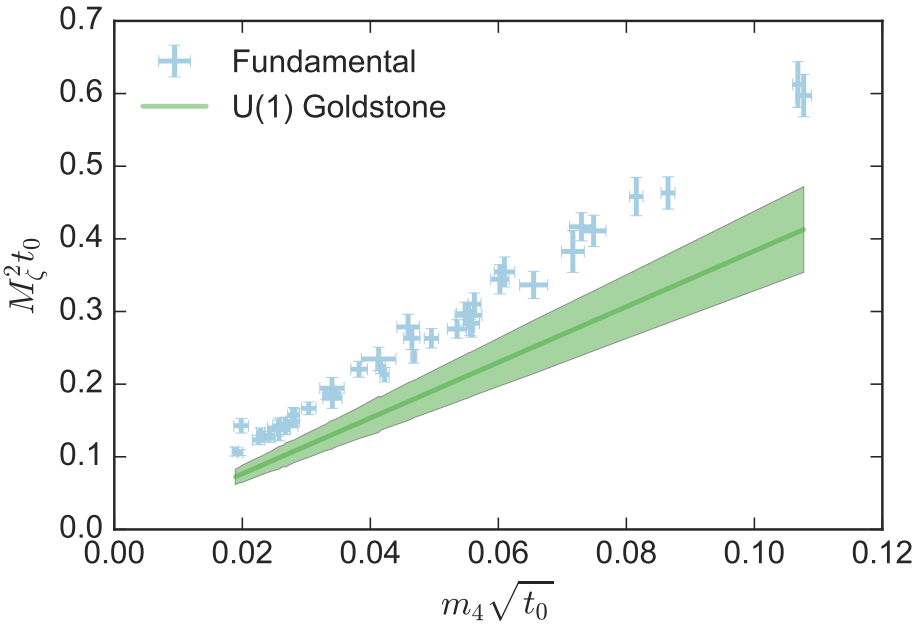

Figure 5.6: Mass squared $\hat{M}_\zeta^2$ of the non-anomalous Goldstone boson in the combined continuum ($\hat{a} \to 0$) and chiral-sextet ($\hat{m}_6 \to 0$) limits, as extracted using Eq. (5.18) and the central fit's parameters, plotted against $\hat{m}_4$. The pseudoscalar mass $\hat{M}_4^2$ in the fundamental sector in the same limit is shown for comparison.

sector in this limit.

We can make a conservative prediction regarding the ζ mass as follows. As we have just explained, we do not know how large $\hat{m}_4$ can be while keeping the N^{2}LO corrections below, say, 10% or 20%. Lowering the maximal value of $\hat{m}_4$ raises the uncertainty in $\mathring{F}_\zeta$, as seen in Fig. 5.5. Still, even if we lower the maximal value of $\hat{m}_4$ so as to, say, double the uncertainty of $\mathring{F}_\zeta$, we would still find that $M_\zeta^2 < M_4^2$ at the level of one standard deviation (1σ).

The chiral-sextet limit is interesting for composite-Higgs models. In many models, including those proposed by Ferretti and Karateev [77], the symmetries of the Standard Model are embedded into the unbroken global symmetries, so that neither the fundamental nor the sextet fermions are required to be strictly massless. Nonetheless, successful models are likely to have very light sextet fermions, because a large sextet mass would prevent the Higgs field from condensing even after the

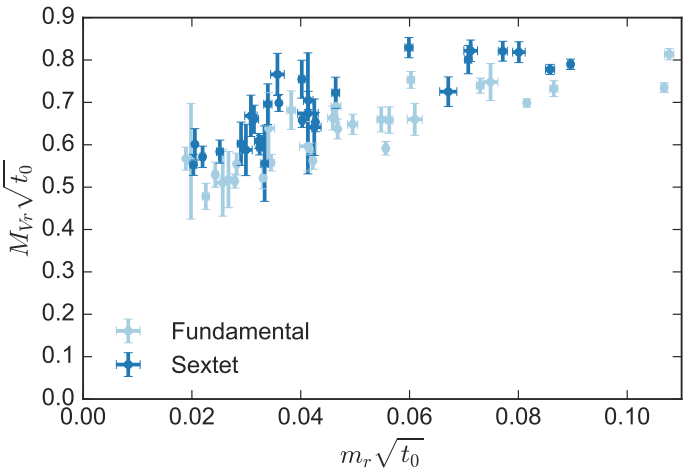

Figure 5.7: Vector masses vs fermion masses in units of the flow scale t_0.

generation of a potential from the coupling of the Higgs to Standard Model fields.

5.3 Vector Mesons

5.3.1 Masses and Decay Constants

We now turn to our results for vector masses and decay constants. Vector-meson decay constants appear in the literature with a variety of conventions. We define F_{Vr} to have units of energy,

$$\left\langle 0 \middle| V_{ia}^{(r)} \middle| V_{jb}^{(r)} \right\rangle = \delta_{ab}\delta_{ij} F_{Vr} M_{Vr} \ , \tag{5.28}$$

where the vector meson is at rest. The indices are $i, j = 1, 2, 3$, for the spatial directions, and as usual, $a, b = 1, 2, 3$, for isospin. This definition is frequently used in the phenomenology literature on precision electroweak observables, for example Ref. [123].

Figures 5.7 and 5.8 show results for $\hat{M}_{Vr}$ and $\hat{F}_{Vr}$, respectively, each plotted against the fermion mass $\hat{m}_r$ in the same representation. As before, we measure all quantities in units of t_0. The data for these figures are listed in Tables D.10–D.12. Both quantities shows a modest, plausibly linear rise against the fermion mass, albeit with a large spread.

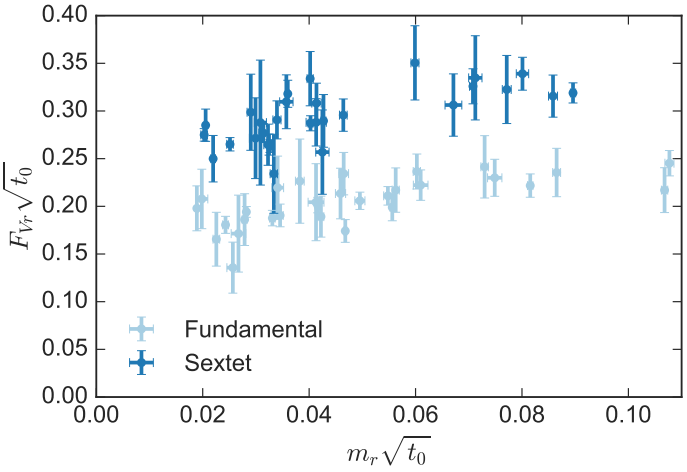

Figure 5.8: Vector decay constants vs fermion masses in units of the flow scale t_0.

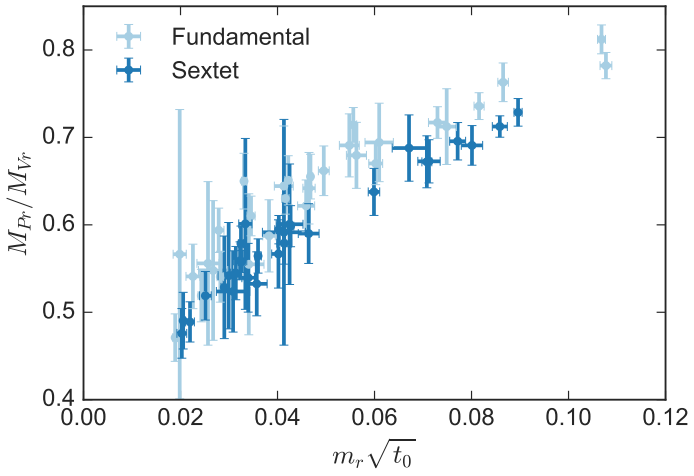

Figure 5.9: The mass ratio M_{Pr}/M_{Vr} in a fixed representation.

Figure 5.9 shows the ratio of the pseudoscalar and vector masses, M_{Pr}/M_{Vr}, again plotted against the fermion mass $\hat{m}_r$ in the same representation. This ratio is greater than or equal to one half for all but the smallest masses. Because the decay $V \to PP$ is p-wave, the vector is stable if $M_P/M_V > 0.5\sqrt{1 - 4k_{\text{min}}^2/M_V^2}$, where $k_{\text{min}} = 2\pi/L$ is the minimum nonzero momentum. This condition is satisfied for both representations on all of our ensembles, so the vectors are indeed stable.

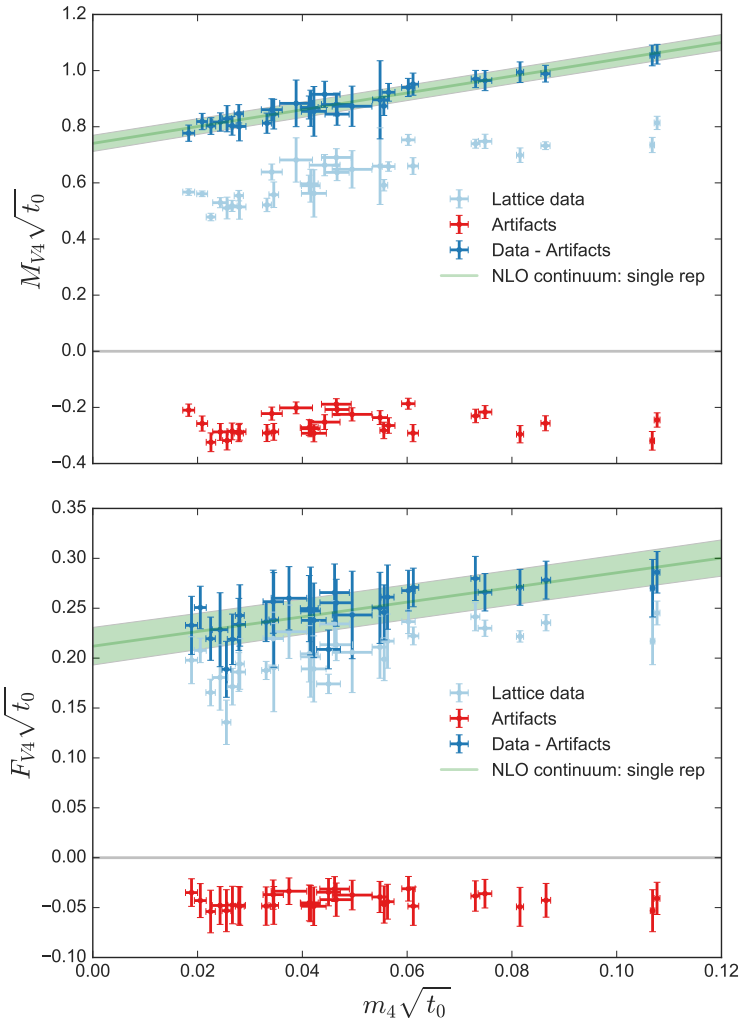

Figure 5.10: Breakdown of the contribution of lattice artifacts in the empirical models for the vector masses and decay constants in the fundamental representation.

We model $\hat{M}_{Vr}$ and $\hat{F}_{Vr}$ as linear functions of the fermion mass in the same representation and of the lattice spacing, for example,

$$\hat{M}_{V4} = c_0 + c_1\hat{m}_4 + c_2\hat{a} \ . \tag{5.29}$$

For this analysis, we restrict ourselves to the 30 ensembles for which we were able to measure the

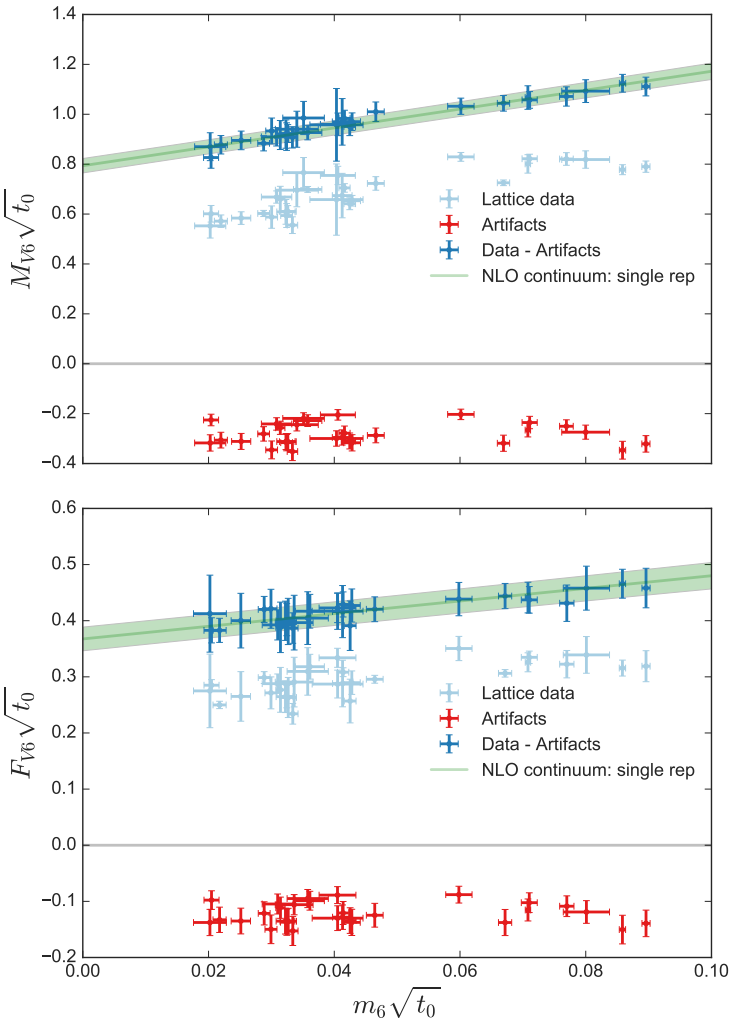

Figure 5.11: Breakdown of the contribution of lattice artifacts in the empirical models for the vector masses and decay constants in the sextet representation.

vector decay constants (see Tables D.10—D.12). The individual correlated fits are successful, with typical $\chi^2/\text{DOF} \lesssim 1.0$ for $30 - 3 = 27$ degrees of freedom. Figures 5.10 and 5.11 illustrate the contribution of lattice artifacts to these fits in the same manner as for the pseudoscalars above; the green bands represent the linear continuum terms in each fit.

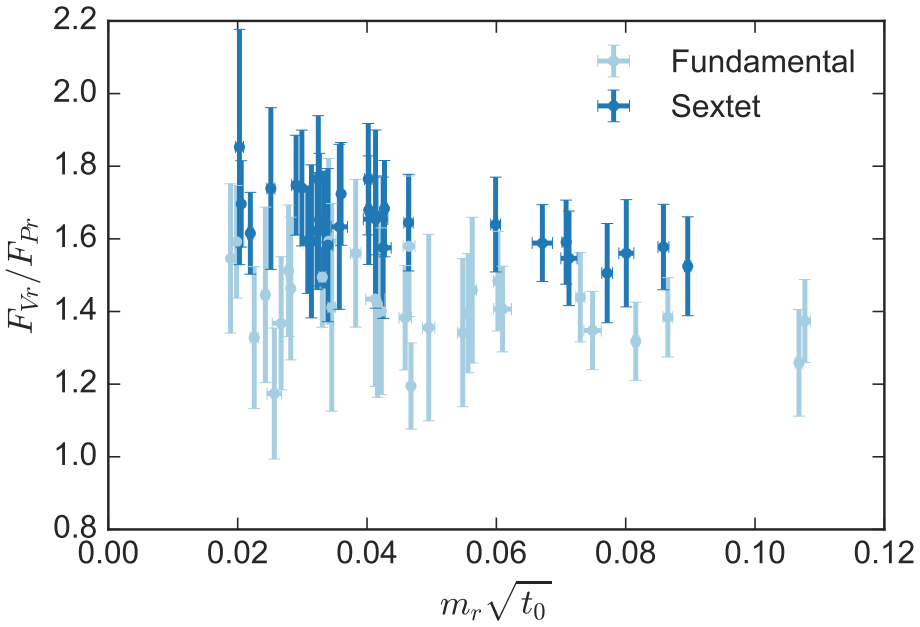

Figure 5.12: The ratio of the vector and pseudoscalar decay constants in each representation. The KSRF prediction is a constant value of $\sqrt{2}$.

5.3.2 Vector Meson Dominance and the KSRF Relations

The pseudoscalar and vector decay constants are related through the hypothesis of vector meson dominance (VMD). Kawarabayashi, Suzuki, Riazuddin, and Fayyazuddin (KSRF) showed long ago [104, 126, 100] that VMD leads to the prediction

$$F_V = \sqrt{2} F_P \ , \tag{5.30}$$

independent of representation. Figure 5.12 shows the ratio F_{Vr}/F_{Pr} in each representation, after subtracting lattice artifacts. The KSRF prediction is qualitatively successful. For comparison, the experimental value is roughly 1.66 in QCD.

Another result of KSRF is that the on-shell coupling constant g_{VPP} mediating the decay of a vector into two pseudoscalars is given by

$$g_{VPP} = \frac{M_V}{F_P} \ . \tag{5.31}$$

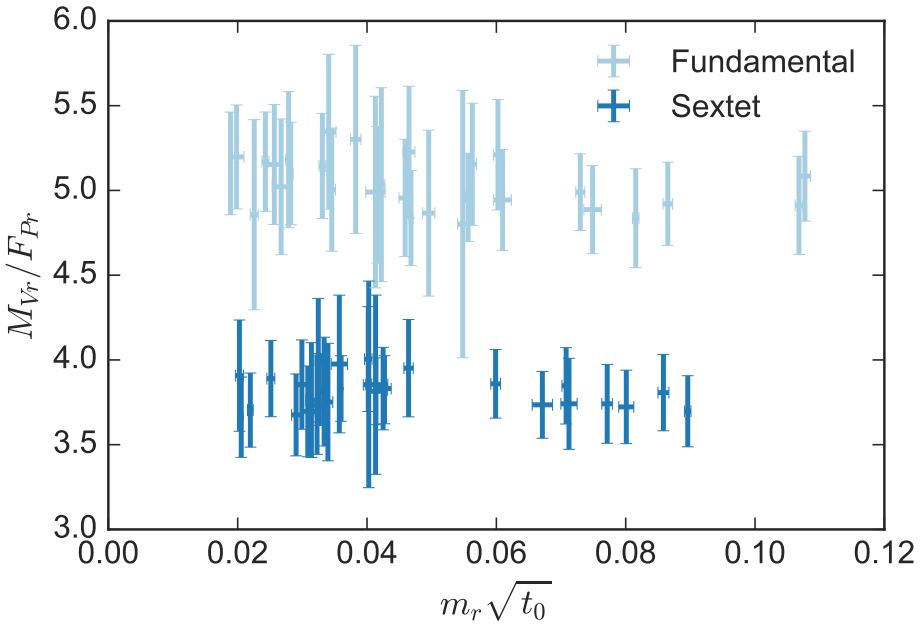

Figure 5.13: The ratio of the vector mass and pseudoscalar decay constant in a fixed representation. KSRF identify this quantity with the coupling g_{VPP}. In QCD, this ratio is roughly 5.9.

We plot this ratio in Fig. 5.13. As already noted, in our ensembles the vector meson is stable. Nevertheless, we may use the KSRF result as a phenomenological estimate for the behavior close to the chiral limit. Using the tree-level formula for the $V \to PP$ decay width in the limit where $M_{Pr} \ll M_{Vr}$,

$$\Gamma_{V\to PP} \simeq \frac{g_{VPP}^2 M_V}{48\pi} \ , \tag{5.32}$$

we can estimate the the mass-to-width ratio for each vector resonance,

$$\frac{\Gamma_{V\to PP}}{M_V} \simeq \frac{M_V^2}{48\pi F_P^2} \ . \tag{5.33}$$

From Fig. 5.13 we thus obtain Fig. 5.14. For the physical ρ meson, this ratio has a value of roughly 0.23. (The experimental value is 0.19.)

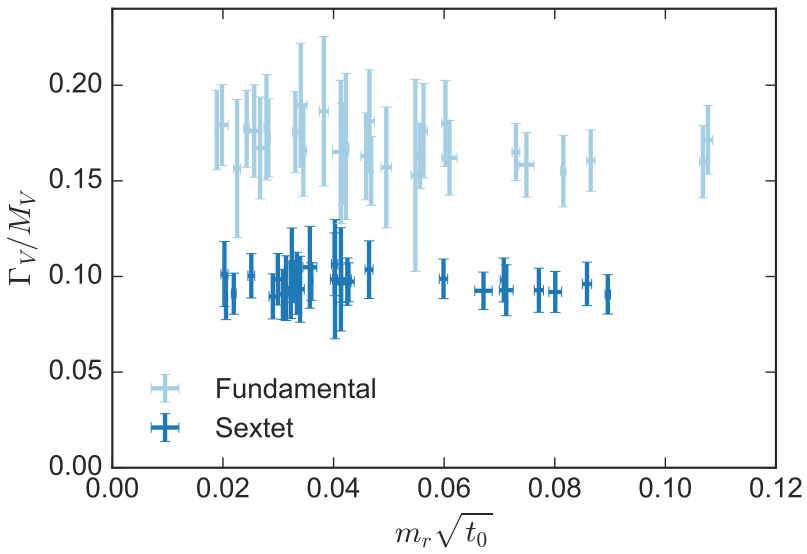

Figure 5.14: Tree-level estimates for the width-to-mass ratio of the vector mesons according to KSRF. The KSRF estimate for this ratio is roughly 0.23 in QCD.

5.4 Summary of Meson Results

Our analysis of the meson spectrum focused on the masses of the pseudoscalar and vector states and their associated decay constants. Using chiral perturbation theory (and its extension to include discretization errors from Wilson fermions), we carried a global analysis of the pseudoscalar masses and decay constants of the two representations. This EFT analysis employed next-to-leading order formulae in the generic small mass power-counting scheme. We found significant lattice artifacts, which we were able to subtract, obtaining predictions in the joint chiral-continuum limit. Our fit provided mild evidence for coupling between the two fermion representations, a novel feature of multirep theories.

Our lattice formulation in terms of Wilson fermions explicitly breaks the global symmetries according to the expected patterns: $\mathrm{SU}(2)_L \times \mathrm{SU}(2)_R \to \mathrm{SU}(2)_V$ in the fundamental sector, and $\mathrm{SU}(4) \to \mathrm{SO}(4)$ in the sextet sector. We did not carry out a dedicated study of alternative symmetry breaking patterns. Nevertheless, the success of the chiral fits provides some confirmation that the above symmetry breaking patterns are the right ones.

The main theoretical uncertainty of our chiral fits concerns the size of N^{2}LO effects. Thanks to a large decay constant, the chiral expansion converges quickly in the sextet sector, supporting the hypothesis that N^{2}LO effects are small in this sector. In the fundamental sector the chiral expansion converges more slowly. Hence, keeping N^{2}LO effects below a certain comfortable level might require the exclusion of ensembles where $\hat{m}_4$ is on the high side. Our data do not allow more quantitative statements.

We computed correlation functions of the the pseudoscalar states made purely of fundamental fermions or purely of sextet fermions. The fact that we measure these states directly is reflected in the stability of the LO parameters $\mathring{F}_r$ and $\mathring{B}_r$ under different cuts on the maximal value of $\hat{m}_4$. In contrast, our measurement of the final LO parameter, the decay constant $\mathring{F}_\zeta$ of the flavor-singlet Goldstone boson, was indirect because we did not calculate propagators in the ζ channel. However, the ζ meson does contribute through virtual loops to the correlations functions we did study. More precisely, the EFT predicts contributions from NLO logarithmic terms in our fit functions. As a result of this indirect role played by the ζ, both its decay constant and the reconstructed prediction for its mass were more sensitive to cuts on $\hat{m}_4$. Nevertheless, we argued that the ζ is lighter than the fundamental-sector Goldstone bosons ($M_\zeta < M_4$) in the sextet-chiral limit ($\hat{m}_6 \to 0$). This limit is interesting for the phenomenology of Ferretti's model, where the Higgs boson begins as an exactly massless sextet Goldstone boson before coupling to the Standard Model. In a full composite-Higgs model, however, the masses of all pseudoscalar states can receive important corrections from the couplings to Standard Model fields.

In modeling our results for the vector mesons, we found that the ratio of pseudoscalar to vector decay constants agrees well with the KSRF result based on vector meson dominance. Comparing the KSRF prediction for the decay rate of the vector meson in the chiral limit to the QCD case shows reasonable agreement with large-N_c counting.

Although our estimates for the decay width Γ_V/M_V depend on the well-motivated but non-rigorous assumption of vector meson dominance, the resulting narrowness is almost certainly generic. In large-N_c, the widths of mesons made of fundamental-representation fermions scales

as $1/\sqrt{N_c}$ and thus become narrower as N_c increases. Insofar as large-N_c provides the cleanest explanation for the narrowness and existence of mesons in QCD, the vector mesons should become narrower in theories with more colors. We proposed that in multirep theories, the generalization of $\sqrt{N_c}$ is $(\dim r)^{1/2}$, a hypothesis supported by our data. This result is good news for phenomenologists looking to constrain models like the Ferretti model, since narrower states typically provide clearer signals in collider data.

Chapter 6

The Baryon Spectrum

6.1 Overview

In the context of the Ferretti composite Higgs model, knowing the spectrum of baryon states allows for concrete predictions about their future discovery potential in LHC searches. One baryon state, made up of valence fermions from both the **4** and **6** representations, is of particular interest. In the model it carries the same Standard Model quantum numbers as the top quark, and in fact serves as a top partner. As a top partner, it plays a crucial role in the generation of the Higgs potential and of the top-quark mass itself. We refer to these bound states as "chimera" baryons, due to their mixed composition.

Aside from phenomenology beyond the Standard Model, this system offers a rich testing ground for a generalized version of the familiar quark model description of hadronic physics, containing baryons with different expected behavior in the large-N_c limit. Since baryons in QCD only contain quarks in a single representation, the chimera states are particularly novel from a quark-model perspective.

Our analysis will spend more time on models than is common in modern QCD simulations. The present work is an exploratory study of a new system with many baryon states, and it is useful to have an organizing principle to present them. It is also useful to be able to compare the spectroscopy of this system to that of real-world QCD. Models are a good way to do that. The models may also be useful in phenomenology of this and similar theories.

Baryon correlation functions are noisy, so the present study uses only a subset of our full

	min	max
t_0/a^2	1.06	2.67
M_{P4}/M_{V4}	0.55	0.79
M_{P6}/M_{V6}	0.47	0.73
$M_{p4}L$	4.23	8.16
$M_{p6}L$	4.03	8.91

Table 6.1: Summary of basic physical properties of the ensembles used in this study.

data set, focusing on a dozen ensembles with sufficient statistics to achieve reliable measurements of the baryon spectrum. In lieu of repeating the technical details, we summarize some features of these ensembles in Table 6.1.

All the ensembles in the present analysis have volume $V = 16^3 \times 32$. In the meson study, we estimated the finite volume effects for mesons and concluded that they were at the level of a few percent [10]. Baryons, of course, are a different story, because their sizes are expected to be larger than those of mesons. Still, the pseudoscalar decay constants in the SU(4) gauge theory are larger than those of SU(3) and, since finite volume corrections from pion loops are proportional to $1/F_P^2$, we expect that they are smaller than in SU(3) (see Ref. [10] for a discussion). Sec. 6.6 presents a preliminary estimate of finite-volume effects in our analysis.

Tables containing the various measured quantities have been collected together in Appendix D.

6.2 Baryons in SU(4) with Two Representations

The spectrum of the lightest s-wave baryons in this theory consists of three classes of states with differing valence fermion content: fundamental-only baryons, sextet-only baryons, and mixed-representation baryons. Fundamental-only baryons contain four valence fermions and have nonzero $\mathrm{U}(1)_B$. We shall denote these bosonic states as q^4 states. Sextet-only baryons contain six valence fermions and we will denote these bosons as Q^6 states. No unique definition of baryon number exists for these pure-sextet objects, although one can single out one of the unbroken SO(4) generators and call it a baryon number. In practice we shall only discuss the Q^6 states with color indices contracted against the Levi-Civita symbol of SO(6), as in Ref. [62]. [We remind the reader that

the defining representation of SO(6) is isomorphic to the **6** of SU(4).] Finally, the color-singlet combination of two fundamentals with a single sextet fermion gives a mixed-representation baryon containing three fermions. We shall denote these fermionic states as Qqq states and refer to them as chimera baryons.

The lightest Qqq chimera baryons are expected to be stable under strong decay, due to conservation of fundamental baryon number $\mathrm{U}(1)_B$. The q^4 baryons can decay into a pair of chimeras, and a q^4 baryon will be stable only if it is sufficiently light. Because the **6** of SU(4) is a real representation, di-fermion QQ states live in the same multiplets with fermion-antifermion $\overline{Q}Q$ states; the same applies to the four-fermion states $QQQQ$, $\overline{Q}QQQ$, etc. The Q^6 states are unstable against decay into three QQ particles, which include in particular some of the states in the Goldstone multiplet of $\mathrm{SU}(4) \to \mathrm{SO}(4)$ symmetry breaking [62].

Mixed-representation baryons represent a new sort of baryon, but the relevant interpolating fields are closely related to those of the QCD hyperons containing a single strange quark (i.e., Σ^*, Σ, and Λ), with the lone sextet fermion playing the role of the strange quark. From a computational perspective, the only new feature is the presence of an additional color SU(4) index for the sextet fermion; details appear in Appendix C. As in QCD, these mixed-representation baryons are classified according to their total spin J and the isospin I of the qq pair; the three possible states are identified as $\Sigma^\star, (J,I) = (3/2,1)$; $\Sigma, (J,I) = (1/2,1)$; and $\Lambda, (J,I) = (1/2,0)$. Total antisymmetry of the operator under exchange of identical fermions forbids a spin-3/2 isosinglet state. The chimera analogue of the Λ is of particular phenomenological interest, since it plays the role of a partner for the top quark in Ferretti's model. More information relating to its role as the top partner appears below.

6.3 Continuum Large-N_c Expectations

The properties of both q^4 and Q^6 baryons have been studied in the continuum (a partial list of references are Refs. [145, 146, 50, 51, 97, 49, 31]) and on the lattice (in quenched simulations and in ones with a single representation of dynamical fermion—see Refs. [55, 56, 39, 8, 62]). These

states form multiplets in which angular momentum and isospin (flavor) are locked together, $I = J = 0, 1, \ldots N/2$ where $N = 4$ or 6 for the q^4 and Q^6 states. For the q^4 states, this is an aspect of the "contracted SU($2N_c$)" symmetry of large-N_c baryons [85, 84, 52, 118].

Large-N_c predicts that masses of single-representation baryons, which are classified according to their total spin J, should follow a rotor formula. Mass formulas through $\mathcal{O}(1/N_c)$ for these baryons are given in Refs. [2, 96, 35]:

$$M_B = \dim_r M_r^{(0)} + M_r^{(1)} + B_{rr}\frac{J(J+1)}{\dim_r} \tag{6.1}$$

$$= \begin{cases} 4M_4^{(0)} + M_4^{(1)} + B_{44}\frac{J(J+1)}{4}, \text{ for } q^4 \\ 6M_6^{(0)} + M_6^{(1)} + B_{66}\frac{J(J+1)}{6}, \text{ for } Q^6, \end{cases} \tag{6.2}$$

where the dimensions of the representations are $\dim_r = N_c$ for the fundamental and $\dim_r = N_c(N_c-1)/2$ for the two-index antisymmetric representation. In these expressions, the bulk of the mass of the baryons comes from the leading-order constituent mass term proportional to $\dim_r$. Subleading corrections appear in the term $M_r^{(1)}$ and the rotor splitting B_{rr}. Because the N_c-dependence has been made explicit, no *a priori* hierarchy is assumed to exist among the parameters $M_r^{(0)}$, $M_r^{(1)}$ and B_{rr}.

Large-N_c together with arguments involving spin-flavor symmetry furnish further predictions for mixed-representation baryons [51]. The key insight is that mixed-representation baryons can be classified according to the (unbroken) flavor symmetry of the fundamental fermions, $\mathrm{SU}(2)_I \times \mathrm{U}(1)_B$. With this symmetry, it can be shown that

$$M_{Qqq} = 2\widetilde{M}_4^{(0)} + \widetilde{M}_6^{(0)} + \widetilde{M}_{\mathrm{mix}}^{(1)} + \widetilde{B}_{46}\frac{J(J+1)}{\sqrt{24}} + \left(\frac{\widetilde{B}_{44}}{4} - \frac{\widetilde{B}_{46}}{\sqrt{24}}\right) I(I+1). \tag{6.3}$$

Several comments are in order. First, writing down Eqs. (6.1) and (6.3) required no model assumptions beyond large-N_c counting. The factors of 4 and 6 are conventional. Second, the tildes in Eq. (6.3) remind us that, from the perspective of large-N_c, the expansion parameters of the single-representation baryons are completely unrelated to those of the mixed-representation baryons. The raw lattice data will soon demonstrate, however, that there is good reason to believe

that they are in fact related (e.g., $\widetilde{B}_{44} \simeq B_{44}$). Third, each of the parameters above is implicitly a function of the fermion masses m_4 and m_6.

6.4 Baryon Masses on the Lattice

Motivated by the general arguments above, we now turn to models for describing our lattice data. As with the meson spectrum, we express all quantities in units of the gradient-flow length scale $\sqrt{t_0}$ [115]. Consistent with previous notation, the use of a hat distinguishes these quantities from the corresponding values in lattice units, e.g., $\hat{M}_B \equiv (M_B\, a)(\sqrt{t_0}/a)$.

Our simulations are performed across a wide spread of lattice spacings, allowing us to model and remove lattice artifacts. We expect that the leading-order lattice correction to dimensionless ratios will be linear in the lattice spacing, for instance,

$$(Ma)\left(\frac{\sqrt{t_0}}{a}\right) = M\sqrt{t_0} + \mathcal{O}(a) + \cdots . \tag{6.4}$$

For each individual baryon mass, one therefore supposes that

$$\hat{M}_B = \hat{M}_B^0 + A_B\hat{a} + \cdots , \tag{6.5}$$

where $\hat{M}_B^0$ is the continuum limit value and A_B is an artifact coefficient. Eq. (6.5) does not yet include any explicit dependence on the input fermion masses. One could consider a simple linear dependence on the valence fermion mass $\hat{m}_v$ (for the q^4 or Q^6 states),

$$\hat{M}_B = \hat{M}_B^0 + \hat{M}_B^1\hat{m}_v + A_B\hat{a}, \tag{6.6}$$

or perhaps on both valence and sea masses,

$$\hat{M}_B = \hat{M}_B^0 + \hat{M}_B^1\hat{m}_v + \hat{M}_b^2\hat{m}_s + A_B\hat{a}. \tag{6.7}$$

In a fit of this form, one would expect $\hat{M}_b^1 > \hat{M}_b^2$, reflecting the fact that the baryon mass depends predominantly on the valence fermion mass.

One could also consider a more complex model based on Eq. (6.1), in which all the coefficients have their own lattice artifacts ($\hat{B}_{rr} = \hat{B}_{rr}^0 + \hat{B}_{rr}^1\hat{a}$, for example). In practice, we find that a single

artifact term reproduces all the spectroscopy in a multiplet. Our model for the lattice baryon spectrum is hence

$$\hat{M}_{Q^6} = 6\left[C_6 + C_{66}\hat{m}_6\right] + \frac{B_{66}}{6}J(J+1) + A_6\hat{a}, \tag{6.8}$$

$$\hat{M}_{q^4} = 4\left[C_4 + C_{44}\hat{m}_4\right] + \frac{B_{44}}{4}J(J+1) + A_4\hat{a}, \tag{6.9}$$

$$\begin{aligned}\hat{M}_{Qqq} = {} & 2\left[C_4 + C_{44}\hat{m}_4\right] + \left[C_6 + C_{66}\hat{m}_6\right] + C_{\rm mix} + A_{\rm mix}\hat{a} \\ & + B_{46}\frac{J(J+1)}{\sqrt{24}} + \left(\frac{B_{44}}{4} - \frac{B_{46}}{\sqrt{24}}\right)I(I+1).\end{aligned} \tag{6.10}$$

The constants proportional to $\hat{a}$ are the explicit lattice artifact terms.

It is also worth noting that independent of any fitting, the compatibility of the rotor formula (6.1) with our baryon mass results can be tested across fermion mass values with an analog of the Landé interval rule: ratios of differences $(M_B(J_1) - M_B(J_2))/(M_B(J_3) - M_B(J_4))$ should be pure numbers, depending only on the J's. We will present such a test below as a check on our more elaborate results based on fitting.

The parameters of the lattice models above are related to those of the original large-N_c formulas according to the following relations:

$$\widetilde{M}_4^{(0)} = M_4^{(0)} + M_4^{(1)}/4 = C_4 + C_{44}\hat{m}_4, \tag{6.11}$$

$$\widetilde{M}_6^{(0)} = M_6^{(0)} + M_6^{(1)}/6 = C_6 + C_{66}\hat{m}_6, \tag{6.12}$$

$$C_{\rm mix} = \widetilde{M}_{\rm mix}^{(1)} - M_4^{(1)}/4 - M_6^{(1)}/6. \tag{6.13}$$

This redefinition is desirable from a numerical perspective, since the original large-N_c formulas contain more independent parameters than can be distinguished by data at a single value of N_c. Since the three multiplets of states furnish three linear relations among the constituent masses, a fit can only distinguish between three independent linear combinations of the constituent mass parameters.

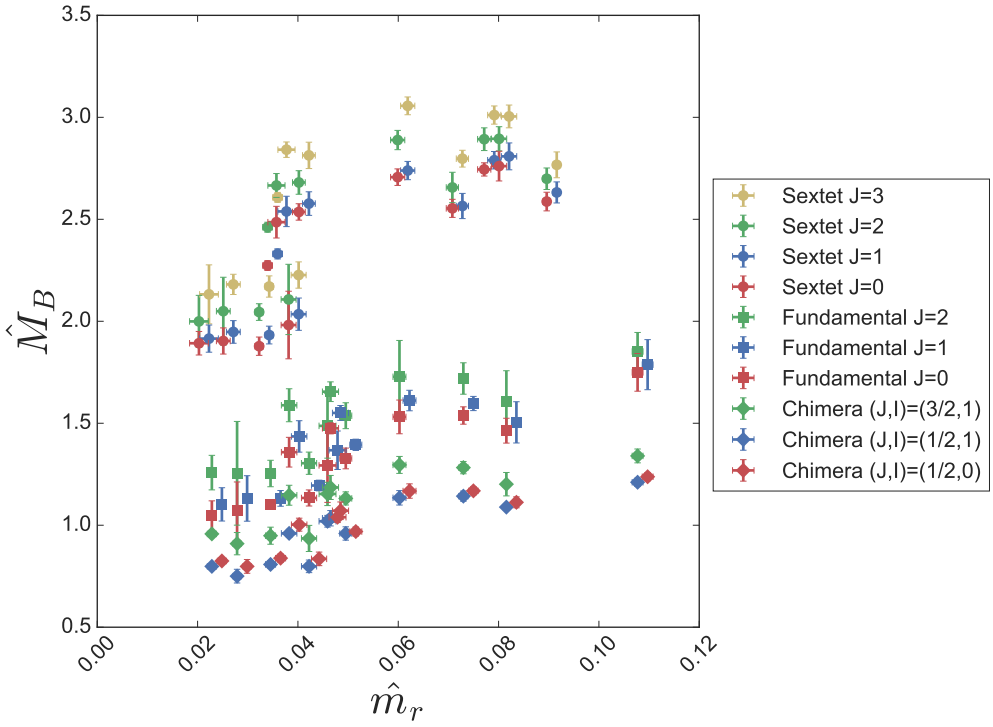

Figure 6.1: Lattice data for the baryon mass spectrum $\hat{M}_B$. The horizontal positions contain small offsets to reduce overlap and aid readability.

6.5 Spectrum Results

The tables containing the measured values for the baryons have been collected together in Appendix D. The figures in this section summarize the content of the tables. Figure 6.1 shows the measured spectrum of baryon masses. Masses of single-representation baryons $\hat{M}_r$ are plotted as functions of the corresponding AWI fermion mass $\hat{m}_r$. The chimera baryons are plotted as a function of $\hat{m}_4$, although one expects some dependence on $\hat{m}_6$ as well. The baryon masses all increase with fermion mass, but no clear functional dependence is conspicuous. As in our meson study, lattice artifacts—which we shall model and remove—obscure the underlying linear nature of our data. To motivate the forthcoming analysis in Sec. 6.6, we first consider evidence for the models which exists *before* fitting.

According to the large-N_c model of Eq. (6.1), ratios of baryon mass differences for the q^4 or Q^6 states are parameter-free functions of the spins. In particular, the parameter B_{rr} only controls

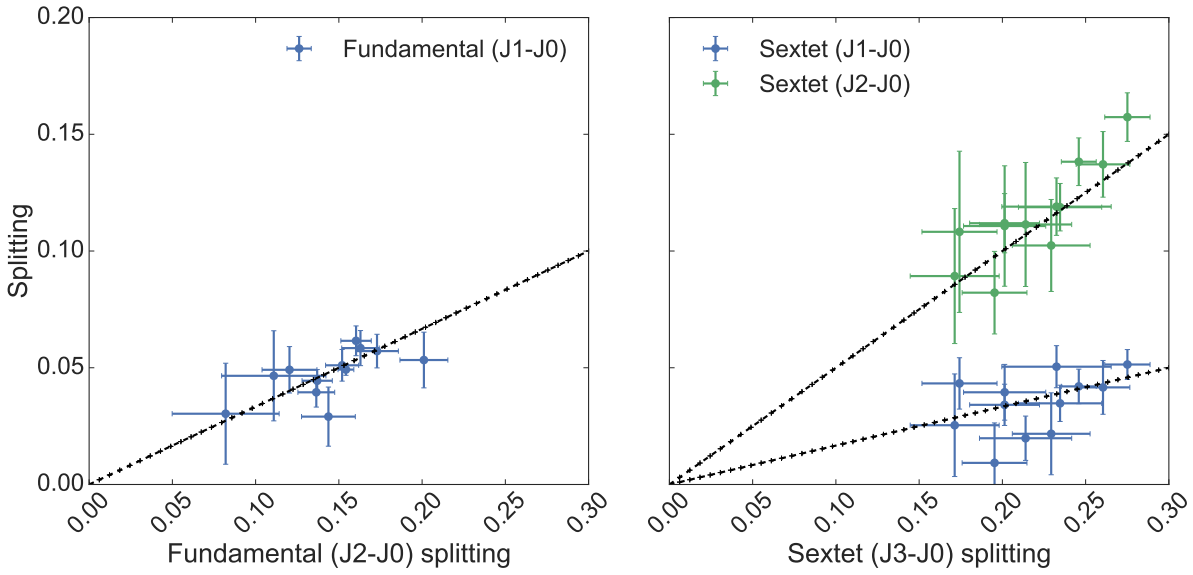

Figure 6.2: Mass splittings between baryons in the fundamental (left) and sextet (right) representations. The lines indicate the expected $J(J+1)$ behavior.

the overall size of the splittings. Figure 6.2 shows mass differences among the single-representation baryons, with errors on the differences from a jackknife. The dotted lines are the expected values from $J(J+1)$ splittings. The rotor behavior is clearly evident in the raw data.

For single-representation baryons, the mass of the $J = 0$ state furnishes estimates for the individual constituent masses. The constituent mass of a chimera baryon is therefore nearly

$$\hat{M}_{Qqq,\text{constituent}} \simeq \frac{\hat{M}_{q^4}^{(J=0)}}{2} + \frac{\hat{M}_{Q^6}^{(J=0)}}{6}. \tag{6.14}$$

On the other hand, one can use Eq. (6.3) to eliminate the splitting terms in favor of the spin independent contribution by averaging the chimera baryon masses together with appropriate weights,

$$\hat{M}_{Qqq,\text{constituent}} \simeq \left(2\hat{M}_{Qqq}^{(J,I)=(3/2,1)} + \hat{M}_{Qqq}^{(J,I)=(1/2,1)} + \hat{M}_{Qqq}^{(J,I)=(1/2,0)}\right)/4. \tag{6.15}$$

Figure 6.3 shows these two raw-data estimates for the total constituent mass of the chimera baryons plotted against each other, with errors from a jackknife. The line indicates equality, as predicted by the large-N_c model. The impressive agreement of the two estimates suggests that the chimera baryons should be modeled together with the single-representation baryons.

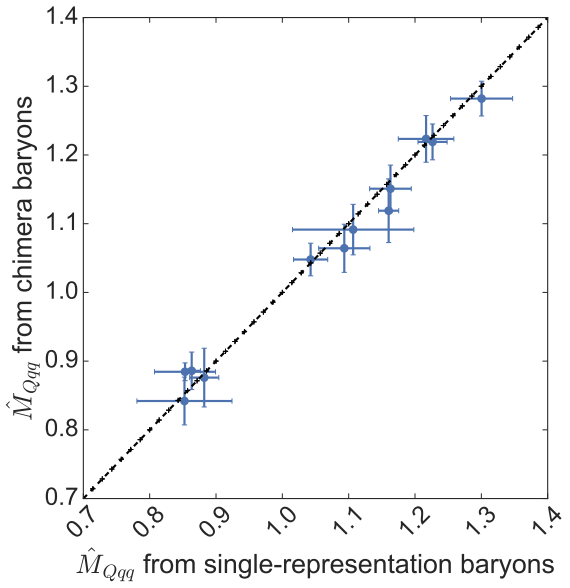

Figure 6.3: Estimates for the total constituent mass of the chimera baryons from the chimeras themselves (vertical axis) again the estimates from single-representation baryons (horizontal axis). The line indicates the expectation that the two independent estimates agree.

Finally, we examine the strength of the splitting terms. Equation (6.10) says that

$$B_{44} = \frac{2}{3}\left(2\hat{M}_{Qqq}^{(J,I)=(3/2,1)} + \hat{M}_{Qqq}^{(J,I)=(1/2,1)} - 3\hat{M}_{Qqq}^{(J,I)=(1/2,0)}\right), \tag{6.16}$$

$$B_{46} = \frac{\sqrt{24}}{3}\left(\hat{M}_{Qqq}^{(J,I)=(3/2,1)} - \hat{M}_{Qqq}^{(J,I)=(1/2,1)}\right). \tag{6.17}$$

Likewise, the single representation formulas (6.8) and (6.9) say that

$$B_{44} = \frac{2}{3}\left(\hat{M}_{q^4}^{(J=2)} - \hat{M}_{Q^6}^{(J=0)}\right), \tag{6.18}$$

$$B_{66} = \frac{1}{2}\left(\hat{M}_{Q^6}^{(J=3)} - \hat{M}_{Q^6}^{(J=0)}\right). \tag{6.19}$$

Figure 6.4 shows these estimates for the rotor splitting coefficients B, displayed as functions of $\hat{m}_4$ ($\hat{m}_6$) in the left (right) pane, with errors from a jackknife.

Physically-motivated models of baryons predict different mass dependence for the splitting coefficients. For instance, if the $J(J+1)$ term arises from rigid rotation (e.g., of a skyrmion), the coefficient should scale inversely with the mass of the baryon [2]. In non-relativistic quark models, the splittings arise from a color hyperfine interaction and (in analogy with the familiar hyperfine

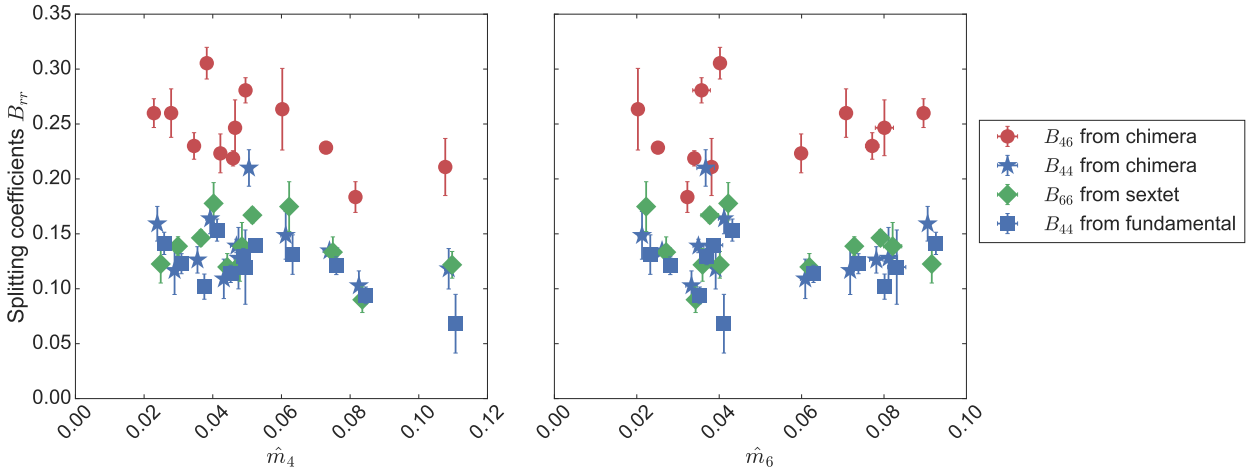

Figure 6.4: Estimates of the splitting coefficients B_{44}, B_{66}, and B_{46} on each ensemble as functions of $\hat{m}_4$ (left) and $\hat{m}_6$ (right). The horizontal positions contain small offsets to reduce overlap and aid readability.

interaction of atomic physics) scale inversely with the square of the constituent quark mass [53]. The raw data show considerable spread, and no particular functional dependence is evident for any of the B coefficients in either pane. The models (6.8), (6.9), and (6.10) therefore treat the B coefficients as constants. It is worth noting that the two independent estimates of B_{44} from the fundamental baryons (squares) and from the chimera baryons (stars) are consistent within the uncertainty of the data.

Another feature of Fig. 6.4 is the large value of B_{46} compared to the other splitting coefficients. This is easily understood in a model where the spin splittings are due to one-gluon exchange, that is, $V_{ij} \propto C_{ij}\mathbf{S}_i \cdot \mathbf{S}_j$ where C_{ij} is a color factor and $\mathbf{S}_i$ is the spin of constituent i. The appropriate color factors are $C_{qq} = 5/8$ for the q^4 baryons (and for the qq diquark in the Qqq baryon), $C_{QQ} = 1/2$ for the Q^6 baryons, and $C_{Qq} = 5/4$ for the mixed interaction chimeras. In other words, one expects $B_{46}/B_{44} \sim C_{Qq}/C_{qq}$ and $B_{46}/B_{66} \sim C_{Qq}/C_{QQ}$. This expectation is in agreement with the qualitative behavior of Fig. 6.4, which suggests that B_{46} is roughly twice as large as B_{44} or B_{66}.

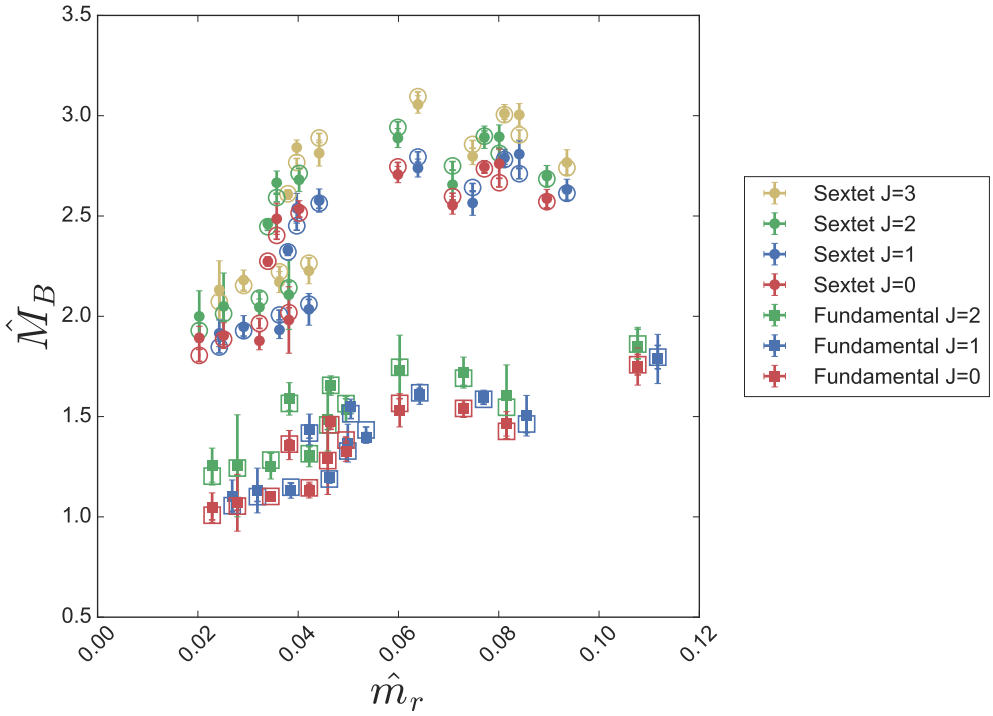

Figure 6.5: Data (solid marker) and linear fits (open marker) to each state in the fundamental and sextet multiplets using the simple linear model (6.5), including a linear term proportional to $\hat{a}$. The error bars of the open markers are those of the fit. The horizontal positions contain small offsets to reduce overlap and aid readability.

6.6 Fitting Mass and Lattice-Spacing Dependence

We now present fit results modeling the dependence of our baryons on the fermion masses and lattice spacing. To justify the assumption that lattice artifacts are proportional to $\hat{a}$ in our general model, we begin by conducting a simple linear fit following Eq. (6.5) for each state individually in the fundamental and sextet multiplets. Figure 6.5 shows the result of these fits, which are in excellent agreement with the data. The parameter corresponding to the artifact is approximately the same for all the states within a given multiplet, giving support to the models of Eqs. (6.8)–(6.10). The case for the chimera baryons is similar, using Eq. (6.6) which is linear in both $\hat{m}_4$ and $\hat{m}_6$.

Based on the success of these simple fits, we proceed to a simultaneous global fit. Using Eqs. (6.8)–(6.10), we simultaneously model all 10 baryon masses on 12 ensembles. Single-elimination

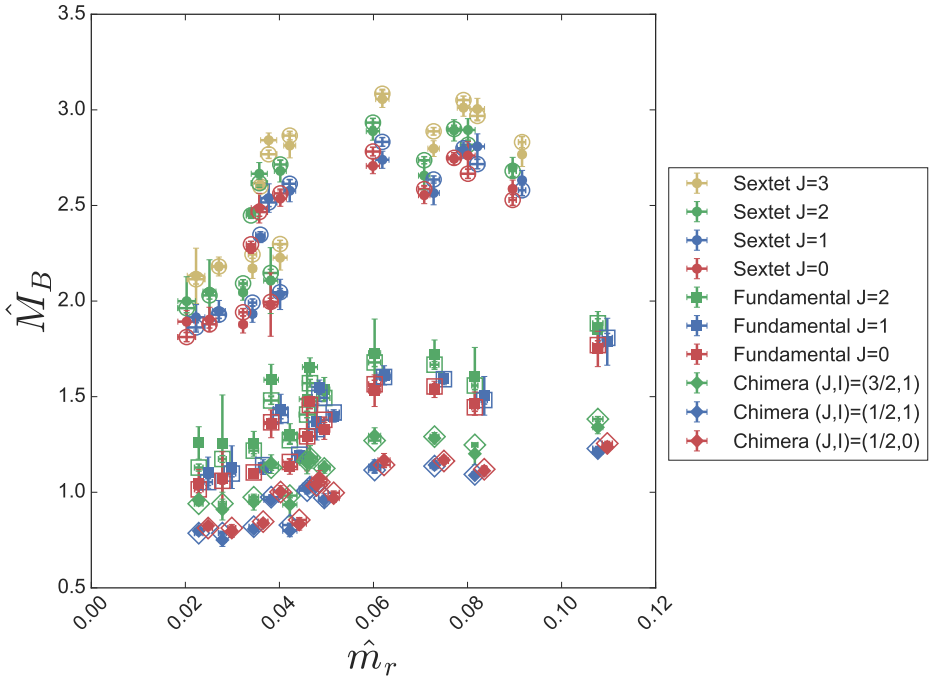

Figure 6.6: Results from the joint correlated fit of all baryon data to Eqs. (6.8), (6.9), and (6.10). The data (solid marker) correspond well to the fit (open marker) at each point. The errors bars of the open markers are those of the fit. The horizontal positions contain small offsets to reduce overlap and aid readability.

jackknife furnishes errors and correlations among the masses. The model used contains 11 free parameters, leaving $120 - 11 = 109$ degrees of freedom. The resulting fit is good, with $\chi^2/\mathrm{DOF} \simeq 93/109 = 0.85$. Figure 6.6 shows the data with the fit overlaid.

Figure 6.7 shows the same fit result after subtracting the lattice artifacts (proportional to $\hat{a}$) from each state. In this figure, the sextet baryons are plotted as functions of $\hat{m}_6$, while the fundamental baryons are plotted as functions of $\hat{m}_4$. Because the masses of the chimera baryons are joint functions of the fermion mass in both representations, they are plotted against the combination $(2C_{44}\hat{m}_4 + C_{66}\hat{m}_6)/6$. The fit formula is linear in this combination. (The factor of 6 is arbitrary and chosen to give the independent variable a similar range to $\hat{m}_4$ and $\hat{m}_6$.) The underlying linear behavior for all the baryons is now clearly visible.

In general, one expects the masses of the single-representation baryons to depend predominantly on the mass of the valence fermions in the same representation and only weakly on the sea

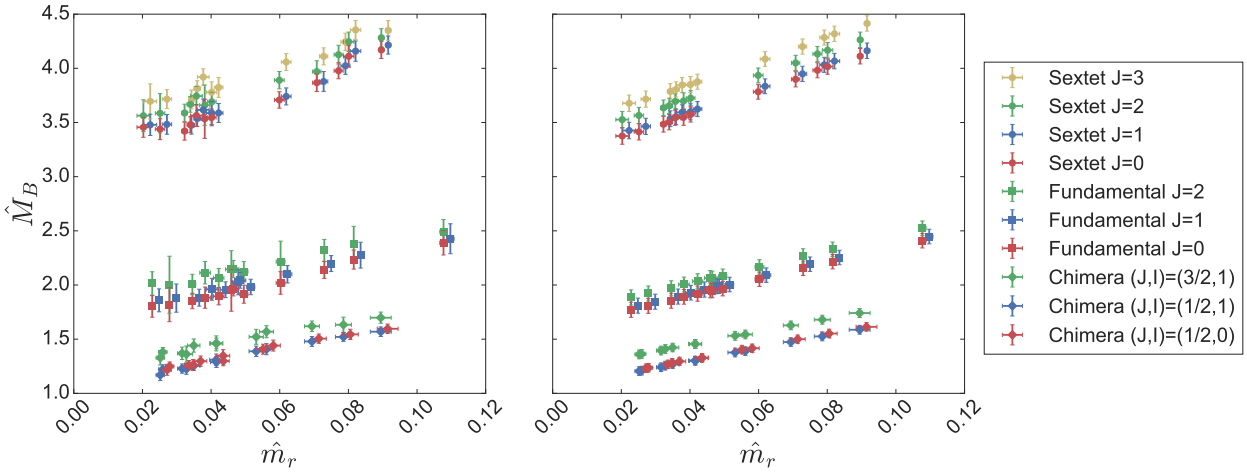

Figure 6.7: Results from the joint correlated fit of all baryon data to Eqs. (6.8)–(6.10). The left pane shows continuum masses obtained by subtracting the lattice artifact from the data. The right pane shows the corresponding fit, with the lattice artifact term removed. The horizontal positions contain small offsets to reduce overlap and aid readability.

fermions in the other representation. The analogy in QCD is the mass of the proton, which also receives virtual contributions from strange quarks. The fact that our models produce a good fit while neglecting these effects suggests that they are small, although we expect their existence as a matter of principle. Repeating the fits including sea dependence did not produce any important changes in the results.

As a preliminary estimate of finite-volume effects, we repeated the above fitting analysis keeping only ensembles with $M_P L > (4.25, 4.5, 4.75, 5.0)$. All qualitative features of the spectrum—the ordering, the rotor splitting, and general placement of the states—were stable against these variations. Quantitatively, the fit parameters were unchanged at the level of roughly one standard deviation. Because the focus of the present analysis of baryons is largely qualitative in nature, we leave a more systematic study of these effects for future work.

6.7 Physical Limits

The fit results of the previous section are most interesting in two limits: the $\hat{m}_6 \to 0$ chiral limit and the double limit $\hat{m}_4, \hat{m}_6 \to 0$. The former limit is important in Ferretti's model, where

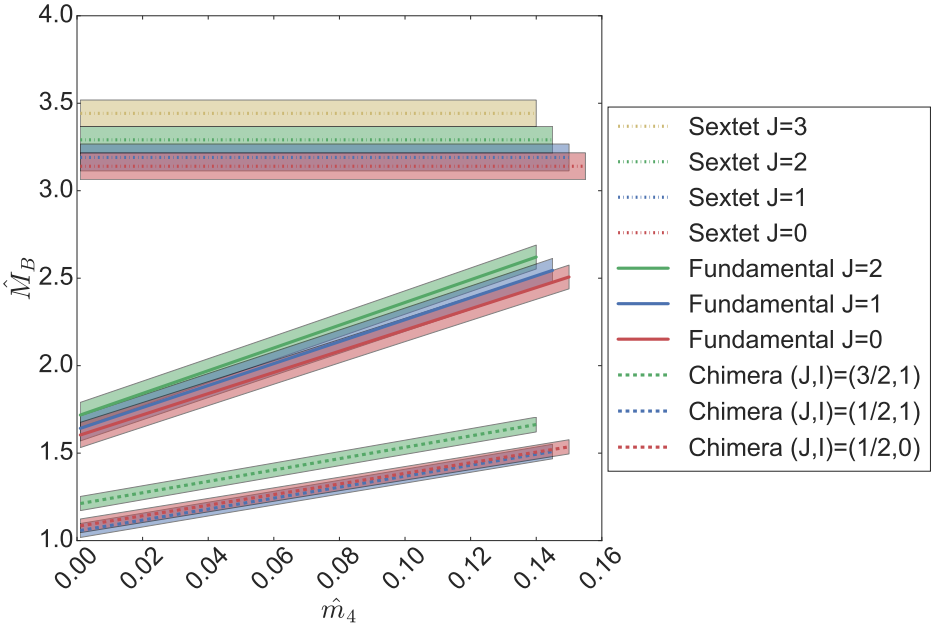

Figure 6.8: The baryon spectrum in the $\hat{m}_6 \to 0$ limit.

the Higgs boson arises (before perturbative coupling to the Standard Model) as an exactly massless sextet Goldstone boson. Figure 6.8 shows the baryon spectrum in the $\hat{m}_6 \to 0$ limit, displayed as a function of the fundamental fermion mass. By construction, the masses of the sextet baryons are independent of $\hat{m}_4$. Likewise, the masses of fundamental and chimera baryons are linear in the fundamental fermion mass. The lightest baryons in the spectrum are the nearly-degenerate $J = 1/2$ chimera baryons, the analogues of the Σ and Λ in QCD. Regarding these two states, it is interesting to note that we observe an inverted multiplet $M_\Lambda \gtrsim M_\Sigma$ with respect to the ordering in QCD, where $M_\Sigma > M_\Lambda$. This ordering is present in the raw lattice data on all the ensembles we considered. Using a non-relativistic quark model as a guide, one would also expect this inversion to occur in QCD if the strange quark were lighter than the up and down quarks.

The spectrum in the double chiral limit ($\hat{m}_4, \hat{m}_6 \to 0$) corresponds to the vertical axis in Fig. 6.8. For convenience, Table 6.2 also records numerical values for the spectrum in the double chiral limit, both in units of the gradient-flow scale $\sqrt{t_0}$ and in units of the sextet pseudoscalar decay constant, which we determined in our previous study of the meson spectrum.

	$M_B\sqrt{t_0}$	M_B/F_6
Fundamental vector meson	0.74(3)	4.2(3)
Sextet vector meson	0.80(3)	4.6(3)
Chimera $(J, I) = (1/2, 0)$	1.08(4)	6.4(4)
Chimera $(J, I) = (1/2, 1)$	1.05(4)	6.2(4)
Chimera $(J, I) = (3/2, 1)$	1.21(4)	7.1(5)
Fundamental $(J = 0)$	1.60(7)	9.4(7)
Fundamental $(J = 1)$	1.63(7)	9.6(7)
Fundamental $(J = 2)$	1.71(7)	10.1(7)
Sextet $(J = 0)$	3.14(8)	18(1)
Sextet $(J = 1)$	3.19(8)	19(1)
Sextet $(J = 2)$	3.29(8)	19(1)
Sextet $(J = 3)$	3.44(8)	20(1)

Table 6.2: The baryon spectrum in the double chiral limit ($\hat{m}_4, \hat{m}_6 \to 0$) in units of the flow scale $\sqrt{t_0}$ and of the sextet pseudoscalar decay constant F_6. For comparison, the masses of the fundamental and sextet vector mesons in this limit are also included. Mesonic quantities were determined in [10].

6.8 Scalar Matrix Elements

We can repurpose our calculations of the mass dependence of the baryons to extract the scalar matrix element $\langle B| \bar{\psi}\psi |B\rangle$ using the Feynman-Hellmann theorem [101]. In the context of composite dark matter models, this matrix element determines the coupling of the Higgs boson to the dark matter and is thus required to calculate the cross section for dark matter direct detection. (For a review of composite dark matter models, see Ref. [108].) Following Ref. [8], we define the quantity f_r^B for the lowest-lying baryon in each representation r:

$$f_r^B \equiv \frac{\hat{m}_r}{\hat{M}_r}\frac{\partial \hat{M}_r}{\partial \hat{m}_r} = \frac{m_r}{M_r}\langle B| \bar{\psi}\psi |B\rangle , \tag{6.20}$$

The dimensionless factor $\hat{m}_r/\hat{M}_r$ serves to cancel the dependence on the renormalization prescription of $\bar{\psi}\psi$ in this expression. We expect f_r^B to be equal to zero in the chiral limit, and to approach unity in the heavy fermion ($\hat{m}_r \to \infty$) limit.

Figure 6.9 shows our results for f_r^B in the fundamental and sextet representations, displayed as functions of the pseudoscalar-to-vector mass ratios on each ensemble. Only the values for the lightest state in each representation are shown; the heavier states are similar. We note that, in the

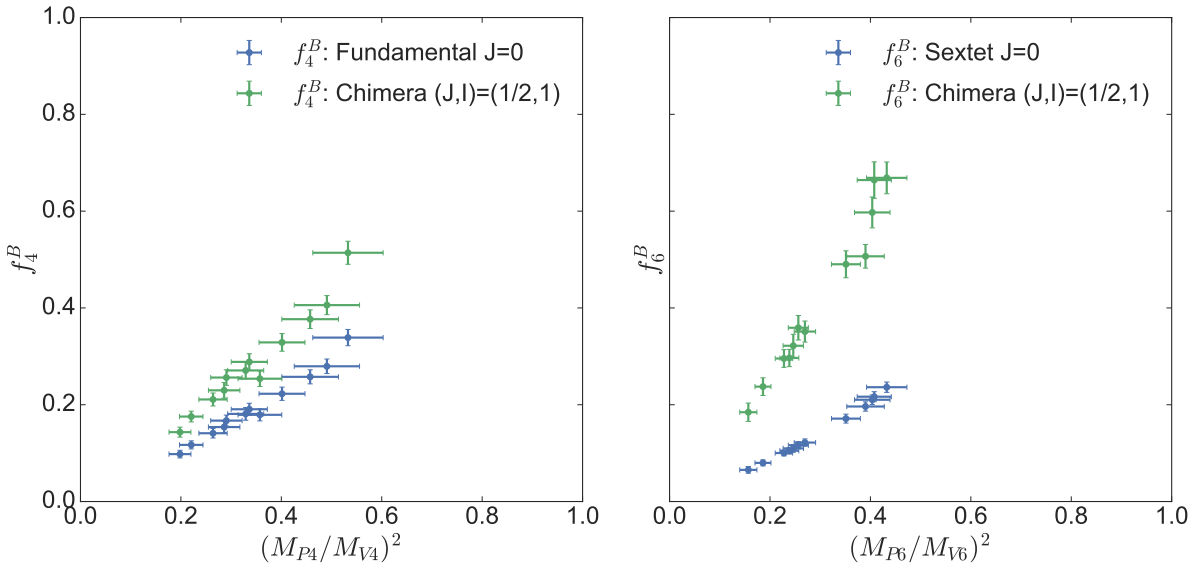

Figure 6.9: Baryon matrix elements of the scalar density, defined via Eq. (6.20). Only the lightest state in each representation is shown; the heavier states are similar. The mesonic quantities were determined in [10].

Ferretti model, none of these baryon states plays the role of a dark matter candidate because of the precise Standard Model charge assignments of the model. However, it is interesting that the values for f_r^B for the fundamental and sextet baryons resemble results seen previously in a number of different gauge theories (in particular, see Fig. 4 of Ref. [57]). The values of both rescaled matrix elements for the chimera baryon come out significantly larger.

6.9 Summary of Baryon Results

This chapter has described the baryon spectrum of SU(4) gauge theory coupled to dynamical fermions in the **4** and **6** representations. The baryon spectrum of this theory contains three classes of baryons with differing valence fermion content: fundamental-only baryons, sextet-only baryons, and mixed-representation baryons. Our analysis began by considering raw lattice results for the baryon masses to motivate a joint model based on large-N_c counting. The important features of this model—a $J(J+1)$ rotor behavior for splittings and shared set of constituent masses for

fermions—were clearly visible even before fitting. The resulting fit was successful and identified a significant lattice artifact proportional to the lattice spacing in each baryon multiplet.

After removing the lattice artifact, the baryon mass data show linear dependence on the fermion mass. Presumably, a more careful analysis in the spirit of heavy baryon chiral perturbation theory [98, 26] would predict non-analytic behavior similar to that of QCD. The precision of our data does not allow us to test these predictions. Observing this behavior in QCD is notoriously difficult, requiring very light fermions.

In Ferretti's model, the Standard Model top quark mixes linearly with the analogue of the Λ. This happens because the fundamental fermions carry $\mathrm{SU}(3) \times \mathrm{SU}(3)' \supset \mathrm{SU}(3)_c$ flavor quantum numbers and transform as a $\bar{\mathbf{3}}$, while sextet fermions are uncharged under $\mathrm{SU}(3)_c$. The fundamental fermions within the top partner are contracted anti-symmetrically to form a $\mathbf{3}$ of $\mathrm{SU}(3)_c$. Discarding one of the three fundamental fermions as we did in this paper, we obtain a qq state, still anti-symmetrized on its flavor index and hence an isospin singlet. Because the qq state is antisymmetric on both its SU(4)-color and flavor indices, the spins must couple anti-symmetrically as well into a $J_{qq} = 0$ state. Thus, the top partner is the analogue of the Λ hyperon in QCD.

The phenomenology of composite Higgs completions of the Standard Model is commonly presented in terms of a ratio $\xi = v^2/F^2$ where v is the Higgs vacuum expectation value (246 GeV), and F is the relevant pseudoscalar decay constant. In the Ferretti model, $F = F_6/\sqrt{2}$ where F_6 is the decay constant of the sextet Goldstone bosons. (The factor of $\sqrt{2}$ is due to our normalization convention, which corresponds to $F_\pi \simeq 130$ MeV in QCD.) In the absence of a direct detection of new resonances, a discovery of new physics can come through a deviation of some observable from its Standard Model value, which would point to a value of ξ and hence of F_6. That would set the scale for other hadronic observables in the new physics sector.

Table 6.2 gives the spectrum of light hadrons in our system in units of F_6, and Fig. 6.10 shows the baryon and meson masses in the $m_6 \to 0$ limit as a function of the ratio $(M_{P4}/F_6)^2$. The mass ratio of Qqq baryons to vector mesons is quite similar to what is seen in QCD. The ratios of all masses to F_6 are smaller than in QCD, but that is something we have seen before, and is

broadly consistent with large-N_c expectations.

Current experimental evidence suggests that $\xi \lesssim 0.1$ [22, 121, 1], which means that the scale of the new strong sector is roughly $F_6 \gtrsim \sqrt{2}v/\sqrt{0.1} \simeq 1.1$ TeV in our normalization. Figure 6.10 then shows that the mass of the Λ analogue—the top partner in Ferretti's model—must be $M_\Lambda \gtrsim 6.5$ TeV. This estimate for the mass of the top partner will be modified by perturbative corrections from interactions with the Standard Model. We expect these corrections to be small, just as perturbative electromagnetic corrections to hadron masses are small in QCD. We note that the present analysis has not attempted a detailed budgeting of systematic effects from the lattice computation itself. Such effects include, of course, the slightly different fermion content of the model we studied in comparison with the Ferretti model.

Although our results for the chimera mass indicate that it is somewhat heavier than assumed in Ref. [75], it remains to be seen whether this leads to any significant phenomenological tension or fine-tuning requirement. The most crucial role of the top partner is in the generation of a realistic potential for the Higgs boson; we plan to investigate the top contribution to the Higgs potential non-perturbatively in a future work. We are also planning a follow-up study of the decay matrix elements of the chimera baryon, which will allow the calculation of its decay width; experimental bounds on the top-partner mass typically assume a narrow width, and could be significantly weaker for a wide resonance.

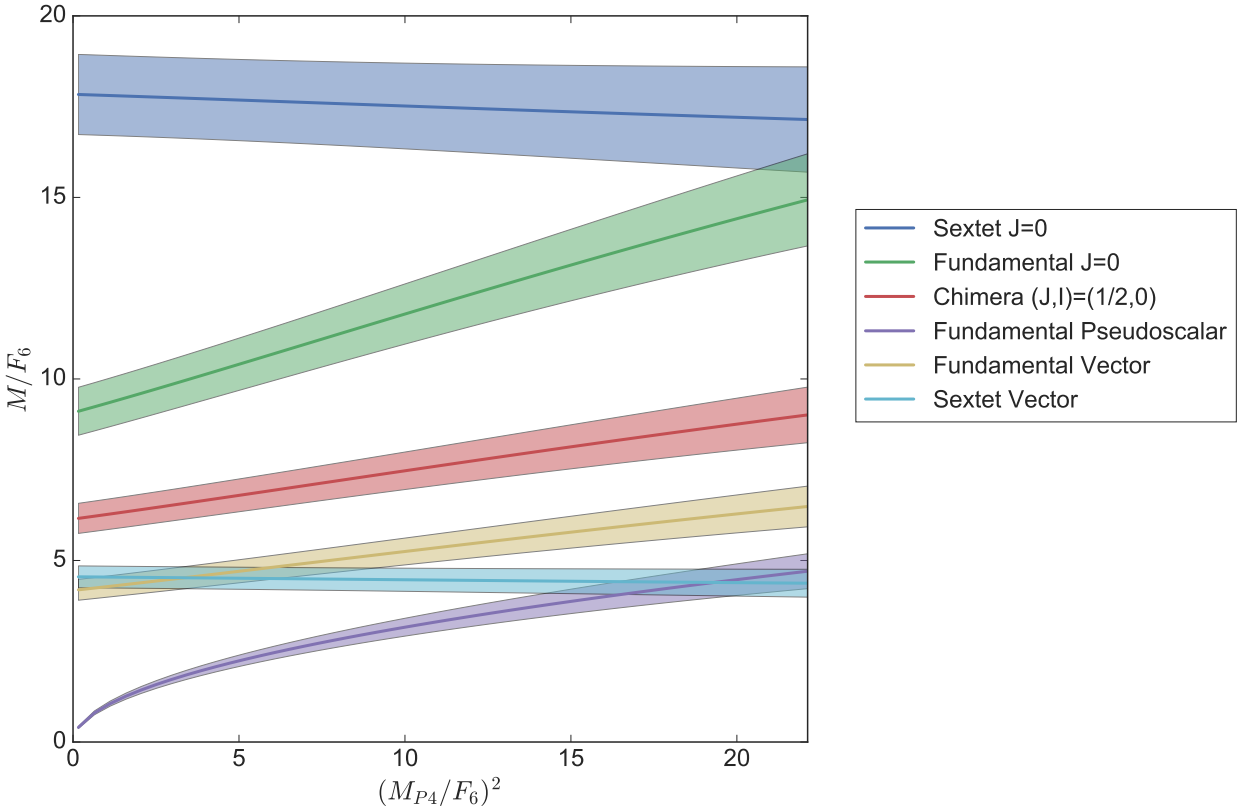

Figure 6.10: Baryon and meson masses in the $m_6 \to 0$ limit. The chimera $(J, I) = (1/2, 0)$ state corresponds to the top partner of Ferretti's model. The small rise of the sextet quantities in this limit is due to the mild variation of $\hat{F}_6$ with the fundamental fermion mass. Mesonic quantities were determined in [10].

Chapter 7

Conclusions and Outlook

This thesis has described lattice simulations of SU(4) gauge theory coupled to fermions in multiple representations, the fundamental **4** and two-index antisymmetric **6**. These "multirep" simulations are the first of their kind to include the dynamics of multiple representations of fermions (in four spacetime dimensions and without any notion of supersymmetry). The motivation for studying this particular theory is twofold.

The first motivation is a theory of physics beyond the Standard Model which was recently proposed in the literature. In this model, the Higgs boson is a composite particle, and the top quark is a partially composite particle. To this end, we calculated the low-lying particle spectrum of the theory, including both mesons and baryons. The main results are summarized neatly in Figure 6.10, which displays a partial list of the new particle spectrum predicted in this multirep model. As explained in Sec. 6.9, current experimental evidence constrains the new compositeness scale to be roughly 1.1 TeV. Figure 6.10 therefore shows that the mass of the top partner must be $M_\Lambda \gtrsim 6.5$ TeV. In principle, all of these particles are potential targets for existing and future direct-detection experiments.

Second, theories of this sort represent a new direction in the study of gauge dynamics and thus provide opportunities to test our understanding of strongly coupled physics. The main result is that the spectrum of the theory is QCD-like. More precisely, a generalized quark model captures the qualitative features of the spectrum, e.g., the ordering and placement of states. Quantitatively, NLO chiral perturbation theory and a large-N_c model reproduce the results for the meson and

baryon states, respectively. The malice of hindsight makes these results seem inevitable. However, strongly coupled QFTs remain poorly understood, and these results may hint at an important lesson for model builders: the spectrum of QCD—in terms of the quark model, large-N_c, and chiral perturbation theory—is surprisingly generic. Engineering a qualitatively novel spectrum likely requires new ingredients (e.g., near-conformal dynamics).

Looking ahead, many avenues exist for future work. We shall mention two such possibilities. First, it remains interesting to determine the low-energy constants associated with the Higgs potential of Eq. (1.35). These constants determine whether electroweak symmetry breaking occurs. They also furnish a theoretically preferred value for ξ, according to Eq. (1.37), which must otherwise be inferred from experiment as an independent parameter. In other words, precise knowledge of these low-energy constants would greatly improve the predictability of this and similar theories. Measuring their values is the subject of ongoing work (see [67] for some preliminary efforts). Second, our knowledge of the anomalous dimensions of baryon operators remains incomplete. Perturbative results suggest that the anomalous dimensions remain small, certainly below the desired neighborhood of $\gamma \sim 2$ [64]. However, surprises could exists beyond perturbation theory. For enthusiasts of partial compositeness, the lack of rigorous obstructions together with promising results from holographic models would make it interesting to check.

Bibliography

[1] G. Aad et al. Constraints on new phenomena via Higgs boson couplings and invisible decays with the ATLAS detector. JHEP, 11:206, 2015.

[2] G.S. Adkins, C.R. Nappi, and E. Witten. Static Properties of Nucleons in the Skyrme Model. Nucl. Phys., B228:552, 1983.

[3] S.L. Adler. Axial vector vertex in spinor electrodynamics. Phys. Rev., 177:2426–2438, 1969.

[4] T. Alanne, N. Bizot, G. Cacciapaglia, and F. Sannino. Classification of NLO operators for composite-Higgs models. arXiv:1801.05444.

[5] S. Aoki. Chiral perturbation theory with Wilson type fermions including a^2 effects: N(f) = 2 degenerate case. Phys. Rev., D68:054508, 2003.

[6] S. Aoki, O. Bär, and S.R. Sharpe. Vector and Axial Currents in Wilson Chiral Perturbation Theory. Phys. Rev., D80:014506, 2009.

[7] S. Aoki, H. Fukaya, S. Hashimoto, and T. Onogi. Finite volume QCD at fixed topological charge. Phys. Rev., D76:054508, 2007.

[8] T. Appelquist et al. Composite bosonic baryon dark matter on the lattice: SU(4) baryon spectrum and the effective Higgs interaction. Phys. Rev., D89(9):094508, 2014.

[9] R. Arthur, V. Drach, M. Hansen, A. Hietanen, C. Pica, and F. Sannino. SU(2) gauge theory with two fundamental flavors: A minimal template for model building. Phys. Rev., D94(9):094507, 2016.

[10] V. Ayyar, T. DeGrand, M. Golterman, D.C. Hackett, W.I. Jay, E.T. Neil, Y. Shamir, and B. Svetitsky. Spectroscopy of SU(4) composite Higgs theory with two distinct fermion representations. arXiv:1710.00806.

[11] V. Ayyar, T. DeGrand, D.C. Hackett, W.I. Jay, E.T. Neil, Y. Shamir, and B. Svetitsky. Finite-temperature phase structure of SU(4) gauge theory with multiple fermion representations. arXiv:1802.09644.

[12] V. Ayyar, T. DeGrand, D.C. Hackett, W.I. Jay, E.T. Neil, Y. Shamir, and B. Svetitsky. Chiral Transition of SU(4) Gauge Theory with Fermions in Multiple Representations. In Proceedings of the 35th International Symposium on Lattice Field Theory, arXiv:1709.06190.

[13] V. Ayyar, T. DeGrand, D.C. Hackett, W.I. Jay, E.T. Neil, Y. Shamir, and B. Svetitsky. Baryon spectrum of SU(4) composite Higgs theory with two distinct fermion representations. arXiv:1801.05809.

[14] V. Ayyar, D. Hackett, W. Jay, and E. Neil. Confinement study of an SU(4) gauge theory with fermions in multiple representations. In Proceedings of the 35th International Symposium on Lattice Field Theory, arXiv:1710.03257.

[15] G.S. Bali, F. Bursa, L. Castagnini, S. Collins, L. Del Debbio, B. Lucini, and M. Panero. Mesons in large-N QCD. JHEP, 06:071, 2013.

[16] O. Bär and M. Golterman. Chiral perturbation theory for gradient flow observables. Phys. Rev., D89(3):034505, 2014. [Erratum: Phys. Rev. D89, 099905 (2014)].

[17] O. Bär, G. Rupak, and N. Shoresh. Chiral perturbation theory at $O(a^2)$ for lattice QCD. Phys. Rev., D70:034508, 2004.

[18] J. Barnard, T. Gherghetta, and T.S. Ray. UV descriptions of composite Higgs models without elementary scalars. JHEP, 02:002, 2014.

[19] A. Bazavov et al. Nonperturbative QCD Simulations with 2+1 Flavors of Improved Staggered Quarks. Rev. Mod. Phys., 82:1349–1417, 2010.

[20] A. Bazavov et al. Gradient flow and scale setting on MILC HISQ ensembles. Phys. Rev., D93(9):094510, 2016.

[21] J. S. Bell and R. Jackiw. A PCAC puzzle: $\pi_0 \to \gamma\gamma$ in the sigma model. Nuovo Cim., A60:47–61, 1969.

[22] B. Bellazzini, C. Csáki, and J. Serra. Composite Higgses. Eur. Phys. J., C74(5):2766, 2014.

[23] A. Belyaev, G Cacciapaglia, H. Cai, G. Ferretti, T. Flacke, A. Parolini, and H. Serodio. Di-boson signatures as Standard Candles for Partial Compositeness. JHEP, 01:094, 2017.

[24] E. Bennett, D.K Hong, J. Lee, C.D. Lin, B. Lucini, M. Piai, and D. Vadacchino. Sp(4) gauge theory on the lattice: towards SU(4)/Sp(4) composite Higgs (and beyond). arXiv:1712.04220.

[25] C.W. Bernard and T.A. DeGrand. Perturbation theory for fat link fermion actions. Nucl. Phys. Proc. Suppl., 83:845–847, 2000.

[26] V. Bernard. Chiral Perturbation Theory and Baryon Properties. Prog. Part. Nucl. Phys., 60:82–160, 2008.

[27] J. Bijnens, P. Gosdzinsky, and P. Talavera. Vector meson masses in chiral perturbation theory. Nucl. Phys., B501:495–517, 1997.

[28] J. Bijnens, P. Gosdzinsky, and P. Talavera. Chiral corrections to vector meson decay constants. Phys. Lett., B429:111–120, 1998.

[29] J. Bijnens and J. Lu. Technicolor and other QCD-like theories at next-to-next-to-leading order. JHEP, 11:116, 2009.

[30] K.M. Bitar et al. Hadron spectrum in QCD at $6/g^2 = 5.6$. Phys. Rev., D42:3794–3818, 1990.

[31] S. Bolognesi. Baryons and Skyrmions in QCD with Quarks in Higher Representations. Phys. Rev., D75:065030, 2007.

[32] R. Brower, S. Chandrasekharan, J.W. Negele, and U. J. Wiese. QCD at fixed topology. Phys. Lett., B560:64–74, 2003.

[33] M. Bruno, T. Korzec, and S. Schaefer. Setting the scale for the CLS $2 + 1$ flavor ensembles. Phys. Rev., D95(7):074504, 2017.

[34] R. Budìnek. Non-supersymmetric extensions of the standard model of electroweak interactions. Master's thesis, Charles University in Prague, 2004.

[35] F. Buisseret, N. Matagne, and C. Semay. Spin contribution to light baryons in different large-N limits. Phys. Rev., D85:036010, 2012.

[36] G. Cacciapaglia and F. Sannino. Fundamental Composite (Goldstone) Higgs Dynamics. JHEP, 04:111, 2014.

[37] W.B. Cairncross, D.N. Gresh, M. Grau, K.C. Cossel, T.S. Roussy, Y. Ni, Y. Zhou, J. Ye, and E.A. Cornell. Precision Measurement of the Electrons Electric Dipole Moment Using Trapped Molecular Ions. Phys. Rev. Lett., 119(15):153001, 2017.

[38] C.G. Callan, Jr., S.R. Coleman, J. Wess, and B. Zumino. Structure of phenomenological Lagrangians. 2. Phys. Rev., 177:2247–2250, 1969.

[39] A. Calle Cordón, T. DeGrand, and J. L. Goity. N_c dependencies of baryon masses: Analysis with lattice QCD and effective theory. Phys. Rev., D90(1):014505, 2014.

[40] M. Cè, M. García Vera, L. Giusti, and S. Schaefer. The topological susceptibility in the large-N limit of SU(N) Yang-Mills theory. Phys. Lett., B762:232–236, 2016.

[41] A. Cherman, T.D. Cohen, and R.F. Lebed. All you need is N: Baryon spectroscopy in two large N limits. Phys. Rev., D80:036002, 2009.

[42] T.D. Cohen, D.L. Shafer, and R.F. Lebed. Baryons in QCD(AS) at Large $N(c)$: A Roundabout Approach. Phys. Rev., D81:036006, 2010.

[43] S.R. Coleman, J. Wess, and B. Zumino. Structure of phenomenological Lagrangians. 1. Phys. Rev., 177:2239–2247, 1969.

[44] R. Contino. The Higgs as a Composite Nambu-Goldstone Boson. In Physics of the large and the small, TASI 2009, proceedings of the Theoretical Advanced Study Institute in Elementary Particle Physics, Boulder, Colorado, USA, 1-26 June 2009, pages 235–306, 2011.

[45] R. Contino and A. Pomarol. Holography for fermions. JHEP, 11:058, 2004.

[46] C. Csáki and P. Tanedo. Beyond the Standard Model. In Proceedings, 2013 European School of High-Energy Physics (ESHEP 2013): Paradfurdo, Hungary, June 5-18, 2013, pages 169–268, 2015.

[47] P. Cvitanović. Group theory for Feynman diagrams in non-Abelian gauge theories. Phys. Rev., D14:1536–1553, 1976.

[48] Predrag Cvitanović. Group theory: Birdtracks, Lie's and exceptional groups. Princeton, USA: Univ. Pr., 2008.

[49] J. Dai, R.F. Dashen, E.E. Jenkins, and A.V. Manohar. Flavor symmetry breaking in the 1/N(c) expansion. Phys. Rev., D53:273–282, 1996.

[50] R.F. Dashen, E.E. Jenkins, and A.V. Manohar. The $1/N(c)$ expansion for baryons. Phys. Rev., D49:4713, 1994. [Erratum: Phys. Rev.D51,2489(1995)].

[51] R.F. Dashen, E.E. Jenkins, and A.V. Manohar. Spin flavor structure of large $N(c)$ baryons. Phys. Rev., D51:3697–3727, 1995.

[52] R.F. Dashen and A.V. Manohar. Baryon - pion couplings from large N(c) QCD. Phys. Lett., B315:425–430, 1993.

[53] A. De Rujula, H. Georgi, and S. L. Glashow. Hadron Masses in a Gauge Theory. Phys. Rev., D12:147–162, 1975.

[54] A. De Simone, O. Matsedonskyi, R. Rattazzi, and A. Wulzer. A First Top Partner Hunter's Guide. JHEP, 04:004, 2013.

[55] T. DeGrand. Lattice baryons in the 1/N expansion. Phys. Rev., D86:034508, 2012.

[56] T. DeGrand. Lattice calculations of the spectroscopy of baryons with broken flavor SU(3) symmetry and 3, 5, or 7 colors. Phys. Rev., D89(1):014506, 2014.

[57] T. DeGrand. Lattice tests of beyond Standard Model dynamics. Rev. Mod. Phys., 88:015001, 2016.

[58] T. DeGrand. Simple chromatic properties of gradient flow. Phys. Rev., D95(11):114512, 2017.

[59] T. DeGrand and C.E. Detar. Lattice methods for quantum chromodynamics. New Jersey, USA: World Scientific (2006) 345 p, 2006.

[60] T. DeGrand, M. Golterman, E.T. Neil, and Y. Shamir. One-loop Chiral Perturbation Theory with two fermion representations. Phys. Rev., D94(2):025020, 2016.

[61] T. DeGrand and Y. Liu. Lattice study of large N_c QCD. Phys. Rev., D94(3):034506, 2016. [Erratum: Phys. Rev. D95, 019902 (2017)].

[62] T. DeGrand, Y. Liu, E.T. Neil, Y. Shamir, and B. Svetitsky. Spectroscopy of SU(4) gauge theory with two flavors of sextet fermions. Phys. Rev., D91:114502, 2015.

[63] T. DeGrand and S. Schaefer. Topological susceptibility in two-flavor QCD. arXiv:0712.2914.

[64] T. DeGrand and Y. Shamir. One-loop anomalous dimension of top-partner hyperbaryons in a family of composite Higgs models. Phys. Rev., D92(7):075039, 2015.

[65] T. DeGrand, Y. Shamir, and B. Svetitsky. Suppressing dislocations in normalized hypercubic smearing. Phys. Rev., D90(5):054501, 2014.

[66] T.A. DeGrand. One loop matching coefficients for a variant overlap action: And some of its simpler relatives. Phys. Rev., D67:014507, 2003.

[67] T.A. DeGrand, M. Golterman, W.I. Jay, E.T. Neil, Y. Shamir, and B. Svetitsky. Radiative contribution to the effective potential in composite Higgs models from lattice gauge theory. Phys. Rev., D94(5):054501, 2016.

[68] T.A. DeGrand, D. Hackett, W.I. Jay, E.T. Neil, Y. Shamir, and B. Svetitsky. Towards Partial Compositeness on the Lattice: Baryons with Fermions in Multiple Representations. Proceedings of Science, LATTICE2016:219, arXiv:1610.06465.

[69] T.A. DeGrand, A. Hasenfratz, and T.G. Kovacs. Improving the chiral properties of lattice fermions. Phys. Rev., D67:054501, 2003.

[70] L. Del Debbio, C. Englert, and R. Zwicky. A UV Complete Compositeness Scenario: LHC Constraints Meet The Lattice. JHEP, 08:142, 2017.

[71] L. Demortier and L. Lyons. Everything you always wanted to know about pulls. CDF/ANAL/PUBLIC/5776. Version 3.00. April 8, 2008.

[72] J. F. Donoghue, E. Golowich, and Barry R. Holstein. Dynamics of the standard model. Camb. Monogr. Part. Phys. Nucl. Phys. Cosmol., 2:1–540, 1992. [Camb. Monogr. Part. Phys. Nucl. Phys. Cosmol.35(2014)].

[73] S. Duane, A. D. Kennedy, B. J. Pendleton, and D. Roweth. Hybrid Monte Carlo. Phys. Lett., B195:216–222, 1987.

[74] M.J. Dugan, H. Georgi, and D.B. Kaplan. Anatomy of a Composite Higgs Model. Nucl. Phys., B254:299–326, 1985.

[75] G. Ferretti. UV Completions of Partial Compositeness: The Case for a SU(4) Gauge Group. JHEP, 06:142, 2014.

[76] G. Ferretti. Gauge theories of Partial Compositeness: Scenarios for Run-II of the LHC. JHEP, 06:107, 2016.

[77] G. Ferretti and D. Karateev. Fermionic UV completions of Composite Higgs models. JHEP, 03:077, 2014.

[78] Kazuo Fujikawa. On the Evaluation of Chiral Anomaly in Gauge Theories with Gamma(5) Couplings. Phys. Rev., D29:285, 1984.

[79] J. Galloway, J.A. Evans, M.A. Luty, and R.A. Tacchi. Minimal Conformal Technicolor and Precision Electroweak Tests. JHEP, 10:086, 2010.

[80] J. Gasser and H. Leutwyler. Chiral Perturbation Theory to One Loop. Annals Phys., 158:142, 1984.

[81] J. Gasser and H. Leutwyler. Light Quarks at Low Temperatures. Phys. Lett., B184:83–88, 1987.

[82] C. Gattringer and C.B. Lang. Quantum chromodynamics on the lattice. Lect. Notes Phys., 788:1–343, 2010.

[83] H. Georgi and D.B. Kaplan. Composite Higgs and Custodial SU(2). Phys. Lett., 145B:216–220, 1984.

[84] J. Gervais and B. Sakita. Large n Baryonic Soliton and Quarks. Phys. Rev., D30:1795, 1984.

[85] J. Gervais and B. Sakita. Large N QCD Baryon Dynamics: Exact Results from Its Relation to the Static Strong Coupling Theory. Phys. Rev. Lett., 52:87, 1984.

[86] M. Golterman. Applications of chiral perturbation theory to lattice QCD. In Modern perspectives in lattice QCD: Quantum field theory and high performance computing. Proceedings, International School, 93rd Session, Les Houches, France, August 3-28, 2009, pages 423–515, 2009.

[87] M. Golterman and Y. Shamir. Top quark induced effective potential in a composite Higgs model. Phys. Rev., D91(9):094506, 2015.

[88] M. Golterman and Y. Shamir. Effective potential in ultraviolet completions for composite Higgs models. arXiv:1707.06033.

[89] S.A. Gottlieb, W. Liu, D. Toussaint, R. L. Renken, and R. L. Sugar. Hybrid Molecular Dynamics Algorithms for the Numerical Simulation of Quantum Chromodynamics. Phys. Rev., D35:2531–2542, 1987.

[90] D.C. Hackett. Stability Analysis of the Chiral Transition in SU(4) Gauge Theory with Fermions in Multiple Representations. arXiv:1712.01959.

[91] A. Hasenfratz, R. Hoffmann, and S. Schaefer. Hypercubic smeared links for dynamical fermions. JHEP, 05:029, 2007.

[92] A. Hasenfratz and F. Knechtli. Flavor symmetry and the static potential with hypercubic blocking. Phys. Rev., D64:034504, 2001.

[93] A. Hasenfratz, Z. Kunszt, P. Hasenfratz, and C. B. Lang. Hopping Parameter Expansion for the Meson Spectrum in SU(3) Lattice QCD. Phys. Lett., 110B:289, 1982.

[94] A. Hasenfratz, Y. Liu, and C.Y. Huang. The renormalization group step scaling function of the 2-flavor SU(3) sextet model. arXiv:1507.08260.

[95] R.J. Hudspith. private communication.

[96] E.E. Jenkins. Baryon hyperfine mass splittings in large N QCD. Phys. Lett., B315:441–446, 1993.

[97] E.E. Jenkins and R.F. Lebed. Baryon mass splittings in the 1/N(c) expansion. Phys. Rev., D52:282–294, 1995.

[98] E.E. Jenkins and A.V. Manohar. Baryon chiral perturbation theory using a heavy fermion Lagrangian. Phys. Lett., B255:558–562, 1991.

[99] E.E. Jenkins, A.V. Manohar, J.W. Negele, and A. Walker-Loud. A Lattice Test of 1/N(c) Baryon Mass Relations. Phys. Rev., D81:014502, 2010.

[100] R. C. Johnson. Simple derivation of the ksrf relation. Nucl. Phys., B23:247–252, 1970.

[101] P. Junnarkar and A. Walker-Loud. Scalar strange content of the nucleon from lattice QCD. Phys. Rev., D87:114510, 2013.

[102] D.B. Kaplan. Flavor at SSC energies: A New mechanism for dynamically generated fermion masses. Nucl. Phys., B365:259–278, 1991.

[103] F. Karsch and M. Lütgemeier. Deconfinement and chiral symmetry restoration in an SU(3) gauge theory with adjoint fermions. Nucl. Phys., B550:449–464, 1999.

[104] K. Kawarabayashi and M. Suzuki. Partially conserved axial vector current and the decays of vector mesons. Phys. Rev. Lett., 16:255, 1966.

[105] F. Knechtli, M. Günther, and M. Peardon. Lattice Quantum Chromodynamics: Practical Essentials. Springer Briefs in Physics. Springer, 2017.

[106] J.B. Kogut, J. Shigemitsu, and D.K. Sinclair. Chiral Symmetry Breaking With Octet and Sextet Quarks. Phys. Lett., B145:239–242, 1984.

[107] J.B. Kogut, M. Stone, H.W. Wyld, J. Shigemitsu, S.H. Shenker, and D.K. Sinclair. The Scales of Chiral Symmetry Breaking in Quantum Chromodynamics. Phys. Rev. Lett., 48:1140, 1982.

[108] G.D. Kribs and E.T. Neil. Review of strongly-coupled composite dark matter models and lattice simulations. Int. J. Mod. Phys., A31(22):1643004, 2016.

[109] D.B. Leinweber, W. Melnitchouk, D.G. Richards, A.G. Williams, and J.M. Zanotti. Baryon spectroscopy in lattice QCD. Lect. Notes Phys., 663:71–112, 2005.

[110] G.P. Lepage and C. Gohlke. gplepage/lsqfit: lsqfit version 9.1.3, April 2017.

[111] G.P. Lepage and D.C. Hackett. gplepage/gvar: gvar version 8.3.2, June 2017.

[112] G.P. Lepage and P.B. Mackenzie. On the viability of lattice perturbation theory. Phys. Rev., D48:2250–2264, 1993.

[113] K.F. Liu, S.J. Dong, T. Draper, D. Leinweber, J.H. Sloan, W. Wilcox, and R. M. Woloshyn. Valence QCD: Connecting QCD to the quark model. Phys. Rev., D59:112001, 1999.

[114] D.G. Luenberger and Y. Ye. Linear and Nonlinear Programming, Fourth Edition. Springer, 2008.

[115] M. Lüscher. Properties and uses of the Wilson flow in lattice QCD. JHEP, 08:071, 2010. [Erratum: JHEP 03, 092 (2014)].

[116] T. Ma and G. Cacciapaglia. Fundamental Composite 2HDM: SU(N) with 4 flavours. JHEP, 03:211, 2016.

[117] G. Mack. All unitary ray representations of the conformal group SU(2, 2) with positive energy. Commun. Math. Phys., 55:1, 1977.

[118] A.V. Manohar. Large N QCD. In Probing the standard model of particle interactions. Proceedings, Summer School in Theoretical Physics, NATO Advanced Study Institute, 68th session, Les Houches, France, July 28-September 5, 1997. Pt. 1, 2, pages 1091–1169, 1998.

[119] I. Montvay and G. Münster. Quantum fields on a lattice. Cambridge University Press, 1997.

[120] K. A. Olive et al. Review of Particle Physics. Chin. Phys., C38:090001, 2014.

[121] G. Panico and A. Wulzer. The Composite Nambu-Goldstone Higgs. Lect. Notes Phys., 913, 2016.

[122] M.E. Peskin. The Alignment of the Vacuum in Theories of Technicolor. Nucl. Phys., B175:197–233, 1980.

[123] M.E. Peskin and T. Takeuchi. Estimation of oblique electroweak corrections. Phys. Rev., D46:381–409, 1992.

[124] R. Rattazzi. TASI 2015 lectures "Particle phenomenology for string theorists", June 2015.

[125] R. Rattazzi, V.S. Rychkov, E. Tonni, and A. Vichi. Bounding scalar operator dimensions in 4D CFT. JHEP, 12:031, 2008.

[126] Riazuddin and Fayyazuddin. Algebra of current components and decay widths of rho and K^* mesons. Phys. Rev., 147:1071–1073, 1966.

[127] W. Rossman. Lie Groups: An Introduction Through Linear Groups. Oxford Graduate Texts in Mathematics. Oxford, 2002.

[128] G. Rupak and N. Shoresh. Chiral perturbation theory for the Wilson lattice action. Phys. Rev., D66:054503, 2002.

[129] Matthew D. Schwartz. Quantum Field Theory and the Standard Model. Cambridge University Press, 2014.

[130] Y. Shamir, B. Svetitsky, and E. Yurkovsky. Improvement via hypercubic smearing in triplet and sextet QCD. Phys. Rev., D83:097502, 2011.

[131] S.R. Sharpe. Quenched chiral logarithms. Phys. Rev., D46:3146–3168, 1992.

[132] S.R. Sharpe. Applications of Chiral Perturbation theory to lattice QCD. In Workshop on Perspectives in Lattice QCD Nara, Japan, October 31-November 11, 2005, 2006.

[133] S.R. Sharpe and R.L. Singleton, Jr. Spontaneous flavor and parity breaking with Wilson fermions. Phys. Rev., D58:074501, 1998.

[134] S.R. Sharpe and J.M.S. Wu. Twisted mass chiral perturbation theory at next-to-leading order. Phys. Rev., D71:074501, 2005.

[135] B. Sheikholeslami and R. Wohlert. Improved Continuum Limit Lattice Action for QCD with Wilson Fermions. Nucl. Phys., B259:572, 1985.

[136] Y. Shi and R. Shrock. Renormalization-Group Evolution and Nonperturbative Behavior of Chiral Gauge Theories with Fermions in Higher-Dimensional Representations. Phys. Rev., D92(12):125009, 2015.

[137] B. Svetitsky. Looking behind the Standard Model with lattice gauge theory. In Proceedings of the 35th International Symposium on Lattice Field Theory, arXiv:1708.04840.

[138] Gerard 't Hooft. A Planar Diagram Theory for Strong Interactions. Nucl. Phys., B72:461, 1974.

[139] L. Vecchi. A dangerous irrelevant UV-completion of the composite Higgs. JHEP, 02:094, 2017.

[140] Steven Weinberg. Baryon and Lepton Nonconserving Processes. Phys. Rev. Lett., 43:1566–1570, 1979.

[141] P. Weisz. Continuum Limit Improved Lattice Action for Pure Yang-Mills Theory. 1. Nucl. Phys., B212:1–17, 1983.

[142] P. Weisz and R. Wohlert. Continuum Limit Improved Lattice Action for Pure Yang-Mills Theory. 2. Nucl. Phys., B236:397, 1984. [Erratum: Nucl. Phys.B247,544(1984)].

[143] Kenneth G. Wilson. Confinement of Quarks. Phys. Rev., D10:2445–2459, 1974. [,45(1974)].

[144] Kenneth G. Wilson. Quarks and Strings on a Lattice. In New Phenomena in Subnuclear Physics: Proceedings, International School of Subnuclear Physics, Erice, Sicily, Jul 11-Aug 1 1975. Part A, page 99, 1975.

[145] E. Witten. Baryons in the 1/n Expansion. Nucl. Phys., B160:57–115, 1979.

[146] E. Witten. Current Algebra, Baryons, and Quark Confinement. Nucl. Phys., B223:433–444, 1983.

Appendix A

Technical Material

A.1 Lie groups

This appendix collects some useful results about Lie groups. Many of the remarks follow closely a set of (unpublished but widely circulated) notes which I took during a course on group theory under Professor N. Manton during fall 2012 at the University of Cambridge. Even the seemingly more technical statements are elementary results in Lie theory and can be found, e.g., in the text by Rossman [127].

Lie groups. A Lie group G is a smooth manifold which is also a group with smooth group operations. The elements depend continuously on a number of (real) parameters, called the dimension of the group. The group operations—products and inverses—depend continuously and smoothly on the parameters. The most important Lie groups in physics are those of square matrices. These are called linear Lie groups, as the matrices act linearly on vectors in a vector space. The group operation in matrix Lie groups is always multiplication. Although addition is a sensible matrix operation, it is not the group operation. The identity in a matrix Lie group is always the unit matrix, and the inverse of an element is the inverse matrix. Matrix multiplication is automatically associative, provided the matrix elements multiply associatively.

Lie algebras. The Lie algebra $\mathfrak{g}$ of a Lie group G is the tangent space to G at the identity $I \in G$. One studies the tangent space by differentiating curves in G. The Lie algebra $\mathfrak{g}$ is a vector space of dimension $\dim G$, with an algebraic structure called the Lie bracket. Miraculously, the algebraic structure of the algebra $\mathfrak{g}$ (which is linear) almost uniquely determine the group G

(which is nonlinear). In this way, group geometry mostly reduces to algebraic calculations. For two matrices X and Y, the Lie bracket is simply the commutator $[X, Y] = XY - YX$.

The Maurer-Cartan form. Let G be a matrix Lie group and $g(t) \in G$ a curve. Then $dg/dt \equiv \dot{g}$ is the tangent matrix at $g(t)$. To leading order, $g(t+\epsilon) = g(t) + \epsilon\dot{g}(t) + \mathcal{O}(\epsilon^2)$. We can also write $g(t+\epsilon)$ as a product in G: $g(t+\epsilon) = g(t)h(\epsilon)$, where $h(\epsilon) = I + \epsilon X + \mathcal{O}(\epsilon^2)$ for some $X(t) \in \mathfrak{g}$. $h(\epsilon)$ is the group element which generates the translation $t \mapsto t + \epsilon$. Let us isolate the algebra element $X(t)$. To leading order in ϵ,

$$I + \epsilon X(t) = g(t)^{-1}g(t+\epsilon) = g(t)^{-1}(g(t) + \epsilon\dot{g}(t)) = I + \epsilon g(t)^{-1}\dot{g}(t). \tag{A.1}$$

Therefore, $X(t) = g(t)^{-1}\dot{g}(t)$. More generally, we shall be interested in spacetime-dependent curves $g(x)$. We have established an important result: $g(x)^{-1}\partial_\mu g(x) \in \mathfrak{g}$ everywhere in spacetime. This Lie-algebra valued object is known as the Maurer-Cartan form and plays an essential role the theoretical background of this thesis, particularly in the CCWZ construction of described in Appendix A.4.

The group–algebra correspondence. Given a matrix Lie group G with the algebra $\mathfrak{g}$, the matrix exponential function is a map from the algebra to the group, $\exp : \mathfrak{g} \to G$. For this reason, the elements of the algebra are often referred to as the generators of the group G.

The adjoint representation. Let G be a matrix Lie group with associated algebra $\mathfrak{g}$. Take $g \in G$ and $X \in \mathfrak{g}$. Then the adjoint representation of G, denoted Ad, is the natural representation of G acting on its algebra:

$$\mathrm{Ad}_g\, X \equiv gXg^{-1}. \tag{A.2}$$

The adjoint representation of the group is simply the linearized version of the action of G on itself by conjugation.

A closely related notion is that of the adjoint representation of the algebra. Suppose that $g \simeq I + \epsilon X \in G$ for $X \in \mathfrak{g}$. Take $Y \in \mathfrak{g}$. Then the adjoint representation of the group induces a

representation of the algebra:

$$\mathrm{Ad}_g\, Y = (I + \epsilon X)Y(I - \epsilon X) + \mathcal{O}(\epsilon^2) \tag{A.3}$$

$$\simeq Y + \epsilon\,(XY - YX) \tag{A.4}$$

$$= Y + \epsilon[X, Y] \tag{A.5}$$

$$\equiv (I + \epsilon\,\mathrm{ad}_X)Y. \tag{A.6}$$

In other words, $\mathrm{ad}_X : \mathfrak{g} \to \mathfrak{g}$ is map given by $\mathrm{ad}_X = [X, \cdot]$. It is sometimes useful to encode the relation between adjoint representation of the group and the algebra as using the exponential map: $\mathrm{Ad}_{\exp X} = \exp(\mathrm{ad}_X)$, which is valid as matrix equation for all $X \in \mathfrak{g}$. An example makes the meaning of this equation clear. Take $Y \in \mathfrak{g}$. Then

$$\mathrm{Ad}_{\exp X}\, Y = \exp(\mathrm{ad}_X)Y \tag{A.7}$$

$$e^X Y e^{-X} = \sum_{n=0}^{\infty} \frac{(\mathrm{ad}_X)^n}{n!} Y = Y + [X, Y] + \frac{1}{2!}[X, [X, Y]] + \cdots . \tag{A.8}$$

The Killing form. The Killing form is a real, symmetric bilinear form defined on the adjoint representation. Let $X, Y \in \mathfrak{g}$.

$$\kappa(X, Y) = \mathrm{Tr}(\mathrm{ad}_X, \mathrm{ad}_Y). \tag{A.9}$$

This expression can be made more concrete. Let $\{T_i\}$ be a basis for $\mathfrak{g}$ with associated structure constants f_{ijk}. The $(ij)^{\text{th}}$ component of Killing form is

$$\kappa_{ij} = \kappa(T_i, T_j) = \mathrm{Tr}(\mathrm{ad}_{T_i}\, \mathrm{ad}_{T_j}) = f_{ilk} f_{jkl}. \tag{A.10}$$

When $\mathfrak{g}$ is *semi-simple*, the Killing form is non-degenerate. The existence of the Killing form means that one can always "raise and lower" adjoint indices. As a familiar example, the Killing form for $\mathfrak{su}(2)$ in the standard basis is

$$\kappa_{ab} = \epsilon_{adc}\epsilon_{bcd} = -2\delta_{ab}. \tag{A.11}$$

Derivative of the exponential. In physical applications, it is essential to be able to take the derivative of a group element written as the exponential of generators. The most compact

formula for doing so is written in terms of the adjoint representation. Suppose $X = X(x) \in \mathfrak{g}$ is a function of the spacetime coordinate x. Then

$$\partial_\mu e^X = e^X \left(\frac{1 - e^{-\operatorname{ad}_X}}{\operatorname{ad}_X} \right) \partial_\mu X \tag{A.12}$$

$$= e^X \sum_{n=0}^{\infty} \frac{(-1)^n}{(n+1)!} (\operatorname{ad}_X)^n \partial_\mu X \tag{A.13}$$

$$= e^X \left(\partial_\mu X - \frac{1}{2!}[X, \partial_\mu X] + \frac{1}{3!}[X, [X, \partial_\mu X]] + \cdots \right). \tag{A.14}$$

The Baker–Campbell–Hausdorff formula. Let $X, Y \in \mathfrak{g}$. Then $e^X e^Y = e^Z$ with

$$Z = X + Y + \frac{1}{2}[X, Y] + \frac{1}{12}\left([X, [X, Y]] + [Y, [Y, X]]\right) + \cdots . \tag{A.15}$$

Factors of the complex unit. So far, none of the formulae in this Appendix have involved the use of the complex unit, i. In physical applications, one customarily removes a factor of i from the generators and therefore writes $g = e^{iT}$, where T is a generator. The motivation for this notation is twofold. First, this convention emphasizes the connection to the Euler formula and invites the reader to think of T as an "angular variable." Second, and more importantly, this convention renders the generators Hermitian. Hermitian matrices, of course, play a privileged role in quantum mechanics, where they serve as observables.

Graphical identities involving the generators Practical applications present products of generators in various partially contracted forms. Two important identities often allow these products to be simplified for the generators of $\mathrm{SU}(N)$ and $\mathrm{SO}(N)$:

$$\mathrm{SU}(N) : (T_i)^a{}_b (T_i)^c{}_d = \delta^a{}_d \delta^c{}_b - \frac{1}{N} \delta^a{}_b \delta^c{}_d \tag{A.16}$$

$$\mathrm{SO}(N) : (T_i)_{ab} (T_i)_{cd} = \frac{1}{2} \left(\delta_{ad} \delta_{cb} - \delta_{ac} \delta_{bd} \right). \tag{A.17}$$

Such expressions, while useful, are impossible to understand. Graphical versions of these identities, on the other hand, allow one to grasp quickly the meaning of complicated tensor expressions and are given in Figure A.1. Most group theoretical calculations encountered in physics can be reduced to an elegant diagrammatic formulation developed by Cvitanović [47, 48].

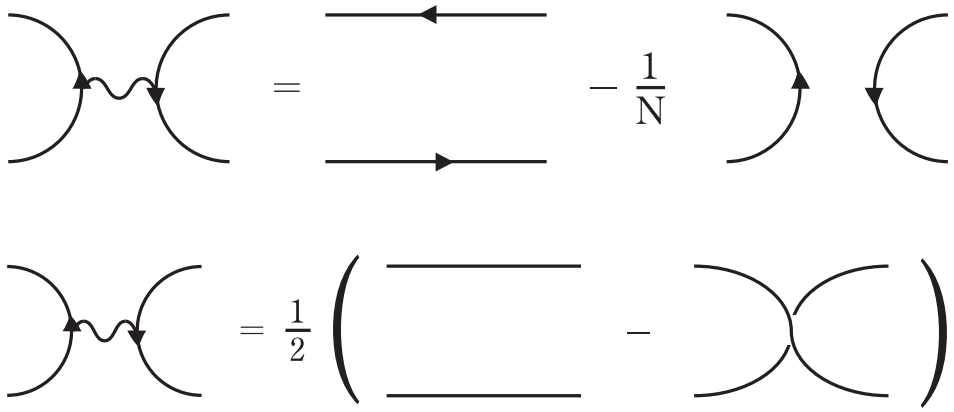

Figure A.1: Some useful birdtrack diagrams for reducing contractions of SU(N) and SO(N) generators.

A.2 Symmetry Properties of Common Lattice Operators

In this appendix we review the symmetry properties of operators which appear commonly in lattice calculations. Broadly speaking, two sorts of fields appear: mesons ($\bar{\psi}\Gamma\psi$) and baryons $\Gamma^A\psi\left(\psi^{\mathrm{T}}\Gamma^B\psi\right)$. The so-called diquark operators, ($\psi^T\Gamma\psi$), play a special role in baryons. Although elementary field theory texts discuss meson operators, diquark operators typically receive less attention.

Proposition 1. *The diquark operator* ($\psi^T C\Gamma\psi$) *is Lorentz invariant for all products of gamma matrices* Γ.

Proof. The proof proceeds via direct computation and relies on the fact that the matrix C provides a basis-independent notion of the transpose,

$$C\gamma_\mu C = \gamma_\mu^{\mathrm{T}}, \tag{A.18}$$

and, moreover, squares to minus the identity, $C^2 = -\mathbb{1}$. Recall that a Dirac fermion transforms as $\psi \mapsto \Lambda_S\psi = \exp\left[i\theta^{\mu\nu}S_{\mu\nu}\right]\psi \simeq \psi + \delta\psi$, where $\delta\psi \equiv i\theta^{\mu\nu}S_{\mu\nu}\psi$ with $S_{\mu\nu} \equiv \frac{i}{4}\left[\gamma^\mu, \gamma^\nu\right]$. Recall also that the generators $S_{\mu\nu}$ of fermion transformations commute with the gamma matrices: $[S_{\mu\nu}, \gamma_\rho] = 0$.

Consider the infinitesimal variation of the diquark operator, $\delta(\psi^T C\Gamma\psi)$:

$$\delta(\psi^T C\Gamma\psi) = \delta(\psi^{\mathrm{T}})C\Gamma\psi + \psi^{\mathrm{T}}C\Gamma\delta\psi \tag{A.19}$$

$$= i\theta^{\mu\nu}\left(\psi^{\mathrm{T}}S^{\mathrm{T}}_{\mu\nu}C\Gamma\psi + \psi^{\mathrm{T}}C\Gamma S_{\mu\nu}\psi\right) \tag{A.20}$$

$$= i\theta^{\mu\nu}\left(\psi^{\mathrm{T}}CS_{\mu\nu}C^2\Gamma\psi + \psi^{T}C\Gamma S_{\mu\nu}\psi\right) \tag{A.21}$$

$$= i\theta^{\mu\nu}\left(-\psi^{\mathrm{T}}CS_{\mu\nu}\Gamma\psi + \psi^{T}C\Gamma S_{\mu\nu}\psi\right) \tag{A.22}$$

$$= i\theta^{\mu\nu}\left(\psi^{\mathrm{T}}C[\Gamma, S_{\mu\nu}]\psi\right) = 0, \tag{A.23}$$

where we have used $[\Gamma, S_{\mu\nu}] = 0$ in the final equality. The diquark operator $\psi^T C\Gamma\psi$ is therefore Lorentz invariant, as claimed. □

Proposition 2. *Meson and diquark operators obey the classification of Table A.1 in terms of spin J and parity P.*

Table A.1: The J^P classification of meson and diquark operators.

Γ	Meson $(\bar{\psi}\Gamma\psi)$ J^P	Diquark $(\psi^{\mathrm{T}}C\Gamma\psi)$ J^P
$\mathbb{1}$	0^+	0^-
γ_4	0^+	0^-
γ_5	0^-	0^+
$\gamma_4\gamma_5$	0^-	0^+
γ_i	1^-	1^+
$\gamma_4\gamma_i$	1^-	1^+
$\gamma_i\gamma_5$	1^+	1^-
$\epsilon^{ijk}\gamma_j\gamma_k$	1^+	1^-

Proof. We begin by recalling the transformation properties of spinors under parity:

$$\mathcal{P} : \psi(\vec{x}, t) \mapsto \gamma_4\psi(-\vec{x}, t) \tag{A.24}$$

$$\psi(\vec{x}, t)^{\mathrm{T}} \mapsto \psi(-\vec{x}, t)^{\mathrm{T}}\gamma_4^T \tag{A.25}$$

$$\bar{\psi}(\vec{x}, t) \mapsto \bar{\psi}(-\vec{x}, t)\gamma_4. \tag{A.26}$$

Therefore, in the classification of mesonic operators $(\bar{\psi}\Gamma\psi)$, it suffices to determine the transforma-

tion rules for $\gamma_4\Gamma\gamma_4$. Because $\gamma_4^2 = \mathbb{1}$, the scalar operators $\Gamma \in \{\mathbb{1}, \gamma_4\}$ satisfy

$$\gamma_4\Gamma\gamma_4 = +\Gamma. \tag{A.27}$$

Because $\{\gamma_4, \gamma_5\} = 0$, the pseudoscalar operators $\Gamma \in \{\gamma_5, \gamma_4\gamma_5\}$ satisfy,

$$\gamma_4\Gamma\gamma_4 = -\Gamma. \tag{A.28}$$

For the vector operators $\Gamma \in \{\gamma_i, \gamma_4\gamma_i\}$, one uses the fact that $\{\gamma_4, \gamma_i\} = 0$ for $i \neq 4$. Then it follows that

$$\gamma_4\Gamma\gamma_4 = -\Gamma. \tag{A.29}$$

It also follows from the previous arguments that the pseudovector operator $\Gamma = \gamma_i\gamma_5$ and the tensor operator $\Gamma = \gamma_j\gamma_k$ satisfy

$$\gamma_4\Gamma\gamma_4 = +\Gamma, \tag{A.30}$$

thereby completing our classification of meson operators. In order to classify the diquark operators, we remind ourselves that the "charge conjugation" matrix satisfies the following useful properties. First, it provides a basis independent notion of transposition: $C\gamma_\mu C = \gamma_\mu^{\mathrm{T}}$. Second, the charge conjugation matrix squares to minus the identity: $C^2 = -\mathbb{1}$. Because the diquark operators have the form $(\psi^{\mathrm{T}} C\Gamma\psi)$, it suffices to classify the transformation rules of $\gamma_4^{\mathrm{T}} C\Gamma\gamma_4$. But this combination satisfies the following relation:

$$\gamma_4^{\mathrm{T}} C\Gamma\gamma_4 = (\gamma_4^{\mathrm{T}} C)(\Gamma\gamma_4) = C\gamma_4 C^2(\Gamma\gamma_4) = -C\gamma_4(\Gamma\gamma_4) = -C(\gamma_4\Gamma\gamma_4) = \mp C\Gamma. \tag{A.31}$$

In the last equality we used that previous classification of meson operators according to the behavior of $\gamma_4\Gamma\gamma_4$. Therefore, the parity of the diquark operators differ by a minus sign from the corresponding meson operators.

To complete the classification, we should clarify what is meant by spin J. For the (pseudo)scalars, this statement is simply the fact that the operators are invariant in the sense of carrying no free Lorentz indices. The (pseudo)vectors transform under vector representations of SO(3), the little

group of the massive state excited by the particle. Note that γ_4 plays a privileged role in this construction. This role is simply due the fact that, at zero spatial momentum (i.e., in the privileged frame of massive particle), the "u" and "v" spinors are eigenstates of γ_4 with eigenvalues $+1$ and -1, respectively. For the tensor operator $\gamma_i\gamma_j$, one uses the decomposition

$$\gamma_j\gamma_k = \gamma_{[j}\gamma_{k]} + \gamma_{(j}\gamma_{k)} \tag{A.32}$$

$$= \gamma_{[j}\gamma_{k]} + \frac{1}{2}\delta_{jk}\mathbb{1}. \tag{A.33}$$

The first term is the 3-dimensional antisymmetric subspace $3 \subset 3 \otimes 3$. As with the usual cross product, one can index this subspace with the Levi-Civita symbol of the Little Group SO(3) serving as the "Clebsch-Gordan" coefficient, i.e., $\epsilon^{ijk}\gamma_j\gamma_k$. □

Proposition 3. *A baryon operator of the form $\psi(\psi^T C\Gamma\psi)$ couples to eigenstates of both positive and negative parity.*

Proof. As the classification of Prop. 2 showed, the diquark operators $(\psi^{\mathrm{T}} C\Gamma\psi)$ transform with definite parity—positive or negative. Therefore it suffices to consider the parity of the field ψ with free Lorentz indices. But a generic massive Dirac spinor ψ contains both positive and negative parities, and so the baryon operator couples to both of them. □

Projection operators $P_\pm = \frac{1}{2}(\mathbb{1} \pm \gamma_4)$ construct baryon operators of definite parity, as the following proposition demonstrates.

Proposition 4. *Consider baryon operators $P_\pm\Gamma_A\psi(\psi^T C\gamma_B\psi)$. The choices*

$$(\Gamma_A, \Gamma_B) \in \{(\mathbb{1}, \gamma_5), (\gamma_5, \mathbb{1}), (\mathbb{1}, \gamma_4\gamma_5)\} \tag{A.34}$$

have definite parity, given by the sign of $P_\pm$.

Proof. The first case of $(\mathbb{1}, \gamma_5)$ is trivial, since the diquark transforms with positive parity, and $P_\pm\psi$ transforms with definite parity. For the second case of $(\gamma_5, \mathbb{1})$, we observe that $(\psi^T C\psi)$ transforms with negative parity. Moreover, $P_\pm\gamma_5 = \gamma_5 P_\mp$. The two minus signs cancel, thereby producing a

baryon operator with the correct spin. (More precisely, if one considers scalar two-point correlation functions by tracing over the free spinor index, the free γ_5 of the source and sink operator will annihilate, since $\gamma_5^2 = \mathbb{1}$. Then the source and sink operators really do couple to states of the correct definite parity.) The final case of $(\mathbb{1}, \gamma_4\gamma_5)$ is also trivial, since the diquark transforms with positive parity. □

A.3 Goldstone's Theorem

Theorem 1 (Goldstone's Theorem)**.** *Suppose that a field theory has global symmetry $\mathcal{G}_F$ which is spontaneously broken to the subgroup $\mathcal{H}_F \subset \mathcal{G}_F$. Then the vacuum manifold consists of* $\dim \mathcal{G}_F/\mathcal{H}_F$ *massless modes.*

Proof. Let ϕ_a generically denote the field content of the theory, with the index a serving as a collective index. Because $\mathcal{G}_\mathrm{F}$ is a global symmetry of the theory, it is also symmetry of the potential $V(\phi)$. Therefore, the variation of the potential under an infinitesimal $\mathcal{G}_\mathrm{F}$-variation must vanish:

$$\delta V = \delta\phi_a \frac{\partial V}{\partial \phi_a} = 0, \tag{A.35}$$

where $\delta\phi_a = i\theta^\alpha (T_\alpha)_{ab}\phi_b$ and the T_α are the generators of $\mathcal{G}_\mathrm{F}$. This statement is true even at a generic point in field space. Consider now a minimum in field space, so that $\partial V/\partial\phi_a$ vanishes. The curvature matrix of second derivatives at the minimum of the potential determines the mass spectrum. To probe this quantity, we take the derivative of the previous equation

$$0 = \frac{\partial}{\partial \phi_b}\left(\delta\phi_a \frac{\partial V}{\partial \phi_a}\right) \tag{A.36}$$

$$= \delta\phi_a \frac{\partial^2 V}{\partial\phi_b \partial\phi_a} \tag{A.37}$$

$$= \delta\phi_a M^2_{ab}, \tag{A.38}$$

where we've used that $\partial V/\partial\phi_a$ vanishes. The generators of the unbroken symmetry $\mathcal{H}_\mathrm{F}$ produce vanishing variations ($\delta\phi_a = 0$), while generators of the coset $\mathcal{G}_\mathrm{F}/\mathcal{H}_\mathrm{F}$ generate non-vanishing variations ($\delta\phi_a \neq 0$). Therefore the mass matrix has $\dim \mathcal{G}_\mathrm{F}/\mathcal{H}_\mathrm{F}$ eigenvectors with eigenvalue zero, corresponding to $\dim \mathcal{G}_\mathrm{F}/\mathcal{H}_\mathrm{F}$ massless modes.

We have completed the proof for classical field theory. The proof in the quantum mechanical case is similar, relying on the fact that the conserved charge associated with the broken symmetry generates a manifold of states. □

A.4 The General CCWZ Construction

The Callan–Coleman–Wess–Zumino (CCWZ) construction provides a general method for writing down the effective field theory of a broken global symmetry $\mathcal{G}_{\rm F} \to \mathcal{H}_{\rm F}$. The idea is to construct the induced, nonlinear representation of $\mathcal{G}_{\rm F}$ acting on the broken generators in $\mathcal{G}_{\rm F}/\mathcal{H}_{\rm F}$. The power of their method lies in the fact that, after determining the objects which transform homogeneously under $\mathcal{G}_{\rm F}$, it suffices to construct Lagrangians which are superficially invariant under the subgroup $\mathcal{H}_{\rm F}$. This appendix describes the CCWZ construction. The discussion in Panico and Wulzer is a useful companion [121] to the original classic papers [38, 43].

Consider a Lie group $\mathcal{G}_{\rm F}$ with a Lie subgroup $\mathcal{H}_{\rm F}$. We shall denote the generators of $\mathcal{H}_{\rm F}$ as T^a; they are the "unbroken generators" and carry an un-hatted index. We shall denote the remaining generators of $\mathcal{G}_{\rm F}$ as $X^{\hat{a}}$; the are the "broken generators" and carry a hatted index. Often it will be a convenient to overload our terminology to refer to the $X^{\hat{a}}$ simultaneously as being generators of $\mathcal{G}_{\rm F}$ and of the coset $\mathcal{G}_{\rm F}/\mathcal{H}_{\rm F}$. Let us first consider the transformation properties of the generators.

$$[T, T] = T \tag{A.39}$$

$$[T, X] = X \tag{A.40}$$

$$[X, X] = T + X \tag{A.41}$$

The first equation says that, since $\mathcal{H}_{\rm F}$ is a group, its generators close to form an algebra. The second equation say that $\mathcal{G}_{\rm F}/\mathcal{H}_{\rm F}$ transforms in a (linear) representation of the unbroken $\mathcal{H}_{\rm F}$. The final equation provides the essential complication and says that the generators of $\mathcal{G}_{\rm F}/\mathcal{H}_{\rm F}$ do not close, since the coset is not, in general, a group. Moreover, the final equation says that $\mathcal{G}_{\rm F}/\mathcal{H}_{\rm F}$ transforms in a *nonlinear* representation of the full group $\mathcal{G}_{\rm F}$. All three equations can be summarized by the decomposition $\mathrm{Ad}_{\mathcal{G}_{\rm F}} = \mathrm{Ad}_{\mathcal{H}_{\rm F}} \oplus \mathbf{r}_\pi$. The final summand, $\mathbf{r}_\pi$, is the induced representation of the

Goldstone bosons.

A certain subclass of symmetry breaking patterns, known as symmetric spaces, play a special role in many physical applications, including QCD. A symmetric space enjoys a discrete "parity" symmetry. This notion of parity is a group automorphism of $\mathcal{G}_{\rm F}$ which swaps the sign of the broken generators:

$$P : T^a \longmapsto +T^a \tag{A.42}$$

$$X^{\hat{a}} \longmapsto -X^{\hat{a}}. \tag{A.43}$$

This symmetry simplifies the commutation relation in Eq. (A.41) and requires that $[X, X] = T$. Although the induced representation remains nonlinear, certain formulae simplify.

To see more clearly what is meant by a non-linear representation, let us reconsider the physical motivation. In the presence of a broken symmetry $\mathcal{G}_{\rm F} \to \mathcal{H}_{\rm F}$, the vacuum manifold remains invariant under the unbroken subgroup $\mathcal{H}_{\rm F}$ while acquiring non-trivial transformation properties under the full group $\mathcal{G}_{\rm F}$. Suppose that F is some particular vacuum state within Hilbert space. The Goldstone matrix $U[\xi] = e^{i\xi_{\hat{a}} X^{\hat{a}}}$ is an element of the coset $\mathcal{G}_{\rm F}/\mathcal{H}_{\rm F}$. Acting with $U[\xi]$ reorients F within the (degenerate) vacuum manifold: $F \longmapsto U[\pi]F$. Our task is to infer an action of $\mathcal{G}_{\rm F}$ on $\mathcal{G}_{\rm F}/\mathcal{H}_{\rm F}$ which preserves the form of the Goldstone matrix.

The natural action of $\mathcal{G}_{\rm F}$ on the pion field is that of conjugation ($\xi \mapsto g\xi g^{-1}$), and infinitesimal conjugation is commutation. According to Eq. (A.41), an arbitrary transformation in $\mathcal{G}_{\rm F}$ pushes the Goldstone matrix out of the coset. This relation suggests that one should first act on $\mathcal{G}_{\rm F}/\mathcal{H}_{\rm F}$ with a group element and then include a "correction step" in order to return the result to the coset. Let $g \in \mathcal{G}_{\rm F}$ act on U with left multiplication. Without loss of generality, we can write the result in the following factored form:

$$g\, U[\xi] = U[\xi']\, h[g; \xi], \tag{A.44}$$

where $U[\xi'] \in \mathcal{G}_{\rm F}/\mathcal{H}_{\rm F}$ and $h[g; \xi] \in \mathcal{H}_{\rm F}$. Both quantities depend implicitly on the original Goldstone matrix and the group element g. This factorization inspires us to *define* a representation $\mathcal{D}(\mathcal{G}_{\rm F})$

acting on the Goldstone matrix as

$$\mathcal{D}(\mathcal{G}_{\rm F}) : \mathcal{G}_{\rm F}/\mathcal{H}_{\rm F} \to \mathcal{G}_{\rm F}/\mathcal{H}_{\rm F} \tag{A.45}$$

$$U[\xi] \longmapsto U[\xi'] = gU[\xi]h^{-1}[g;\xi]. \tag{A.46}$$

In the literature on Lie groups, this representation is known as the induced representation. In the physics literature, $\mathcal{D}(\mathcal{G}_{\rm F})$ is often called a nonlinear realization of the symmetry, since the new Goldstone fields ξ' are a nonlinear function of ξ and g.

Because the "correction function" h is implicit and nonlinear, no explicit formula exists for general groups. Moreover, its explicit form is not generally necessary or useful in practical applications. However, the linearized from of this equation is instructive:

$$gU = (1 + ig_{\hat{a}}X^{\hat{a}} + ig_a T^a)(1 + i\xi_{\hat{a}}X^{\hat{a}}) + \mathcal{O}(g^2, \xi^2) \tag{A.47}$$

$$\simeq 1 + i(\xi_{\hat{a}} + g_{\hat{a}})X^{\hat{a}} + ig_a T^a \tag{A.48}$$

$$\simeq (1 + i(\xi_{\hat{a}} + g_{\hat{a}})X^{\hat{a}})(1 + ig_a T^a) \tag{A.49}$$

$$= (1 + i\xi'_{\hat{a}}X^{\hat{a}})h. \tag{A.50}$$

From this expression, we can read off the leading-order results for the implicit function h and the transformed Goldstone modes:

$$h^{-1} = (1 - ig_a T^a) \simeq e^{-ig_a T^a} \tag{A.51}$$

$$\xi'_{\hat{a}} = \xi_{\hat{a}} + g_{\hat{a}}. \tag{A.52}$$

The latter result is particularly important; it says that the Goldstone modes enjoy a shift symmetry under the nonlinear representation of $\mathcal{G}_{\rm F}$ acting on $\mathcal{G}_{\rm F}/\mathcal{H}_{\rm F}$. Because the resulting dynamics must obey this symmetry, the interactions between Goldstone bosons in the EFT must contain derivatives and therefore vanish at zero momentum. Beyond leading order, the Goldstone bosons transform with a nonlinear shift.

In order to construct a $\mathcal{G}_{\rm F}$-invariant Lagrangian, we must take derivatives. Consider therefore the Maurer-Cartan form $U^{-1}\partial_\mu U$, which takes values in the algebra. We can decompose this object

into components along the broken and unbroken generators,

$$iU^{-1}\partial_\mu U = d_{\mu,\hat{a}} X^{\hat{a}} + e_{\mu,a} T^a = \mathbf{d}_\mu + \mathbf{e}_\mu, \tag{A.53}$$

where the factor of i cancels that emerging from the use of Hermitian group generators. This expression defines the symbols $\mathbf{d}_\mu$ and $\mathbf{e}_\mu$, which transform in the following suggestive manner.

$$U^{-1}\partial_\mu U \longmapsto U'^{-1}\partial_\mu U' \tag{A.54}$$

$$= (hU^{-1}g^{-1})\partial_\mu(gUh^{-1}) \tag{A.55}$$

$$= hU^{-1}\partial_\mu U h^{-1} + h\partial_\mu h^{-1} \tag{A.56}$$

$$= h\mathbf{d}_\mu h^{-1} + h\mathbf{e}_\mu h^{-1} - (\partial_\mu h)h^{-1}. \tag{A.57}$$

Since h is an element of $\mathcal{H}_\mathrm{F}$, the last term $(\partial_\mu h)h^{-1}$ contains only generators of $\mathcal{H}_\mathrm{F}$. Therefore $\mathbf{e}_\mu$ contains a shift, while $\mathbf{d}_\mu$ transforms homogeneously:

$$\mathbf{d}_\mu \mapsto h\mathbf{d}_\mu h^{-1} \tag{A.58}$$

$$\mathbf{e}_\mu \mapsto h\mathbf{e}_\mu h^{-1} - (\partial_\mu h)h^{-1}. \tag{A.59}$$

We can summarize the results with two statements. First, $\mathbf{d}_\mu$ is the "covariant derivative of ξ" (in the sense $\mathbf{d}_\mu = \partial_\mu\xi + \dots$) which transforms correctly under the full group $\mathcal{G}_\mathrm{F}$. That is, $\mathbf{d}_\mu$ neatly packages the infinite series of terms—involving different numbers of fields—necessary to maintain nonlinear symmetry of Eq. (A.52) to all orders. Second, $\mathbf{e}_\mu$ transforms as a non-abelian gauge field of $\mathcal{H}_\mathrm{F}$. If any unbroken symmetries are gauged, the symbol $\mathbf{e}_\mu$ is used to construct, e.g., field strength tensors with the correct $\mathcal{G}_\mathrm{F}$ transformation properties.

Computing explicit formulae for the $\mathbf{d}_\mu$ and $\mathbf{e}_\mu$ symbols means computing the Maurer-Cartan form. To do so, we need the derivative of the exponential function, which is given by Eq. (A.12). This result tells us that the Maurer-Cartan form is

$$iU^{-1}\partial_\mu U = i\left(\frac{1 - e^{-i\,\mathrm{ad}_\xi}}{\mathrm{ad}_\xi}\right)\partial_\mu\xi. \tag{A.60}$$

In the case of a symmetric space, a notion of parity decomposes the Maurer-Cartan form along the broken and unbroken generators, which contain either an odd or even number of commutators, respectively. This fact is useful in the computations of Appendix A.5.

At lowest-order, the most general $\mathcal{G}_{\rm F}$-invariant Lagrangian is simply $\mathcal{L} \sim \operatorname{Tr} \mathbf{d}_{\mu\hat{a}} \mathbf{d}^{\mu\hat{a}}$. Note in particular that this expression does *not* include a term $\sim \operatorname{Tr} \mathbf{e}_{\mu a} \mathbf{e}^{\mu a}$. Because $\mathbf{e}_\mu$ transforms with a linear shift, this quantity is not invariant under a general $\mathcal{G}_{\rm F}$ transformation.

To write the Lagrangian in a more transparently physical form, we shall reinstate dimensions. First, we observe that the Goldstone modes ξ are dimensionless angular variables. Since the Goldstone modes are bosonic excitations, the should have mass-dimension unity. Therefore, one writes $\xi = \sqrt{2}\pi/f$, where π now denotes the "pion field." The factor of $\sqrt{2}$ is conventional. The low-energy constant f is the pion decay constant. Next, since $\mathbf{d}_\mu \simeq \partial_\mu \xi + \cdots = \partial_\mu \sqrt{2}\pi/f + \cdots$, we must rescale the overall Lagrangian to possess a canonically normalized kinetic term. Overall one finds

$$\mathcal{L} = \frac{f^2}{4} \operatorname{Tr} \mathbf{d}_{\mu\hat{a}} \mathbf{d}^{\mu\hat{a}}. \tag{A.61}$$

A.5 CCWZ for SO(5)/SO(4)

In this section we compute the decomposition of the Maurer-Cartan form into the tensor $\mathbf{d}_\mu$ for the case of SO(5)/SO(4) broken symmetry. We consider the expressions both with and without external gauge fields for the unbroken symmetry SO(4). In principle, one can choose an explicit basis of generators for SO(5) and compute the matrix exponential

$$U[\pi] = \exp \frac{i\sqrt{2}\pi_{\hat{a}}}{f} T^{\hat{a}}. \tag{A.62}$$

The results would then follow by taking explicit derivatives. Instead, we find it convenient to tread more lightly, using only the abstract group structure to guide the calculation.

We recall the definition $iU[\pi]^{-1}\partial_\mu U[\pi] = \mathbf{d}_\mu + \mathbf{e}_\mu$, where $\mathbf{d}_\mu$ is parallel to the broken gener-

ators. Using Eq. (A.12) for the derivative of an exponential from Lie theory, we find:

$$iU[\pi]^{-1}\partial_\mu U[\pi] = i(\partial_\mu \pi_{\hat{a}}) \sum_{n=0}^{\infty} \frac{(-1)^n}{(n+1)!} \left(\frac{i\sqrt{2}}{f}\right)^n \left(\pi_{\hat{b}}\, \mathrm{ad}_{T^{\hat{b}}}\right)^n T^{\hat{a}}. \tag{A.63}$$

Because SO(5)/SO(4) is a symmetric space, terms involving even powers of $\mathrm{ad}_{T^{\hat{b}}}$ (i.e., even numbers of commutators) will belong to the coset, while odd powers will be parallel to to unbroken generators. Therefore, computing $\mathbf{d}_\mu$ amounts to summing even powers, which the following lemma enables.

Lemma 1. *For $n > 0$, the following formula computes even powers of ad_π acting on the broken generators:*

$$(\partial_\mu \pi_{\hat{a}})(\mathrm{ad}_\pi^2)^n T^{\hat{a}} = \frac{1}{2^n}\left[(\pi^2)^n(\partial_\mu \pi_{\hat{a}}) - (\partial_\mu \pi \cdot \pi)(\pi^2)^{n-1}\pi_{\hat{a}}\right] T^{\hat{a}} \tag{A.64}$$

Proof. The proof shall proceed by induction. To establish notation, we shall use the commutation relations

$$[T^{\hat{b}}, T^{\hat{a}}] = (t_d)^{\hat{a}\hat{b}} T^d \tag{A.65}$$

$$[T^d, T^{\hat{c}}] = T^{\hat{e}} (t^d)_{\hat{e}}{}^{\hat{c}} \tag{A.66}$$

and the completeness relation for orthogonal groups

$$(t^e)^{\hat{d}\hat{c}}(t_e)^{\hat{b}\hat{a}} = \frac{1}{2}\left(\delta^{\hat{d}\hat{a}}\delta^{\hat{c}\hat{b}} - \delta^{\hat{d}\hat{b}}\delta^{\hat{c}\hat{a}}\right), \tag{A.67}$$

where the t_a are generators of SO(4). We remark that hatted indices can be raised and lowered trivially. To established the base case, we compute $(\mathrm{ad}_\pi)^2 \partial_\mu \pi$. Consider first the double commutator. The commutation relations together with a single application of the completeness relation delivers:

$$[T^{\hat{c}}, [T^{\hat{b}}, T^{\hat{a}}]] = \frac{1}{2}\left(\delta^{\hat{d}\hat{a}}\delta^{\hat{c}\hat{b}} - \delta^{\hat{d}\hat{b}}\delta^{\hat{c}\hat{a}}\right) T_{\hat{d}}. \tag{A.68}$$

Contracting this quantity with $\pi_{\hat{c}}\pi_{\hat{b}}\partial_\mu \pi_{\hat{a}}$, we find

$$\frac{1}{2}\left(\pi \cdot \pi(\partial_\mu \pi_{\hat{a}}) - (\partial_\mu \pi \cdot \pi)\pi_{\hat{a}}\right) T^{\hat{a}}, \tag{A.69}$$

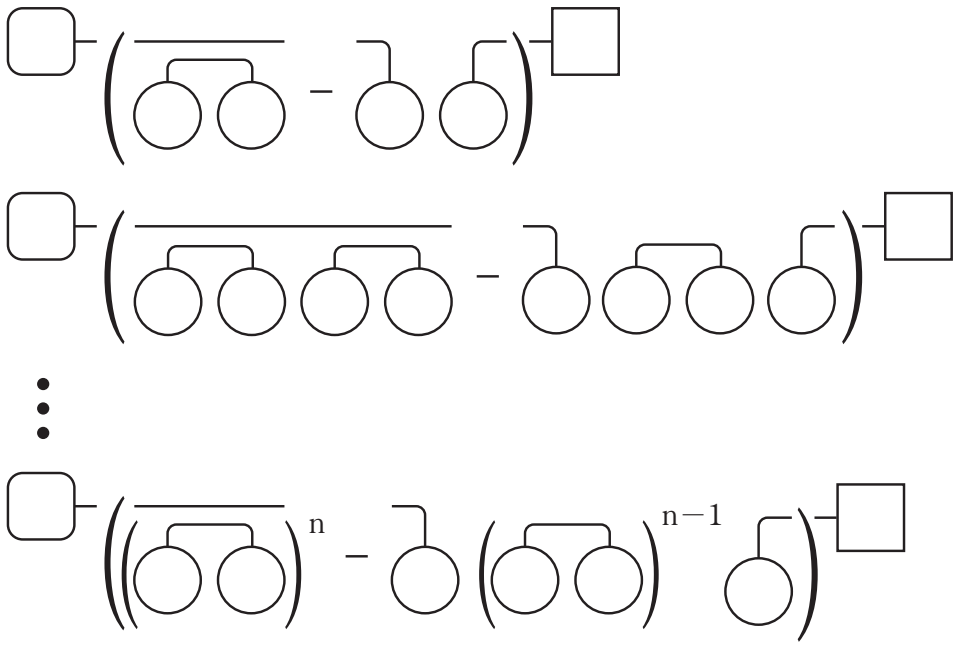

Figure A.2: A graphical demonstration of the inductive proof of the preceding lemma. The square represents the generator $T^{\hat{a}}$, the circles represent $\pi_{\hat{a}}$, and the rounded rectangle represents $\partial\pi_{\hat{a}}$. The first line establishes the base case, and the induction proceeds by contracting powers of the quantity in parentheses.

which is the desired expression for $n = 1$. Suppose now that the expression holds for the n^{th} case.

$$\frac{1}{2^n}\left[(\pi^2)^n(\partial_\mu\pi_{\hat{a}}) - (\partial_\mu\pi\cdot\pi)(\pi^2)^{n-1}\pi_{\hat{a}}\right]\pi_{\hat{c}}\pi_{\hat{b}}[T^{\hat{c}},[T^{\hat{b}},T^{\hat{a}}]] \tag{A.70}$$

$$= \frac{1}{2^n}\left[(\pi^2)^n(\partial_\mu\pi_{\hat{a}}) - (\partial_\mu\pi\cdot\pi)(\pi^2)^{n-1}\pi_{\hat{a}}\right]\pi_{\hat{c}}\pi_{\hat{b}}\frac{1}{2}\left(\delta^{\hat{d}\hat{a}}\delta^{\hat{c}\hat{b}} - \delta^{\hat{d}\hat{b}}\delta^{\hat{c}\hat{a}}\right)T_{\hat{d}} \tag{A.71}$$

$$= \frac{1}{2^{n+1}}\left[(\pi^2)^{n+1}(\partial_\mu\pi_{\hat{a}}) - (\partial_\mu\pi\cdot\pi)(\pi^2)^{n}\pi_{\hat{a}}\right] \tag{A.72}$$

Therefore the n^{th} case implies the $(n+1)^{\text{th}}$, completing the proof. Because the tensor contractions are somewhat opaque, more revealing graphical version of the induction appears in Figure A.2. □

With the help of the previous lemma, the sum of the even terms takes the following shape:

$$\mathbf{d}_\mu = -\frac{\sqrt{2}}{f}\sum_{n=0}^{\infty}\frac{1}{(2n+1)!}\left(\frac{i\sqrt{2}}{f}\right)^{2n}\left(\mathrm{ad}_\pi^2\right)^n(\partial_\mu\pi_{\hat{a}})T^{\hat{a}} \tag{A.73}$$

$$= -\frac{\sqrt{2}}{f}\left[\partial_\mu\pi_{\hat{a}} + \sum_{n=1}^{\infty}\frac{(-1)^n}{(2n+1)!}\frac{1}{f^{2n}}\left((\pi^2)^n(\partial_\mu\pi_{\hat{a}}) - (\partial_\mu\pi\cdot\pi)(\pi^2)^{n-1}\pi_{\hat{a}}\right)\right]T^{\hat{a}} \tag{A.74}$$

$$= \left[\sqrt{2}\left(\frac{1}{\pi}\sin\left(\frac{\pi}{f}\right) - \frac{1}{f}\right)\frac{\pi\cdot\partial_\mu\pi}{\pi^2}\pi_{\hat{a}} - \frac{\sqrt{2}}{\pi}\sin\left(\frac{\pi}{f}\right)(\partial_\mu\pi_{\hat{a}})\right]T^{\hat{a}}, \tag{A.75}$$

where we have used the familiar infinite series form of the sine function from elementary calculus. Obtaining this result depended only the abstract group structure of the problem and not on any particular basis of generators.

We now investigate the gauge-covariant derivative $\mathbf{d}_\mu[\pi, A]$ which results from promoting $\partial_\mu \longmapsto \partial_\mu - iA_\mu$, with $A_\mu = A_{\mu,a}T^a$ the gauge field associated with (any desired subset of) the unbroken generators. Evidently we must consider the behavior of the quantity $U[\pi]^{-1}A_\mu U[\pi] = \mathrm{Ad}_{e^{-i\sqrt{2}\pi/f}}A_\mu$. Fortunately, Eq. (A.7) gives exactly the result we need:

$$\mathrm{Ad}_{e^{-i\sqrt{2}\pi/f}}A_\mu = e^{-\frac{i\sqrt{2}}{f}\mathrm{ad}_\pi}A_\mu \tag{A.76}$$

$$= \sum_{n=0}^{\infty}\frac{-1}{n!}\left(\frac{i\sqrt{2}}{f}\right)^n(\mathrm{ad}_\pi)^nA_\mu. \tag{A.77}$$

Because we are computing $\mathbf{d}_\mu[\pi, A]$, we must extract the components parallel to the broken generators. Once again, the fact the SO(5)/SO(4) is a symmetric space provides a simplification. Acting with once with ad_π on A_μ pushes the generator into the coset, and subsequent applications of $(\mathrm{ad}_\pi)^2$ remain in the coset. Therefore, all the odd powers of ad_π acting on A_μ belong to the coset. The sum of the odd powers is:

$$\sum_{n=0}^{\infty}\frac{-1}{(2n+1)!}\left(\frac{i\sqrt{2}}{f}\right)^{2n+1}(\mathrm{ad}_\pi)^{2n+1}A_\mu, \tag{A.78}$$

which is seen to be a sum of the same form as Eq. (A.73). A moment's study of the coefficients confirms that $\mathbf{d}_\mu[\pi, A]$ follows from replacing $\partial_\mu \longmapsto D_\mu$ in $\mathbf{d}_\mu[\pi]$:

$$\mathbf{d}_\mu[\pi, A] = \left[\sqrt{2}\left(\frac{1}{\pi}\sin\left(\frac{\pi}{f}\right) - \frac{1}{f}\right)\frac{\pi\cdot D_\mu\pi}{\pi^2}\pi_{\hat{a}} - \frac{\sqrt{2}}{\pi}\sin\left(\frac{\pi}{f}\right)(D_\mu\pi_{\hat{a}})\right]T^{\hat{a}} \tag{A.79}$$

$$= \left[\sqrt{2}\left(\frac{1}{\pi}\sin\left(\frac{\pi}{f}\right) - \frac{1}{f}\right)\frac{\pi\cdot\partial_\mu\pi}{\pi^2}\pi_{\hat{a}} - \frac{\sqrt{2}}{\pi}\sin\left(\frac{\pi}{f}\right)(D_\mu\pi_{\hat{a}})\right]T^{\hat{a}}, \tag{A.80}$$

where the second equality follows since generators of SO(N) are antisymmetric and the π are bosonic.

A.6 Anomalous Symmetries in QFT

A classical field theory is defined in terms of its symmetries, which specify the classical action. A quantum field theory is defined by allowing the classical fields to fluctuate according to the rules of quantum mechanics, as described mathematically by the path integral. A natural question is whether the quantum fluctuations respect the symmetries of the classical theory. As it turns out, quantum fluctuations often do *not* respect the classical symmetries, inducing effects which the classical theory would seem to forbid. When this effect is present, the symmetry is said to be anomalous.

Anomalous symmetries play an important role in real-world applications. Perhaps the best-known and most physical example is the decay of a neutral pion into two photons: $\pi^0 \to \gamma\gamma$. Because the π^0 is neutral, it does not couple directly to electromagnetism. However, quantum fluctuations induce a coupling at the 1-loop level; this effect goes by the name of the "chiral anomaly."

An elegant method, due to Fujikawa, for computing anomalies in a general setting investigates the measure of the path integral [78]. Although this quantity seems abstract, the motivation is simple: the measure is the quantum part of the quantum field theory. The technical details exceed this scope of this thesis, but general idea is straightforward. Define a path integral in terms of a classical Lagrangian with some global symmetry $\mathcal{G}_{\mathrm{F}}$. Now imagine changing the variables of the path integral by performing a symmetry transformation $g \in \mathcal{G}_{\mathrm{F}}$. The action is invariant by construction. However, as in elementary calculus, the measure transforms with a Jacobian factor. Fujikawa's method computes this Jacobian factor explicitly. The resulting axial anomaly is phrased in terms of the anomalous divergence of the axial current

$$\partial_\mu J^{A,\mu} \propto \frac{1}{16\pi^2} \epsilon^{\mu\nu\rho\sigma} F_{\mu\nu} F_{\rho\sigma}, \tag{A.81}$$

a result which often goes by the name of the Adler-Bell-Jackiw anomaly, after the physicists who

discovered it originally [3, 21].

The axial anomaly has another important consequence for the particle spectrum of QCD. Neglecting the anomaly, the chiral condensate would spontaneously break the axial $U(1)$ symmetry, yielding another light, pseudo-Goldstone boson. Because the anomaly already explicitly breaks this symmetry, no such state is present. Indeed, the meson with the correct valence-quark content is the η', which has a mass of nearly 1GeV.

The role of the anomaly is particularly interesting in multirep gauge theories. In such theories, each fermion species has an anomalous, flavor-singlet axial current. However, a certain linear combinations of these currents will decouple from the anomaly and therefore remain unbroken. In this case, the formation of a chiral condensate breaks the axial symmetry explicitly, and a light, pseudo-Goldstone analogue of the η' appears in the spectrum.

The axial anomaly explains why physicists refer usually refer to the global symmetry group of QCD as $\mathrm{SU}(N)\times\mathrm{SU}(N)\times U(1)_V$. Although the classical action in fact possesses a $U(N)\times U(N) = \mathrm{SU}(N)\times\mathrm{SU}(N)\times U(1)\times U(1)$, the axial $U(1)$ symmetry is anomalous. Discussions of spontaneously broken symmetries then proceed from the non-anomalous global symmetry group. For brevity, the residual vector $U(1)$ symmetry is omitted, since it often remains unbroken, both in the presence of the anomaly and spontaneously broken symmetry.

Appendix B

The Method of Conjugate Gradients

B.1 Overview

The method of conjugate gradients is a numerical algorithm for solving linear systems of the form $Ax = b$. Many explanations of this method exist in the lattice literature and in textbooks [59, 82], but it is useful to reiterate and amplify the usual discussion for the purpose of this thesis. My own understanding has benefited particularly from the discussion of Luenberger and Ye [114]. Aside from rephrasing and incidental remarks, the essential mathematical ideas below are are theirs.

Solving the system $Ax = b$ amounts to inverting the matrix A. Compared to direct inversion, the method of conjugate gradients is most advantageous for sparse matrices. The geometric origin of conjugate gradient comes from recognizing that A is quadratic form. Instead of directly solving $Ax = b$, one instead solves the auxiliary problem of minimizing the function $f(x) = \frac{1}{2}x \cdot Ax - b \cdot x + c$, the gradient of which is simply $Ax - b$. When A is positive-definite, looking for a unique minimum is a well-posed question. When A is also symmetric, finding this minimum is equivalent to solving the linear system $Ax = b$. The method of conjugate gradients provides a way to find the minimum and solve the system. These hypothesis are not strictly satisfied by Dirac operators encountered in lattice gauge theory, but the necessary modifications are essentially technical in nature, and we ignore them here. The generalization to the so-called stabilized bi-conjugate gradient method ("Bi-CGStab") is described, e.g., in Ref. [82].

Given a vector $x^* \in \mathbf{R}^n$ and some basis $\{e_i\}$ for $\mathbf{R}^n$, a basic postulate of linear algebra

guarantees that this vector has a decomposition:[1]

$$x^* = \sum_i \frac{e_i^{\mathrm{T}} x^*}{e_i^{\mathrm{T}} e_i} e_i = \sum_i \frac{\langle e_i, x^* \rangle}{\langle e_i, e_i \rangle} e_i. \tag{B.1}$$

Of course, computing this decomposition requires direct knowledge of the vector. Suppose, however, that we only possess indirect knowledge of the vector through some additional condition. For instance, suppose that the vector x^* solves the linear equation $Ax = b$. In this case, the matrix A (assumed to be symmetric and positive definite) induces an additional product structure on $\mathbf{R}^n$. Suppose that $\{d_i\}$ is an A-orthogonal basis of *conjugate directions* for $\mathbf{R}^n$:

$$\langle d_i, d_j \rangle_A = \langle d_i, Ad_j \rangle = d_i^T A d_j \propto \delta_{ij}, \tag{B.2}$$

which we do not assume satisfies any particular normalization condition. Expanding x^* in terms of this basis yields:

$$x^* = \sum_i \frac{d_i^T A x^*}{d_i^T A d_i} = \sum_i \frac{d_i^T b}{d_i^T A d_i} = \sum_i \frac{\langle d_i, b \rangle}{\langle d_i, d_i \rangle_A}. \tag{B.3}$$

This formula is the foundation for the following theorem, which constructs the unknown vector x^* from the matrix A and vector b, starting from an arbitrary initial guess x_0.

B.2 The Method of Conjugate Directions

Theorem 2 (Method of Conjugate Directions)**.** *Suppose $Ax^* = b$. Let $\{d_0, d_1, \ldots d_{n-1}\}$ be an ordered basis of A-orthogonal conjugate directions in $\mathbf{R}^n$, and take x_0 be an arbitrary point in $\mathbf{R}^n$. Then the sequence $\{x_0, x_1, \ldots x_n\}$ with $x_{k+1} = x_k + \alpha_k d_k$ and*

$$\alpha_k = -\frac{\langle d_k, g_k \rangle}{\langle d_k, d_k \rangle_A} \tag{B.4}$$

converges to $x^* - x_0$ within n steps.

Proof. Begin by expanding $x^* - x_0$ in the basis $\{d_k\}$:

$$x^* - x_0 = \alpha_0 d_0 + \alpha_1 d_1 + \cdots + \alpha_{n-1} d_{n-1}.$$

[1] Throughout this appendix we shall temporarily abandon the summation convention for repeated indices.

A-orthogonality delivers that the coefficients take the form:

$$\alpha_k = \frac{\langle d_k, x^* - x_0 \rangle_A}{\langle d_k, d_k \rangle_A}. \tag{B.5}$$

Next, using the recursive definition of x_k, write

$$x_k - x_0 = \alpha_0 d_0 + \alpha_1 d_1 + \cdots + \alpha_{k-1} d_{k-1}. \tag{B.6}$$

But since the conjugate directions are A-orthogonal, it follows that $\langle d_k, x_k - x_0 \rangle_A = 0$. In other words, $\langle d_k, x_k \rangle_A = \langle d_k, x_0 \rangle$. Substituting this result into the original formula for the expansion coefficients, one discovers that

$$\alpha_k = -\frac{\langle d_k, g_k \rangle}{\langle d_k, d_k \rangle_A}, \tag{B.7}$$

which was to be shown. Because we have explicitly constructed $x^* - x_0$ using a basis expansion in $\mathbf{R}^n$, the convergence is clear. □

As the previous proof demonstrates, the "method of conjugate directions" is nothing more than a convenient basis expansion. The expansion is somewhat unusual because the conjugate directions is not orthogonal with respect the Euclidean structure of $\mathbf{R}^n$. The following theorem and its corollaries reveal the geometric structure of this expansion.

Theorem 3 (Expanding Subspaces)**.** *Let $\{d_0, d_1, \ldots d_{n-1}\}$ an ordered basis of A-orthogonal conjugate directions in $\mathbf{R}^n$, and take x_0 be an arbitrary point in $\mathbf{R}^n$. Let $\{x_0, x_1, \ldots x_{n-1}\}$ and $\{g_0, g_1, \ldots g_{n-1}\}$ be the sequences of points and gradients, respectively, from Theorem 2. Let $\mathcal{B}_k = \text{span}\{d_0, \ldots, d_{k-1}\} \subseteq R^n$ denote the span of the first k conjugate directions. Then each element in the sequence of expanding subspaces $\mathcal{B}_0 \subset \mathcal{B}_1 \subset \ldots \mathcal{B}_{n-1} = \mathbf{R}^n$ is orthogonal to the respective gradient: $g_k \perp \mathcal{B}_k$.*

Proof. The proof is by induction. By definition $\mathcal{B}_0$ is empty, so $g_0 \perp \mathcal{B}_0$. Suppose that $g_k \perp B_k$. By definition of the gradients and the definition of α_k, the following product vanishes identically,

$$\langle d_k, g_{k+1} \rangle = \langle d_k, g_k \rangle + \alpha_k \langle d_k, d_k \rangle_A = 0. \tag{B.8}$$

We must argue that similar results hold for all $i < k$. But

$$\langle d_i, g_{k+1} \rangle = \langle d_i, g_k \rangle + \alpha_k \langle d_i, d_k \rangle_A = 0, \tag{B.9}$$

since the first term vanishes by assumption and the second by A-orthogonality of the conjugate directions. Therefore, g_{k+1} is orthogonal to the span of the first $k+1$ conjugate directions, which was to be shown. □

Corollary 1. *Let $\{d_i\}$ and $\{g_i\}$ be the conjugate directions and gradients of Theorem 2. Then $\langle g_k, d_i \rangle = g_k^T d_i = 0$ for all $i < k$.*

Corollary 2. *Let $\{x_i\}$ be the sequence of points from Theorem 2 with arbitrary point x_0 in $\mathbf{R}^n$. Then each point x_k in this sequence minimizes $f(x) = \frac{1}{2} x^T A x - x^T b$ on the linear variety $x_0 + \mathcal{B}_k$. In particular, the point x_k minimizes $f(x)$ along the line $x_{k-1} + \alpha d_{k-1}$, $\alpha \in \mathbf{R}$.*

B.3 The Method of Conjugate Gradients

From a computational perspective, the main drawback to using the basis expansion in terms of conjugate directions is that they are required to be given in advance. It would be more convenient if the linear system $Ax = b$ also furnished an ordered basis of conjugate directions. In fact, given an arbitrary starting guess x_0, we shall discover that such a basis does exist. The idea is to consider *conjugate gradients*. The conjugate gradients d_{k+1} are each defined recursively as the linear combination of the gradient g_{k+1} and the previous conjugate direction d_k which is A-orthogonal to g_k:

$$d_{k+1} = -g_{k+1} + \beta_k d_k. \tag{B.10}$$

The constant β_k is fixed by imposing A-orthogonality: $\langle d_k, d_{k+1} \rangle_A = 0$. We begin with a lemma, which illustrates that the conjugate gradients are in fact nothing but a convenient basis for the Krylov subspaces generated by g_0 and A.

Lemma 2 (Krylov subspaces)**.** *Let $\mathcal{K}_k(g_0, A) = span\{A^0 g_0, A^1 g_0, \dots A^k g_0\}$ denote the order-k Krylov subspace generated by g_0 and A. Then the spans of the first $k+1$ gradients and conjugate gradients are both equal to the $\mathcal{K}_k$. Moreover, the first k conjugate gradients are A-orthogonal.*

Proof. The lemma amounts to the following three conditions:

$$\text{span}\{g_0, g_1, \dots g_k\} = \mathcal{K}_k(g_0, Q) \tag{B.11}$$

$$\text{span}\{d_0, d_1, \dots d_k\} \equiv \mathcal{B}_{k+1} = \mathcal{K}_k(g_0, Q) \tag{B.12}$$

$$d_k^{\mathrm{T}} A d_i = \langle d_k, d_i \rangle_A = 0 \,\text{for all}\, i < k. \tag{B.13}$$

The proof proceeds by simultaneous induction on all three cases. The base case ($k = 0$) holds by definition. Suppose that the conditions hold for k. We must demonstrate the validity for $k+1$.

First, by definition of the gradient,

$$g_{k+1} = g_k + \alpha_k A d_k. \tag{B.14}$$

For the first term, the inductive hypothesis says that $g_k \in \mathcal{K}_k \subseteq \mathcal{K}_{k+1}$. For the second term, the inductive hypothesis says $d_k \in \mathcal{K}_k$, so $Ad_k \in \mathcal{K}_{k+1}$. Moreover, Theorem 3 says that $g_{k+1} \perp \mathcal{B}_{k+1}$, so (unless $g_{k+1} = 0$, in which case the sequence terminates) $g_{k+1} \notin \mathcal{K}_k$. Thus we have established that $\text{span}\{g_0, g_1, \dots g_{k+1}\} = \mathcal{K}_{k+1}$ for all k. Next consider the definition of the conjugate gradient

$$d_{k+1} = -g_{k+1} + \beta_k d_k. \tag{B.15}$$

The previous argument for the gradients demonstrated that $g_{k+1} \in \mathcal{K}_{k+1}$. By the inductive hypothesis, $d_k \in \mathcal{K}_k$, so $\mathcal{B}_{k+2} = \mathcal{K}_{k+1}$ for all k.

Finally, we must show that the conjugate gradients are all A-orthogonal. Consider therefore the following product

$$\langle d_{k+1}, d_i \rangle_A = -\langle g_{k+1}, d_i \rangle_A + \beta_k \langle d_k, d_i \rangle_A . \tag{B.16}$$

When $i = k$, the definition of β_k guarantees that this expression vanishes. For $i < k$ both terms on the right-hand side vanish. The second term vanishes by the induction hypothesis. To see that first

term vanishes, note that the induction hypothesis—the statement that the conjugate gradients are A-orthogonal through order k—implies $Ad_i \in \mathcal{B}_{i+1}$. Theorem 3 then shows that g_{k+1} is orthogonal to $\mathcal{B}_{i+1}$, so $\langle g_{k+1}, d_i \rangle_A$ vanishes. Thus all the conjugate gradients are, in fact, A-orthogonal. □

The previous lemma makes it easy to extend the method of conjugate direction to a method of conjugate gradients. The beauty of the method of conjugate gradients is that it constructs the necessary A-orthogonal basis of conjugate directions $\{d_k\}$ alongside the sequence of points $\{x_k\}$.

Theorem 4 (Method of Conjugate Gradients)**.** *Suppose $Ax^* = b$. Let x_0 be an arbitrary point in $\mathbf{R}^n$ and $g_k = Ax_k - b$ be the gradient. Then the following sequence $\{x_0, x_1, \ldots x_n\}$ converges to $x^* - x_0$ after n steps:*

$$x_{k+1} = x_k + \alpha_k d_k \tag{B.17}$$

$$\alpha_k = -\frac{\langle g_k, d_k \rangle}{\langle d_k, d_k \rangle_A} \tag{B.18}$$

$$d_{k+1} = -g_{k+1} + \beta_k d_k \tag{B.19}$$

$$\beta_k = \frac{\langle g_{k+1}, d_k \rangle_A}{\langle d_k, d_k \rangle_A} \tag{B.20}$$

Proof. By Lemma 2, the conjugate gradients $\{d_k\}$ form an A-orthogonal basis for $\mathbf{R}^n$. By Theorem 2, the sequence $\{x_k\}$ converges to $x^* - x_0$ after n steps. □

Alternative forms forms for the coefficients α_k and β_k reduce the number of explicit matrix-times-vector operations necessary in the method of conjugate gradients. These "improved" coefficients therefore reduce the computational cost of the method, which might reasonably be called "improved conjugate gradient."

Theorem 5 (Improved Conjugate Gradients)**.** *The following alternative expressions are equivalent to the original definitions for the coefficients α_k and β_k:*

$$\alpha_k = \frac{\langle g_k, g_k \rangle}{\langle d_k, d_k \rangle_A} \tag{B.21}$$

$$\beta_k = \frac{\langle g_{k+1}, g_{k+1} \rangle}{\langle g_k, g_k \rangle} \tag{B.22}$$

Proof. Comparing the new formula for α_k to the definition reveals that we must show $\langle g_k, g_k \rangle = -\langle g_k, d_k \rangle$. But the definition of d_k says that

$$-\langle g_k, d_k \rangle = \langle g_k, g_k \rangle - \beta_{k-1} \langle g_k, d_{k-1} \rangle , \tag{B.23}$$

and the second term vanishes by Theorem 3. To check the proposed formula for β_k, notice that the definitions of the gradients g_k and points x_k imply

$$g_{k+1} - g_k = A(x_{k+1} - x_k) \tag{B.24}$$

$$x_{k+1} - x_k = \alpha_k d_k. \tag{B.25}$$

Solving these equations, we find that $Ad_k = (g_{k+1} - g_k)/\alpha_k$. Taking the product with g_{k+1} reveals

$$\langle g_{k+1}, d_k \rangle_A = \frac{1}{\alpha_k} \langle g_{k+1}, g_{k+1} \rangle \tag{B.26}$$

$$= \frac{\langle d_k, d_k \rangle_A}{\langle g_k, g_k \rangle} \langle g_{k+1}, g_{k+1} \rangle . \tag{B.27}$$

In the first line we have used that $g_k \in \mathcal{B}_k$ and g_{k+1} are perpendicular by Theorem 3. In the second line we have used the expression for α_k. But this quantity is the numerator in the definition for β_k, so the result is now immediate. □

The following algorithm summarizes the results of this appendix.

Algorithm 1: The Method of Conjugate Gradients (Theorems 4 and 5)

Data: Matrix A, vector b, starting vector x_0 and tolerance $\epsilon > 0$.

Result: The vector x^* solving $Ax - b = 0$ within the specified tolerance.

Initialize: Set x_0 arbitrarily or by guessing;

$g_0 \leftarrow Ax_0 - b$;

$d_0 \leftarrow -g_0$;

while $|g_k| > \epsilon$ **do**

$\alpha_k \leftarrow \frac{\langle g_k, g_k \rangle}{\langle d_k, d_k \rangle_A}$;

$x_{k+1} \leftarrow x_k + \alpha_k d_k$;

$g_{k+1} \leftarrow Ax_{k+1} - b$;

$\beta_k \leftarrow \frac{\langle g_{k+1}, g_{k+1} \rangle}{\langle g_k, g_k \rangle}$;

$d_{k+1} \leftarrow -g_{k+1} + \beta k d_k$;

end

return $x_k \approx x^*$

Appendix C

Construction of Lattice Correlation Functions

C.1 Chimera Baryons

Let Q denote a sextet fermion and q a fundamental fermion. The interpolating field for a chimera baryon has the form $\mathcal{O}_B^\epsilon = \epsilon_{abcd} Q_\alpha^{ab} q_\gamma^c q_\delta^d C^{\alpha\gamma\delta\epsilon}$, where Latin indices indicate SU(4) color and Greek indices indicate spin. For brevity we suppress flavor SU(2) indices. The tensor C is some combination of gamma matrices which projects onto the desired spin state. Because these chimera operators are fermionic, they naturally carry a free spinor index. We find it useful to work in a "non-relativistic" formulation, projecting onto eigenstates of $P_\pm = \frac{1}{2}(1 \pm \gamma_4)$. This projection produces two-component spinors, which we identify with the familiar spin-up and spin-down states of a non-relativistic fermion. To extract the ground-state mass from a two-point correlation function, any gauge-invariant operator with the correct spin and internal quantum numbers suffices. Since the mass spectrum is the focus of the present work, we find the non-relativistic formulation easiest to implement. For a discussion of its use in the existing lattice literature, see [113, 109] and references therein.

Propagators form the numerical building blocks of our correlation functions:

$$D_q^{-1}(m|n)_{\alpha,\beta}^{a,b} \equiv \left\langle q(m)_\alpha^a \bar{q}(n)_\beta^b \right\rangle, \tag{C.1}$$

where m, n are points on the lattice; a, b are SU(4)-color indices; and α, β are non-relativistic spin indices. There is an analogous expression for the sextet propagator D_Q^{-1}. A chimera propagator

then takes the form

$$\left\langle \mathcal{O}_B^{\lambda}(m)\overline{\mathcal{O}}_B^{\zeta}(n)\right\rangle = \epsilon_{abcd}\epsilon_{efgh}C^{\alpha\gamma\delta\lambda}C^{\epsilon\phi\eta\zeta}D_Q^{-1}(m|n)_{\alpha,\epsilon}^{ab,ef} \times \left[D_q^{-1}(m|n)_{\gamma,\phi}^{c,g}D_q^{-1}(m|n)_{\delta,h}^{d,h} - D_q^{-1}(m|n)_{\gamma,\eta}^{c,h}D_q^{-1}(m|n)_{\delta,\phi}^{d,g}\right] \tag{C.2}$$

The bracketed expression contains both a direct and an exchange term. Both terms are necessary for states like the charged Σ or Σ^* in QCD which consist of a single light flavor u or d. States like the Λ, Σ_0, or Σ_0^* inherently contain light quarks of two different flavors u and d. Since different valence flavors cannot be contracted, such states possess no exchange term. For the chimera analogues of the Σ and Σ^*, we consider $I_z = 1$ states, which include both the direct and exchange term.

The spin projectors $C^{\alpha\beta\gamma\lambda}$ isolate the correct spin states for the initial and final baryons. For example, the standard decomposition of the spins of the $S = -1$ hyperons is:

$$\begin{aligned}
\Sigma^* &: |J = 3/2, I = 1\rangle = |\uparrow\uparrow\uparrow\rangle \\
\Sigma &: |J = 1/2, I = 1\rangle = \frac{1}{\sqrt{6}}\left[2|\downarrow\uparrow\uparrow\rangle - |\uparrow\uparrow\downarrow\rangle - |\uparrow\downarrow\uparrow\rangle\right] \\
\Lambda &: |J = 1/2, I = 0\rangle = \frac{1}{\sqrt{2}}\left[|\uparrow\uparrow\downarrow\rangle - |\uparrow\downarrow\uparrow\rangle\right].
\end{aligned} \tag{C.3}$$

In each line we have taken the state with largest value of J_z: for example, $|J = 1/2, I = 0\rangle$ is shorthand for the $J_z = +1/2$ state. The states on the right-hand side are $|S_z^Q S_z^q S_z^q\rangle$.

Appendix D

Data Tables

Ensemble	β	κ_4	κ_6	Configurations
1	7.2	0.13173	0.13423	67
2	7.2	0.1318	0.1341	29
3	7.2	0.132	0.134	42
4	7.3	0.1314	0.1333	17
5	7.3	0.1315	0.1333	17
6	7.308	0.1304	0.1339	29
7	7.31	0.1305	0.1339	17
8	7.32	0.13	0.134	17
9	7.33	0.1314	0.1332	17
10	7.33	0.1314	0.1333	17
11	7.33	0.1315	0.1335	17
12	7.4	0.1307	0.133	17
13	7.4	0.131	0.133	29
14	7.5	0.13	0.132	17
15	7.5	0.13	0.1325	29
16	7.5	0.13	0.1327	29
17	7.5	0.13	0.1328	29
18	7.5	0.1305	0.1327	29
19	7.75	0.129	0.131	29
20	7.75	0.129	0.1315	29

Table D.1: List of ensembles with $V = 16^3 \times 18$ generated for this study. Configurations are separated by 4 Monte Carlo trajectories.

Ensemble	β	κ_4	κ_6	Configurations
21	7.25	0.13095	0.13418	61
22	7.25	0.13147	0.13395	71
23	7.276	0.13157	0.13364	96
24	7.3	0.13117	0.13363	61
25	7.3	0.13118	0.13361	96
26	7.3	0.13162	0.1334	71
27	7.308	0.1304	0.13393	96
28	7.33	0.1314	0.1332	96
29	7.4	0.1307	0.133	96
30	7.55	0.129	0.1325	84
31	7.55	0.13	0.1325	84
32	7.65	0.128	0.131	49
33	7.65	0.129	0.1308	49
34	7.65	0.13	0.131	84
35	7.65	0.13	0.132	84
36	7.75	0.128	0.131	84
37	7.75	0.129	0.1308	54
38	7.75	0.1295	0.1315	34
39	7.85	0.129	0.1308	44

Table D.2: List of ensembles with $V = 16^3 \times 32$. Configurations are separated by 10 Monte Carlo trajectories.

Ensemble	β	κ_4	κ_6	Configurations
40	7.51	0.1307	0.1328	133
41	7.55	0.13	0.1327	80
42	7.55	0.1305	0.1325	91
43	7.55	0.1307	0.13234	80

Table D.3: List of ensembles with $V = 24^3 \times 48$. Configurations are separated by 10 Monte Carlo trajectories.

Ensemble	t_0/a^2	$\hat{m}_4$	$\hat{m}_6$
1	1.07(2)	0.024(1)	0.022(1)
2	0.92(3)	0.026(2)	0.030(2)
3	0.89(2)	0.023(1)	0.033(1)
4	0.99(3)	0.034(3)	0.043(4)
5	0.93(2)	0.028(2)	0.043(2)
6	1.07(3)	0.056(2)	0.024(2)
7	1.26(2)	0.054(3)	0.023(3)
8	1.20(3)	0.066(4)	0.018(2)
9	1.15(3)	0.027(3)	0.043(3)
10	1.22(1)	0.026(2)	0.037(1)
11	1.40(2)	0.020(1)	0.029(1)
12	1.26(2)	0.041(2)	0.041(4)
13	1.45(2)	0.030(2)	0.039(2)
14	1.09(3)	0.061(3)	0.067(4)
15	1.33(2)	0.056(2)	0.046(2)
16	1.49(4)	0.055(3)	0.035(3)
17	1.67(2)	0.055(2)	0.031(1)
18	1.89(3)	0.034(3)	0.031(3)
19	1.99(6)	0.075(2)	0.071(2)
20	2.38(6)	0.072(3)	0.043(2)

Table D.4: Measured gradient flow scale t_0 and fermion masses $\hat{m}_r = m_r\sqrt{t_0}$ in the ensembles with volume $V = 16^3 \times 18$.

Ensemble	t_0/a^2	$\hat{m}_4$	$\hat{m}_6$
21	1.093(9)	0.0422(7)	0.0203(10)
22	1.135(9)	0.0279(11)	0.0251(12)
23	1.128(24)	0.0243(7)	0.0326(7)
24	1.132(12)	0.0345(8)	0.0323(14)
25	1.100(10)	0.0331(5)	0.0325(5)
26	1.111(9)	0.0228(6)	0.0381(8)
27	1.174(10)	0.0556(7)	0.0220(9)
28	1.095(12)	0.0282(7)	0.0427(7)
29	1.226(10)	0.0416(8)	0.0403(8)
30	1.418(12)	0.0865(11)	0.0414(15)
31	1.845(18)	0.0495(11)	0.0340(13)
32	0.916(5)	0.1068(8)	0.0858(15)
33	1.067(5)	0.0816(10)	0.0896(8)
34	1.463(15)	0.0459(18)	0.0801(22)
35	2.294(22)	0.0382(13)	0.0357(21)
36	1.556(12)	0.1077(12)	0.0708(10)
37	1.754(15)	0.0730(19)	0.0771(16)
38	2.621(20)	0.0465(13)	0.0402(14)
39	2.670(22)	0.0602(14)	0.0599(12)

Table D.5: Same as Table D.4, but in the ensembles with volume $V = 16^3 \times 32$.

Ensemble	t_0/a^2	$\hat{m}_4$	$\hat{m}_6$
40	2.260(16)	0.0196(4)	0.0194(9)
41	2.166(11)	0.0468(5)	0.0205(4)
42	2.182(12)	0.0264(5)	0.0293(6)
43	2.118(6)	0.0189(5)	0.0360(7)

Table D.6: Same as Table D.4, but in the ensembles with volume $V = 24^3 \times 48$.

Ensemble	$\hat{M}_{P4}$	$\hat{M}_{P6}$	$\hat{F}_{P4}$	$\hat{F}_{P6}$
1	0.28(1)	0.29(1)	0.102(8)	0.143(8)
2	0.28(2)	0.32(2)	0.106(4)	0.155(6)
3	0.26(1)	0.33(1)	0.109(17)	0.149(15)
4	0.34(3)	0.41(2)	0.115(17)	0.178(33)
5	0.29(2)	0.38(2)	0.108(13)	0.170(11)
6	0.42(2)	0.31(2)	0.120(8)	0.141(19)
7	0.43(2)	0.30(2)	0.132(10)	0.163(23)
8	0.47(1)	0.28(3)	0.138(10)	0.148(19)
9	0.28(2)	0.39(2)	0.110(10)	0.169(10)
10	0.29(2)	0.38(2)	0.129(17)	0.166(28)
11	0.32(5)	0.32(2)	0.113(5)	0.170(11)
12	0.38(2)	0.40(2)	0.127(17)	0.177(23)
13	0.33(1)	0.39(1)	0.115(9)	0.176(11)
14	0.46(2)	0.50(2)	0.142(7)	0.199(9)
15	0.45(1)	0.43(1)	0.133(10)	0.183(14)
16	0.45(2)	0.38(2)	0.141(14)	0.184(19)
17	0.46(1)	0.36(1)	0.145(9)	0.179(14)
18	0.35(2)	0.35(2)	0.122(11)	0.185(13)
19	0.53(2)	0.55(2)	0.159(6)	0.223(17)
20	0.53(2)	0.43(3)	0.153(14)	0.190(20)

Table D.7: Measured pseudoscalar masses $\hat{M}_{Pr} = M_{Pr}\sqrt{t_0}$ and decay constants $\hat{F}_{Pr} = F_{Pr}\sqrt{t_0}$ in the ensembles with volume $V = 16^3 \times 18$.

Ensemble	$\hat{M}_{P4}$	$\hat{M}_{P6}$	$\hat{F}_{P4}$	$\hat{F}_{P6}$
21	0.366(9)	0.263(10)	0.119(6)	0.142(9)
22	0.305(9)	0.303(8)	0.105(4)	0.151(5)
23	0.275(6)	0.341(7)	0.108(4)	0.162(5)
24	0.340(5)	0.340(9)	0.119(4)	0.168(9)
25	0.339(3)	0.344(6)	0.107(4)	0.148(13)
26	0.279(7)	0.368(11)	0.103(4)	0.167(13)
27	0.423(4)	0.279(5)	0.127(4)	0.159(7)
28	0.300(8)	0.391(8)	0.115(6)	0.173(6)
29	0.372(6)	0.391(4)	0.126(3)	0.173(8)
30	0.559(8)	0.408(12)	0.156(6)	0.187(7)
31	0.429(10)	0.375(9)	0.140(9)	0.189(10)
32	0.597(8)	0.554(5)	0.159(9)	0.208(13)
33	0.514(8)	0.576(9)	0.154(8)	0.219(11)
34	0.412(9)	0.565(9)	0.141(7)	0.224(8)
35	0.400(9)	0.408(10)	0.132(6)	0.192(17)
36	0.636(7)	0.538(8)	0.166(6)	0.210(8)
37	0.530(5)	0.571(7)	0.154(4)	0.223(12)
38	0.443(14)	0.428(15)	0.135(9)	0.188(13)
39	0.505(13)	0.529(17)	0.148(8)	0.216(8)

Table D.8: Same as Table D.7, but in the ensembles with volume $V = 16^3 \times 32$.

Ensemble	$\hat{M}_{P4}$	$\hat{M}_{P6}$	$\hat{F}_{P4}$	$\hat{F}_{P6}$
40	0.278(4)	0.291(10)	0.114(4)	0.167(7)
41	0.418(5)	0.295(7)	0.139(4)	0.169(4)
42	0.317(6)	0.355(8)	0.125(4)	0.182(8)
43	0.267(9)	0.394(8)	0.114(4)	0.184(5)

Table D.9: Same as Table D.7, but in the ensembles with volume $V = 24^3 \times 48$.

Ensemble	$\hat{M}_{V4}$	$\hat{M}_{V6}$	$\hat{F}_{V4}$	$\hat{F}_{V6}$
1	0.50(3)	0.57(4)	–	–
2	0.51(8)	0.59(6)	0.14(3)	0.27(4)
3	0.48(3)	0.56(9)	0.17(3)	0.23(4)
4	0.56(6)	0.67(5)	–	–
5	0.54(7)	0.61(4)	–	–
6	0.62(2)	0.62(6)	–	–
7	0.61(4)	0.60(8)	–	–
8	0.62(4)	0.61(16)	–	–
9	0.52(7)	0.64(7)	0.17(4)	0.26(4)
10	0.56(8)	0.63(5)	–	–
11	0.56(14)	0.60(5)	0.21(3)	0.30(4)
12	0.60(6)	0.67(14)	0.20(4)	0.29(3)
13	0.60(8)	0.69(4)	–	–
14	0.66(4)	0.73(4)	0.22(2)	0.31(3)
15	0.66(3)	0.72(4)	0.22(2)	0.30(2)
16	0.66(4)	0.68(9)	–	–
17	0.66(3)	0.66(3)	0.21(1)	0.28(1)
18	0.64(8)	0.67(5)	0.22(3)	0.29(7)
19	0.75(4)	0.82(3)	0.23(2)	0.34(4)
20	0.74(4)	0.77(10)	–	–

Table D.10: Measured vector masses $\hat{M}_{Vr} = M_{Vr}\sqrt{t_0}$ and decay constants $\hat{F}_{Vr} = F_{Vr}\sqrt{t_0}$ in the ensembles with volume $V = 16^3 \times 18$. Some ensembles did not yield reliable measurements of F_{Vr} because of insufficient statistics. The figures and tables omit data from such ensembles.

Ensemble	$\hat{M}_{V4}$	$\hat{M}_{V6}$	$\hat{F}_{V4}$	$\hat{F}_{V6}$
21	0.56(2)	0.55(3)	0.19(2)	0.275(1)
22	0.51(2)	0.58(3)	0.17(3)	0.265(1)
23	0.53(3)	0.61(1)	0.18(1)	0.263(1)
24	0.56(2)	0.61(2)	0.19(1)	0.265(2)
25	0.52(3)	0.59(2)	0.19(1)	0.265(1)
26	0.50(3)	0.62(2)	–	–
27	0.59(2)	0.57(3)	0.20(1)	0.250(2)
28	0.55(3)	0.65(2)	0.19(1)	0.290(3)
29	0.59(1)	0.66(2)	0.20(1)	0.287(1)
30	0.73(2)	0.71(2)	0.24(3)	0.308(2)
31	0.65(2)	0.70(5)	0.21(1)	0.291(2)
32	0.74(1)	0.78(1)	0.24(2)	0.316(2)
33	0.70(1)	0.79(1)	0.22(1)	0.319(1)
34	0.66(3)	0.82(3)	0.22(3)	0.339(2)
35	0.68(5)	0.77(5)	0.20(5)	0.310(3)
36	0.81(1)	0.80(3)	0.25(1)	0.326(2)
37	0.74(2)	0.82(2)	0.23(4)	0.322(4)
38	0.69(4)	0.76(5)	0.24(2)	0.334(3)
39	0.75(2)	0.83(2)	0.24(2)	0.350(4)

Table D.11: Same as Table D.10, but in the ensembles with volume $V = 16^3 \times 32$.

Ensemble	$\hat{M}_{V4}$	$\hat{M}_{V6}$	$\hat{F}_{V4}$	$\hat{F}_{V6}$
40	0.57(6)	0.61(2)	–	–
41	0.64(2)	0.60(4)	0.17(1)	0.29(2)
42	0.59(3)	0.66(5)	–	–
43	0.57(3)	0.70(2)	0.20(2)	0.32(1)

Table D.12: Same as Table D.10, but in the ensembles with volume $V = 24^3 \times 48$.

Ensemble	β	κ_4	κ_6	Configurations
1	7.25	0.13095	0.13418	61
2	7.25	0.13147	0.13395	71
3	7.30	0.13117	0.13363	61
4	7.30	0.13162	0.13340	71
5	7.55	0.13000	0.13250	84
6	7.65	0.12900	0.13080	49
7	7.65	0.13000	0.13100	84
8	7.65	0.13000	0.13200	84
9	7.75	0.12800	0.13100	84
10	7.75	0.12900	0.13080	54
11	7.75	0.12950	0.13150	34
12	7.85	0.12900	0.13080	44

Table D.13: The ensembles list used in the baryon analysis. All ensembles have volume $V = N_s^3 \times N_t = 16^3 \times 32$.

Ensemble	t_0/a^2	$\hat{m}_4$	$\hat{m}_6$
1	1.093(9)	0.0422(7)	0.020(1)
2	1.135(9)	0.028(1)	0.025(1)
3	1.13(1)	0.0345(8)	0.032(1)
4	1.111(9)	0.0228(6)	0.0381(8)
5	1.85(2)	0.050(1)	0.034(1)
6	1.068(5)	0.082(1)	0.0896(8)
7	1.46(2)	0.046(2)	0.080(2)
8	2.29(2)	0.038(1)	0.036(2)
9	1.56(1)	0.108(1)	0.071(1)
10	1.75(2)	0.073(2)	0.077(2)
11	2.62(2)	0.047(1)	0.040(1)
12	2.67(2)	0.060(1)	0.060(1)

Table D.14: Fermion masses and flow scales for the ensembles used in the baryon analysis.

Ensemble	Chimera $(J, I) = (1/2, 0)$	$(J, I) = (1/2, 1)$	$(J, I) = (3/2, 1)$
1	0.84(3)	0.80(3)	0.94(6)
2	0.80(3)	0.75(3)	0.91(6)
3	0.84(2)	0.81(2)	0.95(4)
4	0.83(3)	0.80(3)	0.96(6)
5	0.97(3)	0.960(9)	1.13(6)
6	1.11(2)	1.09(1)	1.20(2)
7	1.04(2)	1.02(2)	1.15(3)
8	1.00(4)	0.96(4)	1.15(4)
9	1.24(3)	1.21(2)	1.34(5)
10	1.17(2)	1.14(3)	1.28(3)
11	1.07(4)	1.03(4)	1.19(5)
12	1.17(2)	1.13(3)	1.30(3)

Table D.15: Masses $\hat{M}_{Qqq}$ for the chimera baryons in units of the flow scale t_0/a^2.

Ensemble	Fundamental $(J = 0)$	Fundamental $(J = 1)$	Fundamental $(J = 2)$
1	1.13(7)	1.20(8)	1.30(9)
2	1.07(9)	1.1(1)	1.26(9)
3	1.10(7)	1.13(8)	1.25(8)
4	1.0(1)	1.1(1)	1.3(3)
5	1.33(4)	1.39(4)	1.54(8)
6	1.46(3)	1.50(4)	1.61(5)
7	1.29(8)	1.37(5)	1.5(2)
8	1.36(6)	1.4(1)	1.6(2)
9	1.75(2)	1.79(4)	1.85(7)
10	1.54(5)	1.60(3)	1.72(6)
11	1.5(2)	1.55(9)	1.7(2)
12	1.53(4)	1.61(3)	1.73(6)

Table D.16: Masses $\hat{M}_{q^4}$ for the fundamental baryons in units of the flow scale t_0/a^2.

Ensemble	Sextet ($J = 0$)	Sextet ($J = 1$)	Sextet ($J = 2$)	Sextet ($J = 3$)
1	1.89(7)	1.92(7)	2.00(6)	2.13(6)
2	1.90(6)	1.95(7)	2.1(1)	2.2(1)
3	1.880(3)	1.93(4)	2.05(6)	2.17(5)
4	1.98(5)	2.04(5)	2.11(5)	2.23(6)
5	2.27(2)	2.33(3)	2.46(2)	2.61(2)
6	2.6(2)	2.63(8)	2.7(2)	2.77(7)
7	2.76(4)	2.81(5)	2.90(5)	3.00(4)
8	2.49(4)	2.54(6)	2.67(7)	2.84(4)
9	2.55(8)	2.57(7)	2.66(6)	2.80(4)
10	2.75(6)	2.79(6)	2.9(2)	3.01(5)
11	2.54(4)	2.58(6)	2.68(6)	2.81(7)
12	2.71(5)	2.74(4)	2.89(4)	3.06(5)

Table D.17: Masses $\hat{M}_{Q^6}$ for the sextet baryons in units of the flow scale t_0/a^2.